1-1-2012

Multi-component ab2 metal hydride alloys for nickel metal hydride battery applications

Jean Nei
Wayne State University,

MULTI-COMPONENT AB_2 METAL HYDRIDE ALLOYS FOR NICKEL METAL HYDRIDE BATTERY APPLICATIONS

by

JEAN NEI

DISSERTATION

Submitted to the Graduate School

of Wayne State University,

Detroit, Michigan

in partial fulfillment of the requirements

for the degree of

DOCTOR OF PHILOSOPHY

2012

MAJOR: CHEMICAL ENGINEERING

Approved by:

_____

Advisor Date

_____

Co-Advisor Date

_____

_____

_____

ACKNOWLEDGEMENTS

I would like to express my sincere gratitude to my advisors, Dr. Simon Ng and Dr. Steve Salley, for their invaluable assistance, support, and guidance throughout my graduate career at Wayne State University. Their knowledge and advice were the crucial factors that made this project become reality. The many opportunities given by them during the years of my graduate study are much appreciated for the completion of this Ph.D. dissertation.

I would also like to thank my industry advisor and supervisor, Dr. Kwo Young, at Ovonic Battery Company. He guided me with his creativity and profound knowledge in material science and battery technology throughout this project. I greatly appreciate for all his education and efforts in helping me completing the research for this Ph.D. dissertation. In addition, I would like to thank Mr. Michael Fetcenko, President of Ovonic Battery Company, for kindly providing me access to essentially everything in Ovonic's laboratory and experts in various areas. The completion of this project would not be possible without the support of Ovonic Battery Company.

I would like to acknowledge Dr. Dennis Corrigan and Dr. Mark Cheng for their valuable time serving on my committee and constructive suggestions on improving the contents of the dissertation. I also want to thank the group members, current and previous, at Wayne State University and Ovonic Battery Company, who offered me helpful insights and dear friendships during the years.

I would like to express my deep appreciation to my fiancé, Jeremy Szymecko. His love and encouragement gave me the momentum to cross the finish line. Finally, I would like to thank my parents, Shi-Jen and Tsui Nei for their tremendous support and the many sacrifices

they made in order for me to have better opportunities in life. This dissertation is dedicated to my family and loved ones.

TABLE OF CONTENTS

LIST OF TABLES

LIST OF FIGURES

CHAPTER 1

INTRODUCTION

1.1 Overview

As the earth's natural resources depleting and the environmental problems caused by the use of fossil fuel worsening, alternative energy technology development becomes more urgent every day. Wind, water, and sun are the most common renewable energy sources with claims that when the technology is perfected, they can replace the need for fossil fuels. Once the energy is generated by the renewable sources, the demand for energy storage devices, such as smart grid and battery, grows to be crucial. Besides, battery development is also very crucial for the purpose of reducing the dependency on fossil energy in transportation application. In the case of hybrid electric vehicle (HEV), battery can be used to improve the gas mileage by reclaiming the energy from braking and acts as an assist to the internal combustion engine. Alternatively, electricity can be generated by either alternative renewable sources or fossil fuels in a more controllable environment (i.e. power plant) more efficiently and possibly more environmental friendly and it can then be used to charge the battery in plug-in hybrid electric vehicle (PHEV) or pure electric vehicle (EV).

Nickel metal hydride (Ni/MH) battery is one of the mature battery technologies used in transportation application. More than three million HEVs based on Ni/MH battery have been sold in the last fifteen years. The proven safety, durability, and practical price advantages place Ni/MH battery in a dominating position currently.

Although Ni/MH battery performs well in the areas of cycle life, safety, abuse tolerance, ease of maintenance, and cost, it has a drawback in its specific energy. While majority of recent

research have been devoted to the rival battery technology of lithium-ion battery, there is still room for the continuing improvement in specific energy of Ni/MH battery [1, 2].

The research presented here focuses on the fundamental understandings of the multi-component and transition metal-based AB_2 metal hydride (MH) alloy, which has a higher specific energy than the AB_5 MH alloy commonly used as the negative electrode material in Ni/MH batteries. The knowledge obtained from this research will assist in further improving the overall performance of AB_2 MH alloy and potentially formulating alternative MH alloy compositions suitable for Ni/MH battery application.

1.2 Structure of Ni/MH battery

Ni/MH battery is made of three major components: negative electrode, positive electrode, and electrolyte. The negative electrode is constructed with a hydrogen storage alloy that allows electrochemical storage and release of hydrogen during battery charge and discharge process. The positive electrode is electrochemically reversible between nickel hydroxide $Ni(OH)_2$ and nickel oxyhydroxide NiOOH. Both positive and negative reactions take place in an alkaline medium that is usually prepared with KOH solution. An acid solution can also act as electrolyte in Ni/MH battery, however, the metal in the battery would be etched and therefore noble metal has to be used in such condition. Moreover, $Ni(OH)_2$ is not stable and likely to be dissolved in acid solution. For those reasons, alkaline solutions are more preferable in Ni/MH battery the applications.

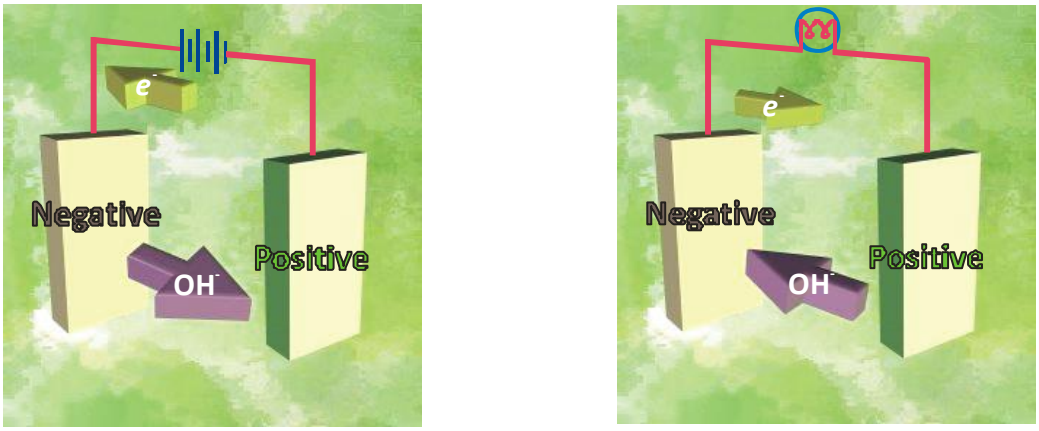

During Charge **During Discharge**

Figure 1.1 Ni/MH battery schematic

Figure 1.1 shows a schematic of Ni/MH battery during charge and discharge. During charge, the water molecule near the surface of the negative electrode is separated into a proton (H^+) and a hydroxyl ion (OH^-) by the applied voltage. H^+ then reacts with the metal in the negative electrode to form MH, and OH^- travels through the electrolyte and reacts with the $Ni(OH)_2$ in the positive electrode to form NiOOH. The positive electrode is oxidized and the negative electrode is reduced during charge. The reactions are reversed during discharge, that is, the positive electrode is reduced and the negative electrode is oxidized. The half-cell and net reactions during charge/discharge can be written as

Negative Electrode $$M + H_2O + e^- \underset{\text{Discharge}}{\overset{\text{Charge}}{\rightleftharpoons}} MH + OH^- \quad (1.1)$$

Positive Electrode $$Ni(OH)_2 + OH^- \underset{\text{Discharge}}{\overset{\text{Charge}}{\rightleftharpoons}} NiOOH + H_2O + e^- \quad (1.2)$$

Net Reaction $$M + Ni(OH)_2 \underset{\text{Discharge}}{\overset{\text{Charge}}{\rightleftharpoons}} MH + NiOOH \quad (1.3)$$

As shown in the net reaction (1.3), there is no consumption or generation of water, therefore the overall electrolyte concentration stays constant during charge/discharge cycle. This result contrasts with other battery systems: in nickel cadmium battery, water is generated during charge and consumed during discharge; in lead-acid battery, water is consumed during charge and generated during discharge. Although transient electrolyte concentration gradients can occur in Ni/MH battery, the constant average concentration of electrolyte provides consistent ionic conductivity and resistance to cycle-life limitations produced by corrosion and swelling [3].

1.3 Hydrogen storage alloy as negative electrode

In order to investigate the chemistry within the hydrogen storage alloy, the hydrogen bonding mechanism needs to be understood. Three types of intramolecular bondings between hydrogen and other elements (different from the intermolecular hydrogen bonding observed in water and DNA) are possible: ionic, covalent, and metallic bondings. Ionic bonding is available when the difference in electronegativities of hydrogen and the host element is large, and atoms of the host element easily give up their valence electrons to the hydrogen atoms. After this process, all the atoms acquire stable or inert gas configurations and additional electric charges, or in other words, they become ions and together from ionic hydrides. Some examples of ionic hydrides include LiH, NaH, and KH. Ionic bonding for NaH is illustrated as an example in Figure 1.2.

Stable electron configurations are assumed in covalent boding model by the sharing of electrons between adjacent atoms that have similar electronegativities. Hydrogen atom and a host atom that are covalently bonded will each contribute at least one electron to the bond, and the shared electrons may be considered to belong to both atoms. This type of bonding is

responsible for forming H_2O, CH_4, etc. Figure 1.3 describes the bonding process of a H_2O molecule.

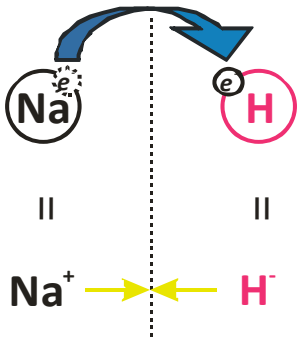

Figure 1.2 Ionic hydride model

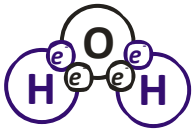

Figure 1.3 Covalent hydride model

Metallic bonding occurs when the difference in electronegativities of hydrogen and the host element is medium. As seen in Figure 1.4, hydrogen atom donates its only electron to the preexisted conduction band of the system and acts as a free proton. The proton then goes into the interstitial site among several host atoms (Figure 1.5). Although the lattice is expanded through this process due to the addition of protons, the crystal structure stays very similar to that of the host system. In general, it's more difficult for a host system to accept the hydrogen atom if it already have too many valence electrons. Therefore, as one moves along the periodic table from left to right in the region where metallic hydride forms, the metal-hydrogen bond becomes weaker (Figure 1.6).

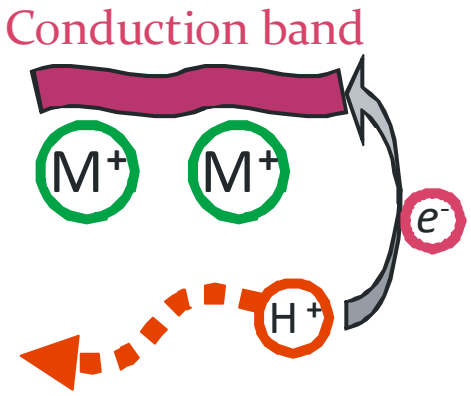

Figure 1.4 Metallic hydride model

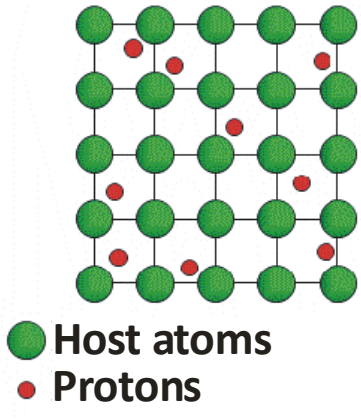

Figure 1.5 Schematic of intrusive hydride

When selecting a hydrogen storage material for Ni/MH battery applications, it is important to evaluate the heat of hydride formation (ΔH), which is a measure of the strength of the metal-hydrogen bond. Among the three different types of hydrogen bonding mechanisms, only the strength of metallic bonding is suitable for gaseous phase hydrogen storage while ionic and covalent bondings are too strong for the purpose of reversible gaseous phase hydrogen storage. Moreover, according to the range of ΔH desirable for room temperature Ni/MH operation (–40 to –30 kJ mol^{-1} H_2 [3-5]), only expensive metals, such as Pd and V, have the appropriate ΔH among all pure systems of metallic bondings as seen in Figure 1.7. Therefore,

the development of hydrogen storage materials is based on multi-element inter-metallic compounds, and their compositions are formulated by balancing the amounts of hydride formers ($\Delta H < 0$) and modifiers ($\Delta H > 0$) to fulfill the performance requirements.

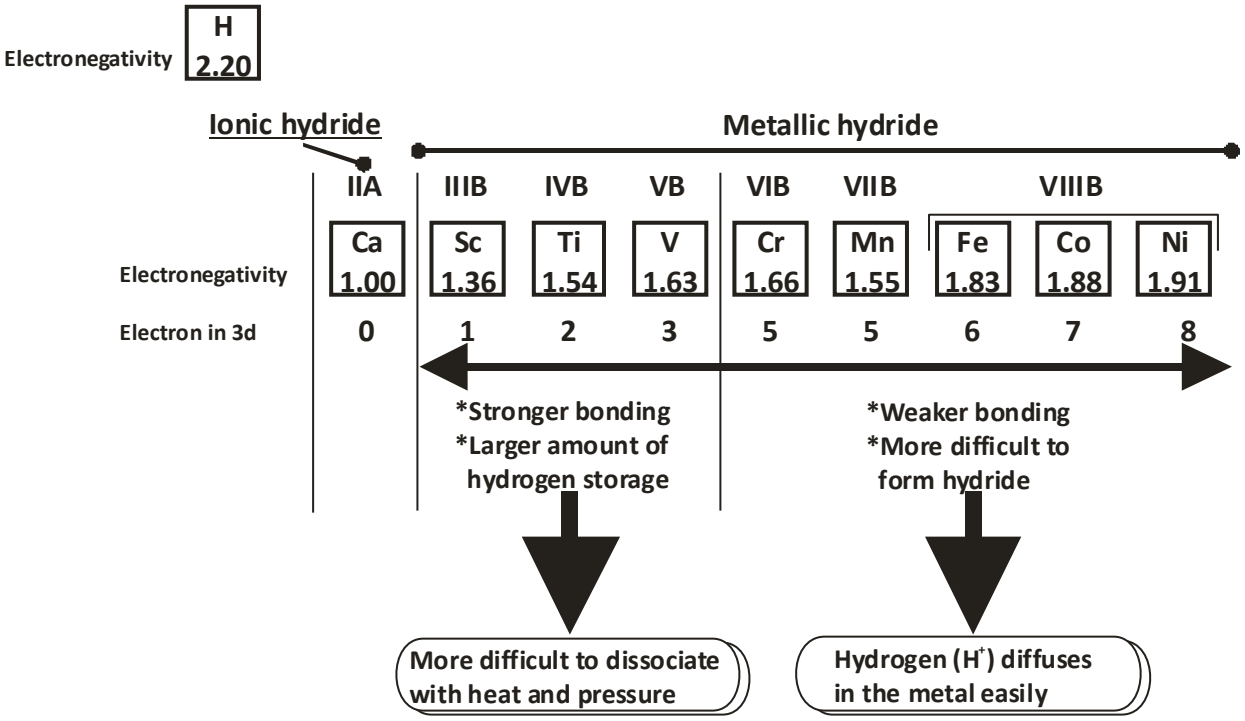

Figure 1.6 Trends of strength of metal-hydrogen bond and ease of forming hydride

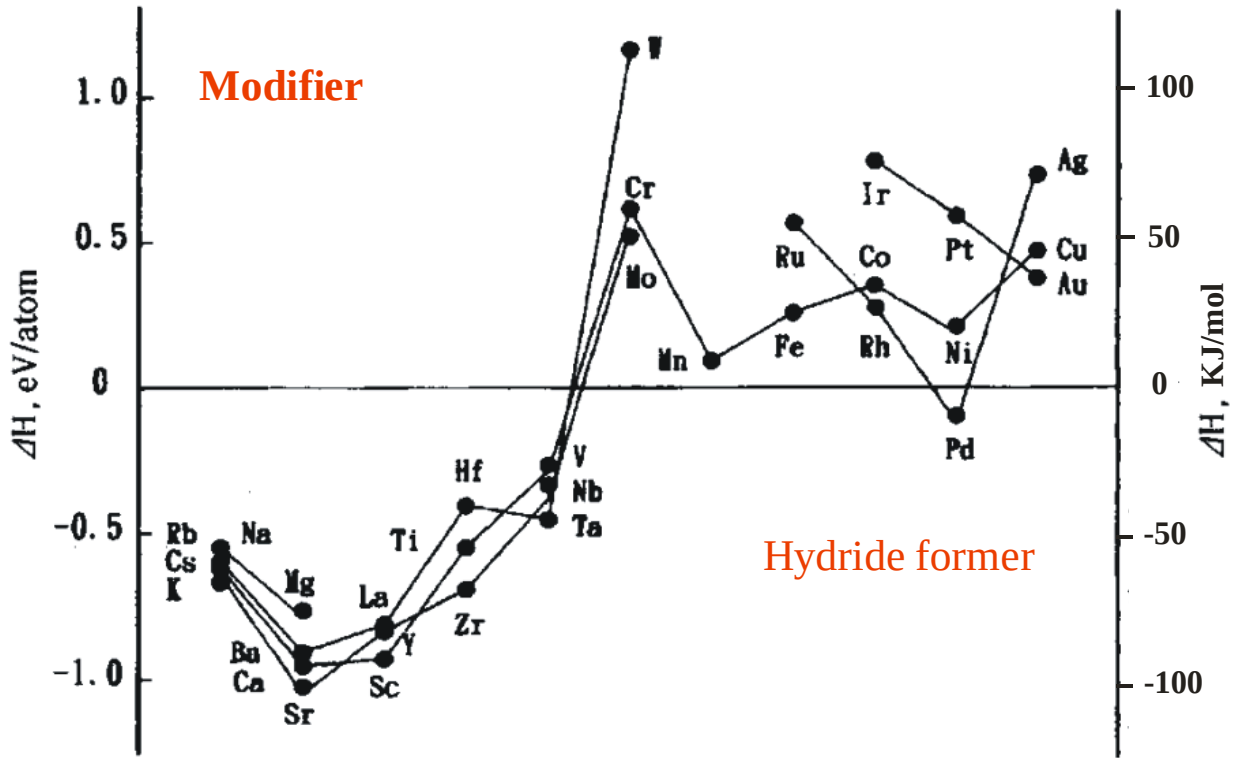

Figure 1.7 Heats of hydride formation for various metals [6]

Two main MH families, AB_5 and AB_2, are currently used as the hydrogen storage negative electrode for Ni/MH batteries. The misch metal-based AB_5 MH alloy is the most commonly used, with misch metals (mixture of light rare earth elements include La, Ce, Pr, and Nd) as the A-site elements and Ni, Mn, Al, Co, etc. as the B-site elements. The main advantages of AB_5 MH alloy are its high power capability as a result of the high B-content and superior cycle life. AB_2 MH alloy is another frequently used alloy system in Ni/MH batteries, with Zr and Ti as the A-site elements and similar B-site elements to those of AB_5 alloy.

While most of the commercial Ni/MH batteries use the mish metal-based AB_5 MH alloy as the negative metal electrode, the transition metal-based AB_2 MH alloy has become one of the most promising candidates to replace AB_5 MH alloy for the purpose of reducing the industry's

dependency on the rare earth imports [2, 7-9]. Furthermore, AB_2 MH alloy demonstrates improvement in specific energy (310 to 340 mAh g^{-1} in AB_5 vs. 384 to 450 mAh g^{-1} in AB_2) [1, 2, 10], which extends the driving range in HEV and PHEV and enables Ni/MH batteries to close up the gap in the competition with lithium-ion batteries.

1.4 AB_2 metal hydride alloy

AB_2 MH alloys used as the negative electrode in Ni/MH batteries are multi-element and multi-phase materials [3]. These alloys are composed of main phases belonging to a family of materials known as Laves phases named after Fritz Laves and secondary non-Laves phases, such as Zr_8Ni_{21}, Zr_7Ni_{10}, Zr_9Ni_{11}, ZrNi, and TiNi [10-29]. The main Laves and secondary non-Laves phases are discussed in detail in the following sections.

1.4.1 Laves phase

Laves phases are a group of three topologically highly closed-packed inter-metallic compounds with the stoichiometry of AB_2: C15 with a face-center-cubic $MgCu_2$ structure, C14 with a hexagonal $MgZn_2$ structure, and C36 with a dihexagonal $MgNi_2$ structure [30, 31]. Most of the research focus on the C14 and C15 phases because the C36 phase is less frequently seen, and previous x-ray diffraction (XRD) analysis and heat of formation calculation indicated that C36 may be an intermediate phase between C14 and C15 [32, 33]. The C14 and C15 phases have different contributions to the gaseous phase hydrogen storage and electrochemical properties of the AB_2 MH alloys. Earlier comparison between the C14 and C15 phases was performed with the modification in chemical composition, and the results favored the C15 phase due to its higher stacking fault density contributing to improvements in both activation and high-

rate dischargeability (HRD) of the electrode [34, 35]. A more recent study conducted by Young et al. [23] separated the contributions from composition and phase abundance and concluded that the C15 phase has both superior gaseous phase hydrogen storage capacity and reversibility, a better HRD due to better reaction in the bulk, a greater specific power, and an improved low-temperature performance with a shortcoming of an inferior cycle life when compared to the C14 phase. Since the gaseous phase hydrogen storage and electrochemical properties of the C14 and C15 phases are different, it is important to be able to predict the C14/C15 phase abundance from the chemical composition during the design stage.

A few parameters were correlated to the C14/C15 phase abundance previously, which include the average electron density (*e*/*a*), geometric atomic size ratio, and difference in electronegativity [36]. The *e*/*a* value is calculated by averaging the numbers of outer-shell electrons of all constituent elements in the formulation. The early works done by Laves and Witte have shown that as *e*/*a* increases, the structure changes from C15, to C36, and finally C14 in several quasi-binary alloy systems involving $MgCu_2$ and $MgZn_2$ [37, 38]. Johnston and Hoffmann summarized the Laves phase transition as a function of the number of the valence electrons per AB_2 unit and successfully correlated it to the energy difference between cubic- and hexagonal-structures calculated by a tight-binding calculation [39]. Zhu et al. reported that based on the Laves phase structures of several binary and ternary AB_2 alloys from the phase diagrams, with $e/a > 5.76$, the C15 structure is stabilized; at an *e*/*a* range of 5.88 to 7.53, the C14 structure is stabilized; with $e/a > 7.65$, the C15 structure is stabilized again; and any further increase in *e*/*a* (> 8) leads to the disordering of the alloy [40]. Similar results were demonstrated with experimental data by the same group [41].

Geometric atomic size ratio is another popular theory in controlling the preference of C14/C15. Assume the AB_2 Laves phases contain spherical atoms in a perfect crystal, the closest packing is obtained at the ideal atomic size ratio of $r_A/r_B = \sqrt{1.5} \approx 1.225$, where r_A and r_B are the average atomic radii of A atoms and B atoms in the AB_2 inter-metallic compounds, respectively [30, 37]. The Laves phases occur between R_A/R_B ratio range of ~ 1.05 to 1.68, where R_A and R_B are the average metallic radii of A atoms and B atoms, respectively [42-44]. Within a reasonable R_A/R_B ratio range, the atoms are able to adjust themselves by expanding or contracting to accommodate the ideal r_A/r_B ratio during the Laves phase formation [43]. As a confirmation of the ideal atomic size ratio and R_A/R_B ratio range for the Laves phases, a study where the enthalpies of formation (ΔH_f) of many Laves phases were plotted as a function of the R_A/R_B ratio has shown that the lowest ΔH_f (most stable) is at an R_A/R_B ratio around 1.225 and lower and higher bounds intersected with $\Delta H_f = 0$ (the compound is thermodynamically unstable beyond this point) are at R_A/R_B ratios of 1.03 and 1.65, respectively [45, 46]. By organizing the details of the existing binary and ternary Laves phases, it was shown that the higher solubility ranges of C14 and C36 phases are observed most frequently within the R_A/R_B ratio range of 1.12 to 1.26, and the higher solubility range of C15 phase is typically seen within the R_A/R_B ratio range of 1.1 to 1.35 [47].

Edwards correlated the size adjustment from *R* to *r* to the difference in electronegativities of the A and B atoms [48]. It was concluded that the size contraction is caused by the attractive interaction between the A and B atoms and can be linked to the square of the difference in A's and B's electronegativities. In other words, the difference in electronegativities of the constituent elements plays an important role in adjusting the r_A/r_B ratio and therefore influences the possibility of forming the Laves phases.

Neither *e*/*a* nor the geometric factor alone can be used to predict the formation of C14/C15 [36]. For example, Ti and Zr have the same number of outer-shell electrons, so if assuming *e*/*a* is the only determining factor in the preference of C14/C15, any composition of $(Ti_xZr_{1-x})B_2$ would have the same Laves phase structure. However, as the Ti-content increases, the main phase shifts from C15 to C14 [49-52].

Most of the previous studies on the effects on the C14/C15 phase abundance were performed on a statistical basis. Therefore, a more systematic investigation that incorporates multiple parameters is needed in order to provide a precise C14/C15 phase abundance database, which will assist the future AB_2 MH alloy design process.

1.4.2 Non-Laves phase

For the best balance between a large storage capacity (lower ΔH) and a high rate discharge capability (higher ΔH) in transition metal-based alloys, a stoichiometry of A : B close to 1 : 2, which has the appropriate ΔH of –40 to –30 kJ mol^{-1} H_2, is desirable for room temperature Ni/MH operation. However, AB_2 inter-metallic compound is not available in either Zr-Ni or Ti-Ni binary system. In the case of multi-phase AB_2 MH system that involves Zr-Ni system (Figure 1.8), after solidification of an alloy with an AB_2 composition, other than the main Laves phase(s), C14 and/or C15, one or more secondary non-Laves phases composed of the neighboring phases of AB_2 can be observed. More specifically, Zr_8Ni_{21}, Zr_7Ni_{10}, Zr_9Ni_{11}, and ZrNi are the most commonly seen secondary phases in AB_2 alloys [10-23, 26-29]. Previous studies have shown that by eliminating the secondary phases with an annealing process, the electrochemical properties deteriorate due to the removal of the synergetic effect between the main storage and secondary catalytic phases [15, 20, 23, 26, 53-56]. The synergetic effect arises

as a result of the multi-phase nature, which provides various properties that together contribute positively to the overall performance. Moreover, the presence of secondary phases offers more catalytic sites in the microstructure for the gaseous phase hydrogen storage and electrochemical reactions. Therefore, the fundamental understandings of these basic non-Laves Zr_xNi_y phases are essential for further performance improvement of AB_2 MH alloys.

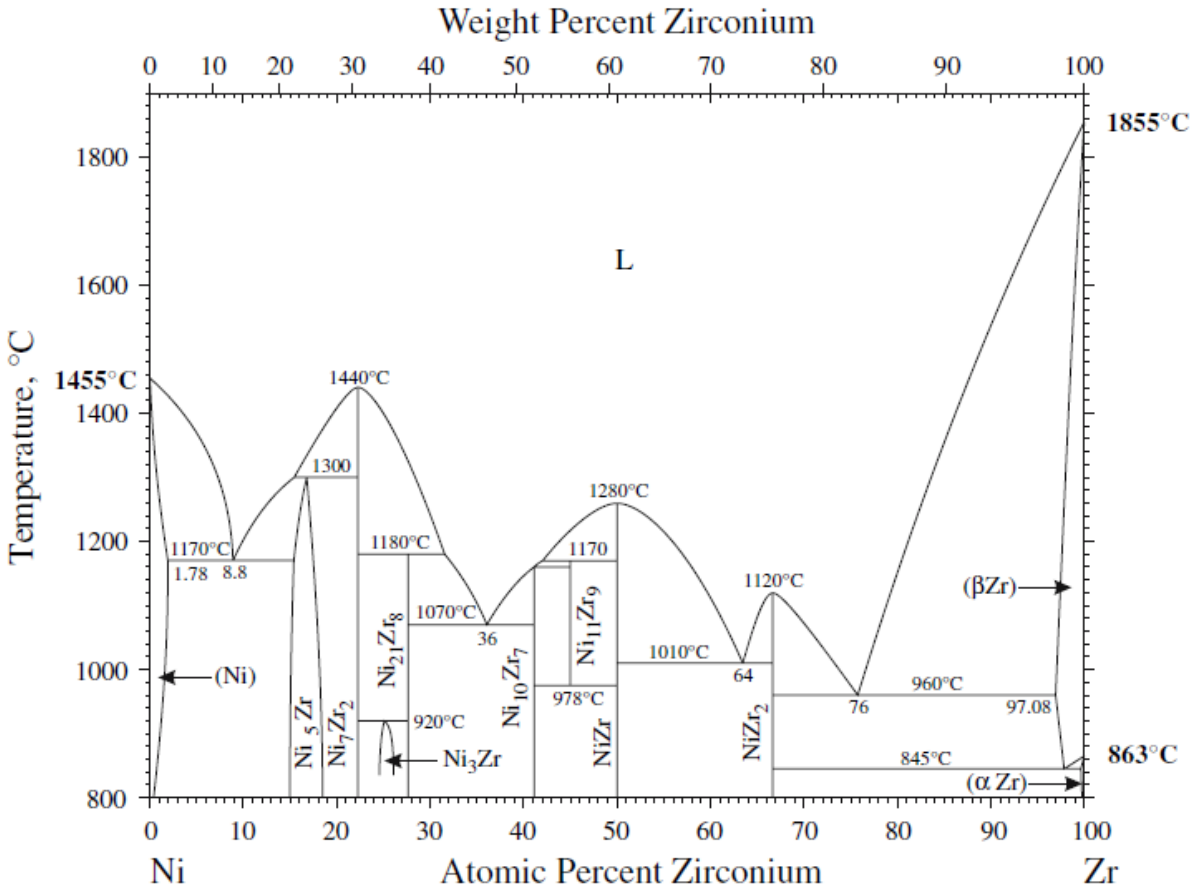

Figure 1.8 Zr-Ni binary phase diagram [57]

Gaseous phase hydrogen storage and electrochemical properties of Zr_8Ni_{21} [56, 58, 59], Zr_7Ni_{10} [12, 13, 56, 58-69], Zr_9Ni_{11} [12, 56, 58, 59, 64, 70, 71], and ZrNi [12, 60, 62, 70, 72-75] have been studied previously. Among these research efforts, Ruiz et al. [56, 59] and Joubert et al.

[12, 58] provided side-by-side comparisons among several of the four non-Laves phase alloys. However, a thorough and systematic examination of all four non-Laves phase alloys that correlates composition, structure, gaseous phase hydrogen storage, and electrochemical properties has not been established in the past. Furthermore, the majority of previous studies were based on the annealed alloys for the purpose of phase purification. Due to the importance of the synergetic effect observed in AB_2 alloys, the effect of secondary phases in the close-related non-Laves phase alloys merits an investigation of the influence of annealing treatment.

1.5 Significance of research

The transition metal-based AB_2 MH alloy has advantages in raw material independency and specific energy over the mish metal-based AB_5 MH alloy commonly used in Ni/MH batteries. However, the multi-phase nature of AB_2 MH alloy is not fully understood, therefore optimization of alloy formulation based on desired performance requirement cannot be achieved. In order to obtain detailed knowledge regarding the formation of the main C14/C15 Laves phases, a systematic investigation that incorporates multiple parameters is presented in the first part of the current research in order to provide a precise C14/C15 phase abundance database, which will assist the future AB_2 MH alloy design process. Moreover, further examination on the determining factors of the C14/C15 threshold is also discussed. In the second part of the current research, several non-Laves secondary phases commonly observed in AB_2 MH alloys including Zr_8Ni_{21}, Zr_7Ni_{10}, Zr_9Ni_{11}, and ZrNi are examined individually, and correlations among composition, structure, gaseous phase hydrogen storage, and electrochemical properties are established. Since the synergetic effect observed in AB_2 MH alloys is crucial to the overall performance, the effect of secondary phases in each of these non-Laves phase alloys is also

investigated by applying annealing treatment. Finally, based on the results obtained, one of the four non-Laves phase alloys, Zr_8Ni_{21}, is chosen for further compositional modification (10 $Zr_8Ni_{19}X_2$ are prepared, where X is the modifying/substituting element in Zr_8Ni_{21}) in hopes of gaining better understanding of Zr_8Ni_{21} MH alloy family and developing alternative MH alloys suitable for Ni/MH battery applications. The modification is done in a way similar to the modifications on AB_5 and AB_2 MH alloys. The effect of annealing on the structure, gaseous phase hydrogen storage, and electrochemical properties of the $Zr_8Ni_{19}X_2$ alloys and the correlations among these characteristics are studied.

With the information obtained from the current research, the overall performance of AB_2 MH alloy can be improved and better controlled in two ways: by recognizing the determining factors of the main C14/C15 Laves phase abundances and known properties of C14 and C15, performance improvement of AB_2 MH alloy through alloy composition adjustment can be accomplished; the fundamental understandings of the non-Laves phase alloys can be related to their contributions in AB_2 MH alloy.

CHAPTER 2

DETERMINATION OF C14/C15 PHASE ABUNDANCE IN LAVES PHASE ALLOYS

A systematic investigation that incorporates multiple parameters was designed for the purpose of examining the determining factors of the C14/C15 phase abundance and the C14 : C15 = 1 : 1 threshold. 23 alloys with the overall AB_2 stoichiometry (the design compositions are shown in Table 2.1) were prepared with raw materials (99.999% purity metals). The six series of alloys, TZ11, TZ73, TZ37, T10, Z10, and H10, were designed in a way that within each series, the A-site composition is the same, the r_A/r_B ratio stays relatively the same, and e/a varies by varying the B-site chemical composition. Although there are several phase changes as e/a increases [40, 41], since most of the Ni-based AB_2 MH alloys have e/a between 6.2 and 7.2 [76], the C14/C15 transition within such e/a range is especially important for the development of the AB_2 MH electrode in Ni/MH battery. Consequently, the e/a values in this study were designed to be in the range of this particular C14/C15 transition. The composition in B-site is identical at the same e/a value from series to series due to the same number of outer-shell electrons among Ti, Zr, and Hf; however, the r_A/r_B ratio varies.

Table 2.1 Design compositions in at.% and corresponding average electron densities

	Alloy name	Ti	Zr	Hf	Cr	Co	Cu	B/A	*e/a*
Ti : Zr = 1 : 1	TZ11-1	16.7	16.7	-	17.8	48.9	-	2.0	6.8
in A-site	TZ11-2	16.7	16.7	-	11.1	55.6	-	2.0	7.0
	TZ11-3	16.7	16.7	-	4.5	62.2	-	2.0	7.2
Ti : Zr = 7 : 3	TZ73-1	23.3	10.0	-	17.8	48.9	-	2.0	6.8
in A-site	TZ73-2	23.3	10.0	-	11.1	55.6	-	2.0	7.0
	TZ73-3	23.3	10.0	-	7.8	58.9	-	2.0	7.1
	TZ73-4	23.3	10.0	-	4.5	62.2	-	2.0	7.2
Ti : Zr = 3 : 7	TZ37-1	10.0	23.3	-	17.8	48.9	-	2.0	6.8
in A-site	TZ37-2	10.0	23.3	-	14.5	52.2	-	2.0	6.9
	TZ37-3	10.0	23.3	-	11.1	55.6	-	2.0	7.0
	TZ37-4	10.0	23.3	-	4.5	62.2	-	2.0	7.2
100% Ti	T10-1	33.3	-	-	11.1	55.6	-	2.0	7.0
in A-site	T10-2	33.3	-	-	4.5	62.2	-	2.0	7.2
	T10-3	33.3	-	-	-	63.4	3.3	2.0	7.4
	T10-4	33.3	-	-	-	53.4	13.3	2.0	7.6
100% Zr	Z10-1	-	33.3	-	31.1	35.6	-	2.0	6.4
in A-site	Z10-2	-	33.3	-	24.5	42.2	-	2.0	6.6
	Z10-3	-	33.3	-	17.8	48.9	-	2.0	6.8
	Z10-4	-	33.3	-	11.1	55.6	-	2.0	7.0
100% Hf	H10-1	-	-	33.3	24.5	42.2	-	2.0	6.6
in A-site	H10-2	-	-	33.3	17.8	48.9	-	2.0	6.8
	H10-3	-	-	33.3	11.1	55.6	-	2.0	7.0
	H10-4	-	-	33.3	4.5	62.2	-	2.0	7.2

2.1 Experimental setup

Samples were prepared by arc melting under a continuous argon flow with a non-consumable tungsten electrode and a water-cooled copper tray. Before each arc melt, a piece of sacrificial titanium underwent a few melting-cooling cycles to reduce the residual oxygen concentration in the system. Each 10-g sample ingot was re-melted and flipped over a few times to ensure uniformity in chemical composition. A Rigaku *Miniflex* XRD was used to study each alloy's microstructure. A JEOL *JSM6320F* scanning electron microscope (SEM) with x-ray energy dispersive spectroscopy (EDS) capability was used to study the phase distribution and composition. Sample alloys for SEM/EDS analysis were mounted and polished on epoxy blocks, rinsed and dried before entering the SEM chamber.

2.2 Results and discussion

A few important properties of the constituent elements, such as atomic number, electronegativity (χ), atomic radius in Laves phase (r), number of outer-shell electrons, and chemical potential for electronic charge (ϕ^*) are listed in Table 2.2.

Table 2.2 Properties of elements used in this study, where χ, r, and ϕ^* are electronegativity, atomic radius in Laves phase, and chemical potential for electronic charge, respectively.

	Ti	**Zr**	**Hf**	**Cr**	**Co**	**Cu**
Atomic number	22	40	72	24	27	29
χ [77]	1.54	1.33	1.30	1.66	1.88	1.90
***r* (Å)** [78]	1.614	1.771	1.743	1.423	1.385	1.413
Number of outer-shell electrons	4	4	4	6	9	11
ϕ^* [79]	3.80	3.45	3.60	4.65	5.10	-

2.2.1 XRD structure analysis

XRD analysis was performed on all 23 alloys. XRD patterns from series TZ73, T10, Z10, and H10 were chosen to show the trend of phase abundance transition (Figure 2.1a-d). Due to the complete overlap of C15 with C14 seen in the selected area diffraction patterns [80], Figure 2.1a-d evidently demonstrates that the major XRD peaks of C15 overlap with several XRD peaks of C14. The lattice constants of the main C14 and C15 phases and the abundances of the identified phases are listed in Table 2.3. The C14 and C15 phase abundances were calculated from the integration of diffraction peaks using a calibration with previous samples done by Rietveld method. The main Laves phase changes from C14 to C15 as *e*/*a* increases in each series, however, at different rates. In TZ73-series, the design Co-content increases to accommodate the increase in *e*/*a*, and the secondary TiCo phase is observed at the highest Co-content (Figure 2.1a). In T10-series, with 100% Ti in the A-site, the existence of the secondary TiCo phase is observed in each alloy (Figure 2.1b). Similarly, the secondary ZrCo and HfCo phases present in Z10-series (Figure 2.1c) and H10-series (Figure 2.1d), respectively. Since the amount of the secondary phase in each alloy of T10-, Z10-, and Hf10-series is significant, as shown in Table 2.3, SEM/EDS analysis was performed in order to determine the composition of the secondary phase. Combining the composition of the secondary phase and the phase abundance calculated by XRD analysis, the actual composition and *e*/*a* of the AB_2 phase can be obtained.

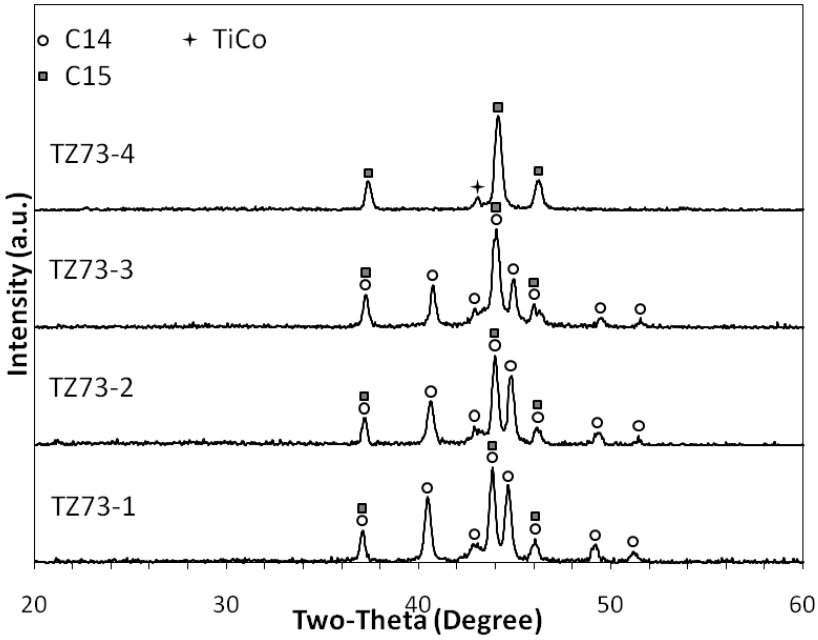

Figure 2.1a XRD patterns using Cu-K_{α} as the radiation source for TZ73-series (Ti : Zr = 7 : 3 in A-site)

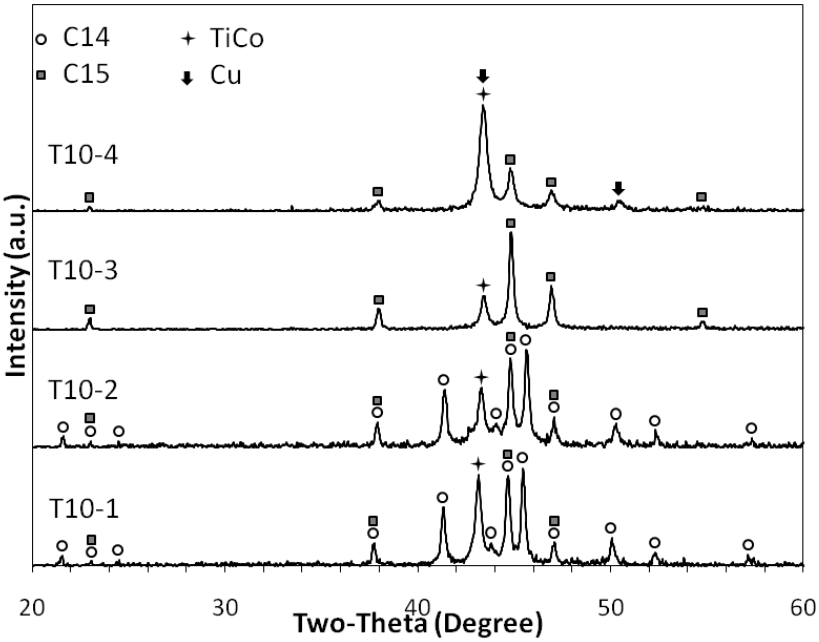

Figure 2.1b XRD patterns using Cu-Kα as the radiation source for T10-series (100% Ti in A-site)

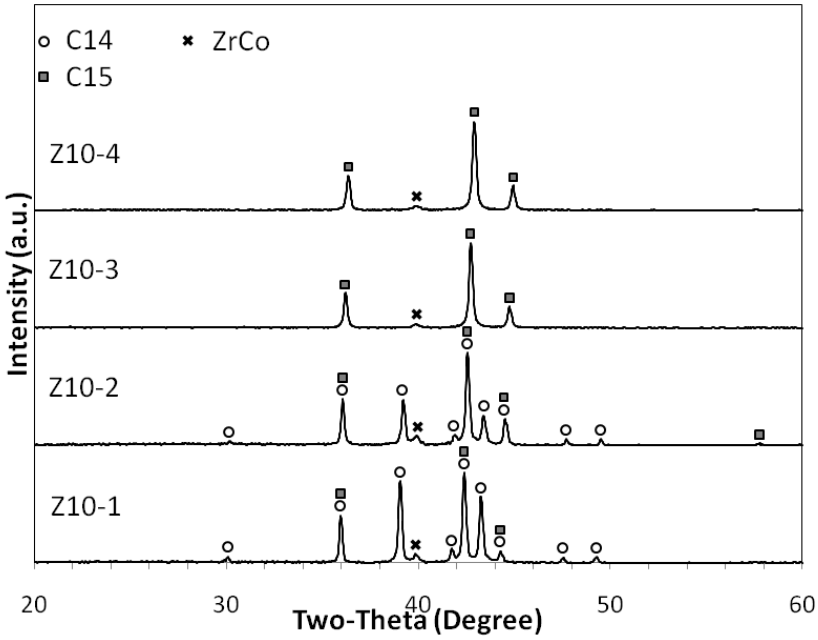

Figure 2.1c XRD patterns using Cu-K_α as the radiation source for Z10-series (100% Zr in A-site)

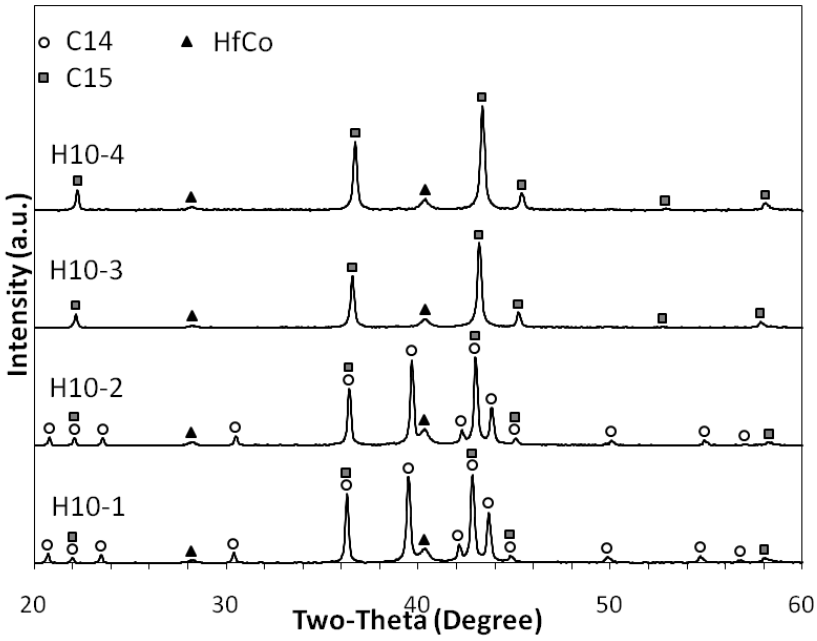

Figure 2.1d XRD patterns using Cu-K_α as the radiation source for H10-series (100% Hf in A-site)

Table 2.3 Summary of XRD results

Alloy name	**C14 lattice constant *a* (Å)**	**C14 lattice constant *c* (Å)**	**C14 unit cell volume ($Å^3$)**	**C15 lattice constant *a* (Å)**	**C15 unit cell volume ($Å^3$)**	**C14 phase abundance (%)**	**C15 phase abundance (%)**	**TiCo phase abundance (%)**	**ZrCo phase abundance (%)**	**HfCo phase abundance (%)**	**Cu phase abundance (%)**
TZ11-1	4.888	7.957	164.64	6.905	329.22	96	4	ND	ND	-	-
TZ11-2	4.865	7.922	162.38	6.887	326.66	49	51	ND	ND	-	-
TZ11-3	-	-	-	6.855	322.12	ND	100	ND	ND	-	-
TZ73-1	4.849	7.877	160.40	6.844	320.58	99	1	ND	ND	-	-
TZ73-2	4.838	7.849	159.10	6.826	318.05	93	7	ND	ND	-	-
TZ73-3	4.829	7.843	158.39	6.821	317.35	66	34	ND	ND	-	-
TZ73-4	-	-	-	6.800	314.43	ND	97	3	ND	-	-
TZ37-1	4.918	8.015	167.88	-	-	100	ND	ND	ND	-	-
TZ37-2	4.906	7.996	166.67	6.944	334.83	31	69	ND	ND	-	-
TZ37-3	4.898	7.982	165.84	6.926	332.24	3	97	ND	ND	-	-
TZ37-4	-	-	-	6.901	328.65	ND	100	ND	ND	-	-
T10-1	4.766	7.719	151.84	-	-	80	ND	20	-	-	-
T10-2	4.746	7.716	150.51	6.704	301.30	80	7	13	-	-	-
T10-3	-	-	-	6.701	300.90	ND	82	18	-	-	ND

T10-4	-	-	-	6.704	301.30	ND	30	62	-	-	8
Z10-1	4.992	8.176	176.45	7.066	352.79	97	1	-	2	-	-
Z10-2	4.977	8.136	174.53	7.040	348.91	65	32	-	3	-	-
Z10-3	-	-	-	7.011	344.62	ND	98	-	2	-	-
Z10-4	-	-	-	6.983	340.51	ND	96	-	4	-	-
H10-1	4.949	8.081	171.41	6.998	342.71	94	3	-	-	3	-
H10-2	4.933	8.041	169.46	6.972	338.90	86	7	-	-	7	-
H10-3	-	-	-	6.942	334.54	ND	92	-	-	8	-
H10-4	-	-	-	6.918	331.09	ND	92	-	-	8	-

It should be noted although some of the as-cast alloys contain secondary non-Laves phase, no annealing treatment is adopted in this study because the practical AB_2 MH alloys in Ni/MH batteries are not annealed in order to retain the synergetic effects between the main storage and secondary catalytic phases [15, 20, 23, 26, 53-56]. Moreover, annealing shrinks the *e*/*a* range corresponding to the C14-C15 transition [23]. The wider transition *e*/*a* window of the unannealed samples increases the precision in identifying the C14 : C15 = 1 : 1 threshold.

When comparing among all series containing Ti and/or Zr, the overall lattice constants of C14 and C15 increase in the order of 100% Ti, to Ti + Zr mixture, and finally 100% Zr in the A-site. Moreover, the alloys with 100% Hf in the A-site have the overall lattice constants between 100% Ti and 100% Zr in the A-site. The variation in lattice constants from series to series is due to the change in size of the A-site elements (Table 2.2). The lattice constants of C14 and C15 in each series decrease as *e*/*a* increases except for the Cu-addition in T10-series. This observation follows the design trend where the composition in B-site changes to vary *e*/*a*. More specifically, *e*/*a* is increased by increasing the content of the smaller-sized Co (larger number of outer-shell electrons compared to the larger-sized Cr). In the case of Cu-addition (chosen to further increase *e*/*a*), its larger size compared to Co increases the lattice constants.

2.2.2 SEM/EDS phase analysis

The microstructures of all the alloys in T10-, Z10-, and H10-series were studied by SEM, and the back-scattering electron images (BEI) with the same magnification are presented in Figure 2.2a-l. The compositions in several areas identified numerically in the micrographs were studied by EDS and the results are listed in Table 2.4. In T10-series of alloys, TiCo is the most prominent of all secondary phases (Figure 2.2a-d); as *e*/*a* increase, the amount of TiCo increases,

which is consistent with the results from XRD analysis. Similar results were obtained from Z10-series (secondary ZrCo phase, Figure 2.2e-h) and H10 (secondary HfCo phase, Figure 2i-l).

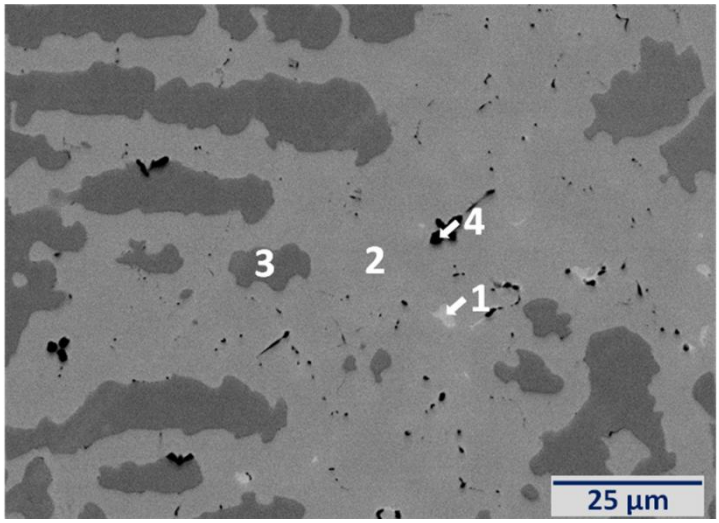

Figure 2.2a SEM BEI images for T10-1, and the chemical compositions of the indexed areas measured by EDS are summarized in Table 2.4.

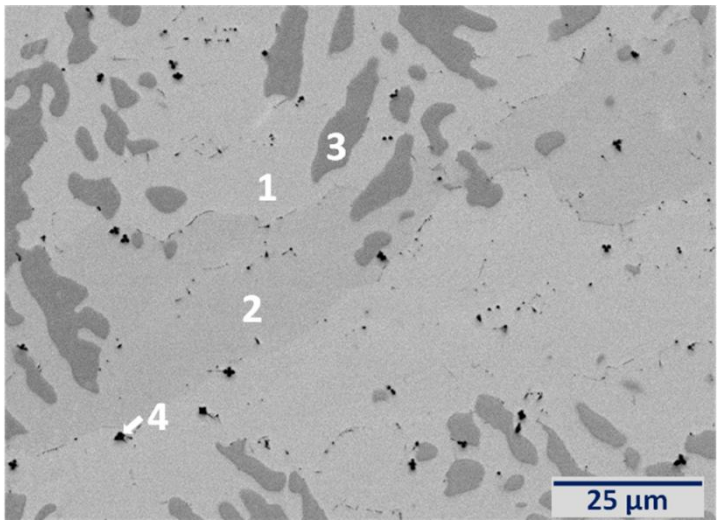

Figure 2.2b SEM BEI images for T10-2, and the chemical compositions of the indexed areas measured by EDS are summarized in Table 2.4.

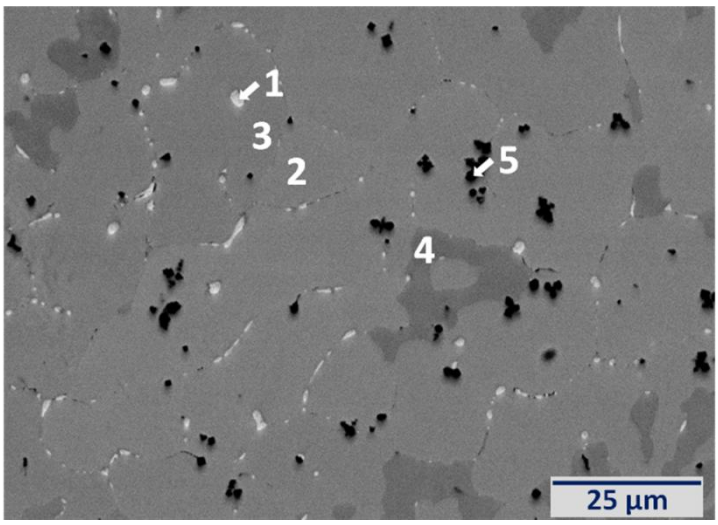

Figure 2.2c SEM BEI images for T10-3, and the chemical compositions of the indexed areas measured by EDS are summarized in Table 2.4.

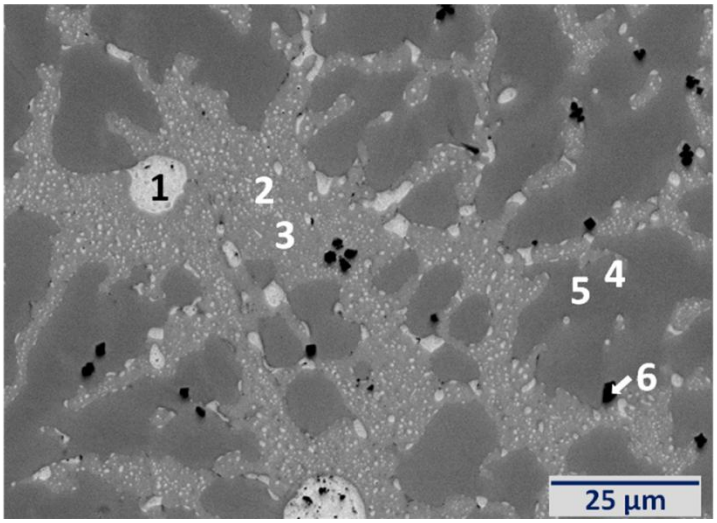

Figure 2.2d SEM BEI images for T10-4, and the chemical compositions of the indexed areas measured by EDS are summarized in Table 2.4.

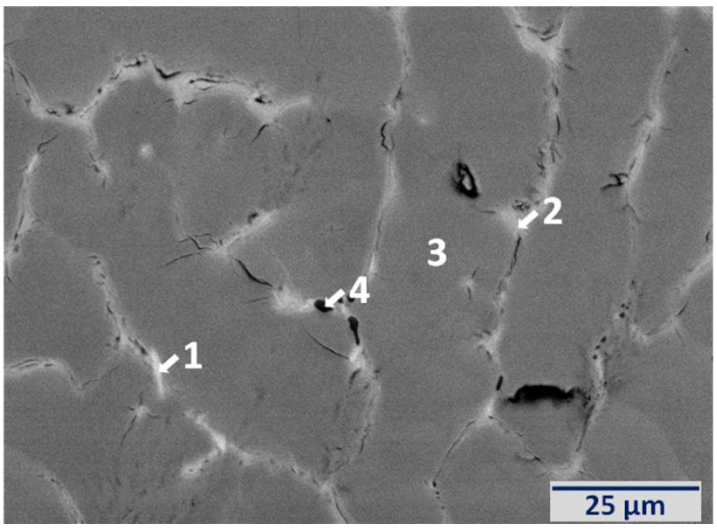

Figure 2.2e SEM BEI images for Z10-1, and the chemical compositions of the indexed areas measured by EDS are summarized in Table 2.4.

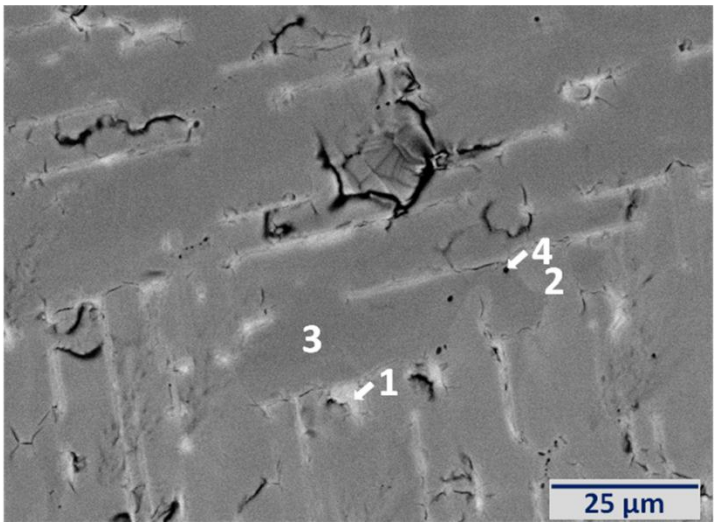

Figure 2.2f SEM BEI images for Z10-2, and the chemical compositions of the indexed areas measured by EDS are summarized in Table 2.4.

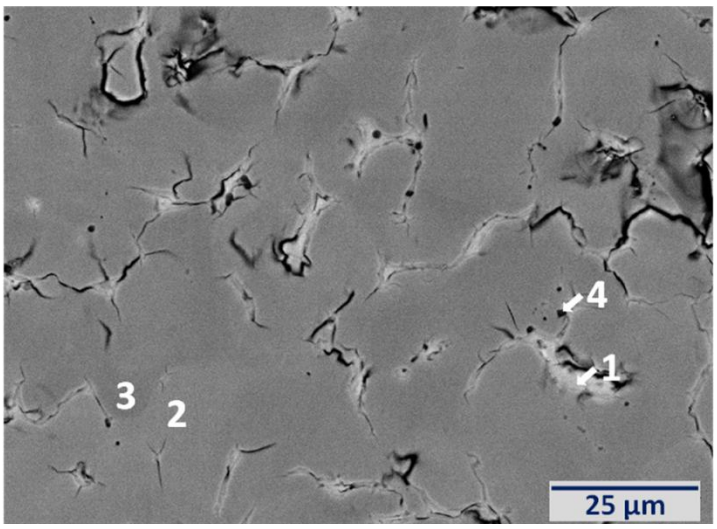

Figure 2.2g SEM BEI images for Z10-3, and the chemical compositions of the indexed areas measured by EDS are summarized in Table 2.4.

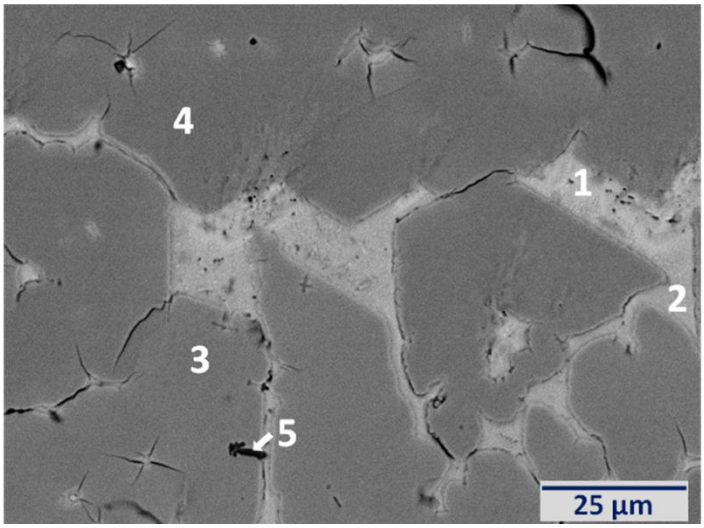

Figure 2.2h SEM BEI images for Z10-4, and the chemical compositions of the indexed areas measured by EDS are summarized in Table 2.4.

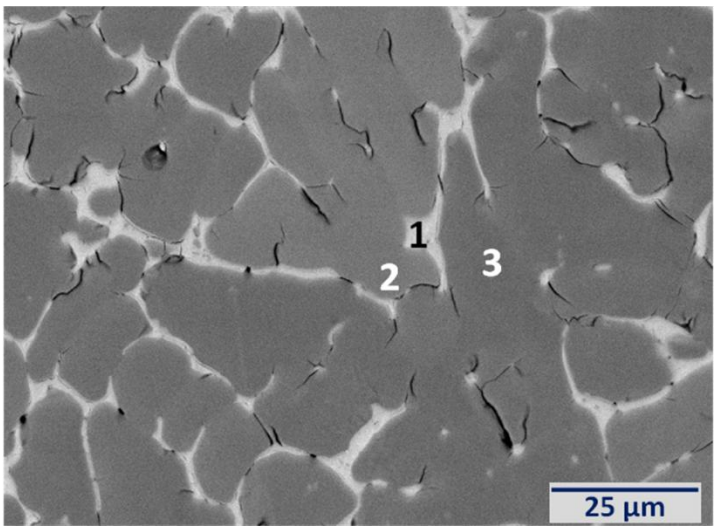

Figure 2.2i SEM BEI images for H10-1, and the chemical compositions of the indexed areas measured by EDS are summarized in Table 2.4.

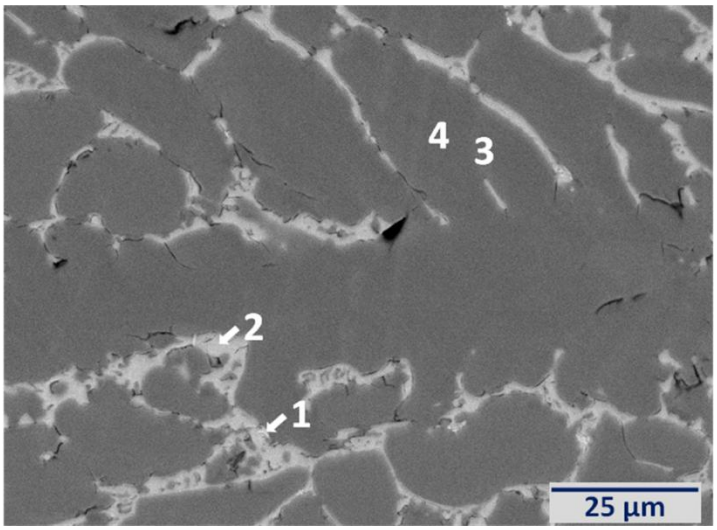

Figure 2.2j SEM BEI images for H10-2, and the chemical compositions of the indexed areas measured by EDS are summarized in Table 2.4.

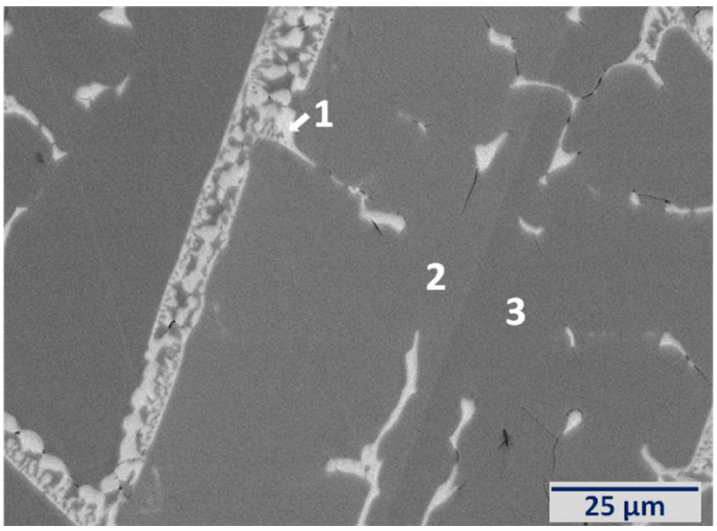

Figure 2.2k SEM BEI images for H10-3, and the chemical compositions of the indexed areas measured by EDS are summarized in Table 2.4.

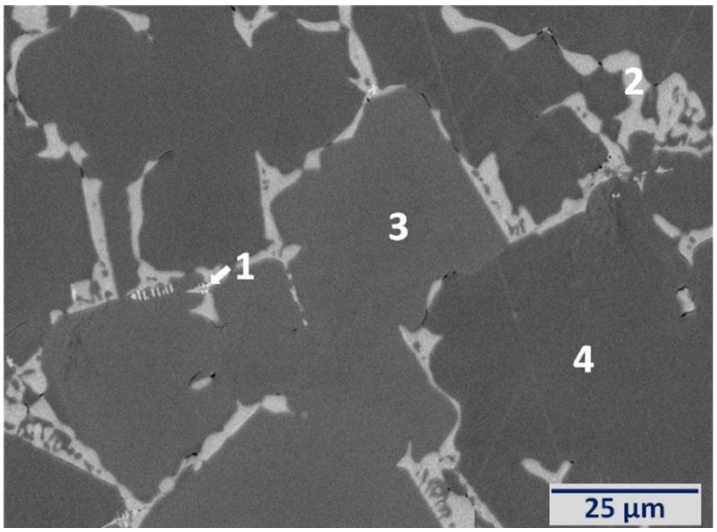

Figure 2.2l SEM BEI images for H10-4, and the chemical compositions of the indexed areas measured by EDS are summarized in Table 2.4.

Table 2.4 Summary of EDS results in at.% from areas identified in SEM BEI micrographs (Figure 2.2a-l)

Alloy name	Area	Ti	Zr	Hf	Cr	Co	Cu	B/A	*e/a*	Phase(s)
T10-1	Figure 2.2a-1	16.2	-	-	25.6	58.2	-	5.2	7.42	Co metal
	Figure 2.2a-2	30.3	-	-	14.7	55.1	-	2.3	7.05	AB_2
	Figure 2.2a-3	40.8	-	-	6.2	53.1	-	1.5	6.78	TiCo
	Figure 2.2a-4	70.3	-	-	6.6	23.1	-	0.4	5.29	TiO_2
T10-2	Figure 2.2b-1	31.1	-	-	5.3	63.6	-	2.2	7.29	AB_2
	Figure 2.2b-2	31.3	-	-	4.6	64.1	-	2.2	7.30	AB_2
	Figure 2.2b-3	40.2	-	-	3.0	56.8	-	1.5	6.90	TiCo
	Figure 2.2b-4	59.8	-	-	3.0	37.3	-	0.7	5.92	TiO_2
T10-3	Figure 2.2c-1	7.8	-	-	-	15.3	76.9	11.8	10.15	Cu metal
	Figure 2.2c-2	32.1	-	-	-	66.4	1.5	2.1	7.43	AB_2
	Figure 2.2c-3	32.2	-	-	-	66.3	1.6	2.1	7.43	AB_2
	Figure 2.2c-4	39.6	-	-	-	58.3	2.1	1.5	7.06	TiCo
	Figure 2.2c-5	67.8	-	-	-	30.6	1.5	0.5	5.63	TiO_2
T10-4	Figure 2.2d-1	1.1	-	-	-	3.7	95.2	89.9	10.85	Cu metal
	Figure 2.2d-2	24.3	-	-	-	49.2	26.6	3.1	8.33	Cu metal + AB_2
	Figure 2.2d-3	29.2	-	-	-	60.7	10.1	2.4	7.74	AB_2
	Figure 2.2d-4	37.5	-	-	-	55.6	7.0	1.7	7.27	AB_2 + TiCo
	Figure 2.2d-5	40.7	-	-	-	53.8	5.5	1.5	7.08	TiCo

	Figure 2.2d-6	86.8	-	-	-	9.5	3.7	0.2	4.73	TiO_2
Z10-1	Figure 2.2e-1	-	65.3	-	6.0	28.7	-	0.5	5.56	Zr_2Co
	Figure 2.2e-2	-	50.6	-	2.2	47.2	-	1.0	6.40	ZrCo
	Figure 2.2e-3	-	31.8	-	35.2	33.0	-	2.1	6.35	AB_2
	Figure 2.2e-4	-	76.4	-	10.1	13.5	-	0.3	4.88	ZrO_2
Z10-2	Figure 2.2f-1	-	50.4	-	1.8	47.8	-	1.0	6.43	ZrCo
	Figure 2.2f-2	-	31.9	-	27.6	40.5	-	2.1	6.58	AB_2
	Figure 2.2f-3	-	31.3	-	28.7	40.0	-	2.2	6.57	AB_2
	Figure 2.2f-4	-	51.0	-	16.2	32.8	-	1.0	5.96	ZrO_2
Z10-3	Figure 2.2g-1	-	49.4	-	2.1	48.5	-	1.0	6.47	ZrCo
	Figure 2.2g-2	-	33.2	-	17.1	49.7	-	2.0	6.83	AB_2
	Figure 2.2g-3	-	32.0	-	19.8	48.3	-	2.1	6.82	AB_2
	Figure 2.2g-4	-	63.9	-	9.3	26.8	-	0.6	5.53	ZrO_2
Z10-4	Figure 2.2h-1	-	50.2	-	0.5	49.2	-	1.0	6.47	ZrCo
	Figure 2.2h-2	-	50.1	-	0.7	49.2	-	1.0	6.47	ZrCo
	Figure 2.2h-3	-	32.2	-	12.3	55.5	-	2.1	7.02	AB_2
	Figure 2.2h-4	-	32.0	-	12.4	55.6	-	2.1	7.03	AB_2
	Figure 2.2h-5	-	63.1	-	6.6	30.3	-	0.6	5.65	ZrO_2
H10-1	Figure 2.2i-1	-	-	49.8	2.2	48.0	-	1.0	6.44	HfCo
	Figure 2.2i-2	-	-	33.3	28.4	38.3	-	2.0	6.48	AB_2

	Figure 2.2i-3	-	-	33.0	29.1	37.9	-	2.0	6.48	AB_2
	Figure 2.2i-4	-	-	26.3	17.7	56.0	-	2.8	7.15	Hf_2Co_7
H10-2	Figure 2.2j-1	-	-	64.8	6.4	28.8	-	0.5	5.57	Hf_2Co
	Figure 2.2j-2	-	-	49.5	2.0	48.5	-	1.0	6.47	HfCo
	Figure 2.2j-3	-	-	33.2	18.7	48.1	-	2.0	6.78	AB_2
	Figure 2.2j-4	-	-	32.8	21.8	45.4	-	2.0	6.71	AB_2
H10-3	Figure 2.2k-1	-	-	49.7	0.9	49.4	-	1.0	6.49	HfCo
	Figure 2.2k-2	-	-	33.0	12.4	54.7	-	2.0	6.99	AB_2
	Figure 2.2k-3	-	-	32.8	12.7	54.5	-	2.0	6.98	AB_2
H10-4	Figure 2.2l-1	-	-	76.6	0.5	22.9	-	0.3	5.16	Hf metal
	Figure 2.2l-2	-	-	49.4	0.4	50.2	-	1.0	6.52	HfCo
	Figure 2.2l-3	-	-	32.8	5.1	62.2	-	2.1	7.22	AB_2
	Figure 2.2l-4	-	-	32.9	4.9	62.3	-	2.0	7.22	AB_2

As discussed in the XRD phase analysis section, the EDS result of the secondary phase was combined with the phase abundance analyzed by XRD and overall composition to calculate the actual composition and *e*/*a* of the AB_2 phase for each alloy in T10-, Z10-, and H10-series and, and the calculated result is listed in Table 2.5 together with the design composition and the EDS result of the AB_2 phase for comparison. The EDS results of the AB_2 phases are not used for further correlation because EDS only provides the composition of a small portion of the main phase. By combining the phase abundance examined by XRD, the more overall and wider range nature of XRD analysis offers a more accurate calculation for the true composition of the AB_2 phase. As seen in Table 2.5, the difference between the calculated *e*/*a* value and the EDS result of the AB_2 phase is negligible for each alloy in T10-, Z10-, and H10-series. The deviation from the calculated *e*/*a* value to the design is also minimal except for T10-4 due to the large amount of TiCo formation.

Table 2.5 Comparison among design composition, EDS result, and calculated composition of the AB_2 phase. All compositions are in at.%.

Alloy name		**Ti**	**Zr**	**Hf**	**Cr**	**Co**	**Cu**	***e*/*a***
T10-1	Design	33.3	-	-	11.1	55.6	-	7.00
	EDS	30.3	-	-	14.7	55.1	-	7.05
	Calculated	31.4	-	-	12.4	56.2	-	7.06
T10-2	Design	33.3	-	-	4.5	62.2	-	7.20
	EDS	31.1	-	-	5.3	63.6	-	7.29
	Calculated	32.3	-	-	4.7	63.0	-	7.25
T10-3	Design	33.3	-	-	-	63.3	3.3	7.40
	EDS	32.1	-	-	-	66.4	1.5	7.43
	Calculated	32.0	-	-	-	64.4	3.6	7.47

T10-4	Design	33.3	-	-	-	53.3	13.3	7.60
	EDS	29.2	-	-	-	60.7	10.1	7.74
	Calculated	26.9	-	-	-	66.4	6.7	7.79
Z10-1	Design	-	33.3	-	31.1	35.6	-	6.40
	EDS	-	31.8	-	35.2	33.0	-	6.35
	Calculated	-	33.1	-	31.6	35.4	-	6.40
Z10-2	Design	-	33.3	-	24.5	42.2	-	6.60
	EDS	-	31.9	-	27.6	40.5	-	6.58
	Calculated	-	32.8	-	25.1	42.1	-	6.61
Z10-3	Design	-	33.3	-	17.8	48.9	-	6.80
	EDS	-	32.0	-	19.8	48.3	-	6.82
	Calculated	-	32.9	-	18.2	48.9	-	6.81
Z10-4	Design	-	33.3	-	11.1	55.6	-	7.00
	EDS	-	32.2	-	12.3	55.5	-	7.02
	Calculated	-	32.7	-	11.5	55.8	-	7.02
H10-1	Design	-	-	33.3	24.5	42.2	-	6.60
	EDS	-	-	33.3	28.4	38.3	-	6.48
	Calculated	-	-	32.8	25.2	42.0	-	6.60
H10-2	Design	-	-	33.3	17.8	48.9	-	6.80
	EDS	-	-	33.2	18.7	48.1	-	6.78
	Calculated	-	-	32.2	18.9	48.9	-	6.82
H10-3	Design	-	-	33.3	11.1	55.6	-	7.00
	EDS	-	-	33.0	12.4	54.7	-	6.99
	Calculated	-	-	31.9	12.0	56.1	-	7.05
H10-4	Design	-	-	33.3	4.4	62.2	-	7.20
	EDS	-	-	32.8	5.1	62.2	-	7.22
	Calculated	-	-	32.0	4.8	63.2	-	7.26

2.2.3 C14/C15 phase abundance vs. *e*/*a*

The C14/C15 phase abundance in the AB_2 Laves phases as a function of *e*/*a* is constructed and presented in Figure 2.3. It should be noted that for T10-, Z10-, and H10-series, the calculated *e*/*a* values are used; for all other series, the design *e*/*a* values are used. The abundance of C14 decreases as *e*/*a* increases in every series. In the observed *e*/*a* range, TZ11-series demonstrates a linear relationship between C14/C15 phase abundance and *e*/*a*, with 100% C14 and 100% C15 at *e*/*a* of 6.8 and 7.2, respectively. TZ37-series shows 100% C14 and 100% C15 at the same *e*/*a* values as TZ11, however the C14 abundance decreases in an exponential decay fashion with respect to *e*/*a*. The relationship between C14/C15 phase abundance and *e*/*a* of TZ73-series is a perfect rotational symmetry of that of TZ37 across the trend seen in TZ11.

As the Ti-content further increases to 100% (T10-series) in A-site from TZ73, an increase in *e*/*a* to 7.06 is needed to achieve 100% C14 and the C14 abundance decreases more rapidly compared to alloys with Ti + Zr mixture in A-site. When the A-site composition becomes 100% Zr (Z10-series), the curve is moved to a much lower *e*/*a* value (6.40) for 100% C14, and the curve trend is similar to that in T10. The A-site composition of 100% Hf (H10), which is in the same group as Ti and Zr, shows a similar curve trend as in T10 and Z10, and the curve lands right in between T10 and Z10 (100% C14 at *e*/*a* of 6.60).

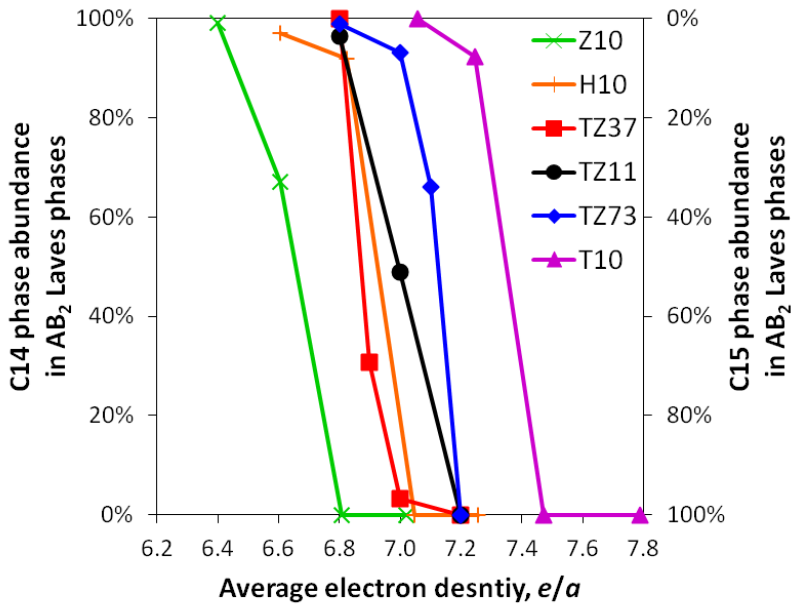

Figure 2.3 Correlation between the C14/C15 phase abundance in the AB_2 Laves phases and the average electron density

2.2.4 Parameters in controlling C14/C15 threshold

Figure 2.3 illustrates a close relationship between the C14/C15 abundance and *e*/*a*. However, some other factor is in play and causes the shift in *e*/*a* as the A-site composition, which is composed of elements with the same number of outer-shell electrons, changes. The investigation continues by obtaining *e*/*a* at the C14/C15 threshold (C14 : C15 = 1 : 1) of each series from Figure 2.3. *e*/*a* at the C14/C15 threshold is plotted against the average atomic radius of A atoms in Laves phases (r_A) (since A atoms are much larger than B atoms, the geometric contribution from B atoms is negligible) in Figure 2.4 and shows a significant correlation (R^2 = 0.9436). This result seems to be consistent with that geometric factor plays an important role in the stability of different Laves phases [42-47, 81]. However, the C14/C15 threshold of H10 falls out of the fitted function of the atomic radius in Laves phases, and therefore Vegard's law is

responsible for the strong correlation demonstrated. A more improved correlation to predict the C14/C15 threshold is desirable.

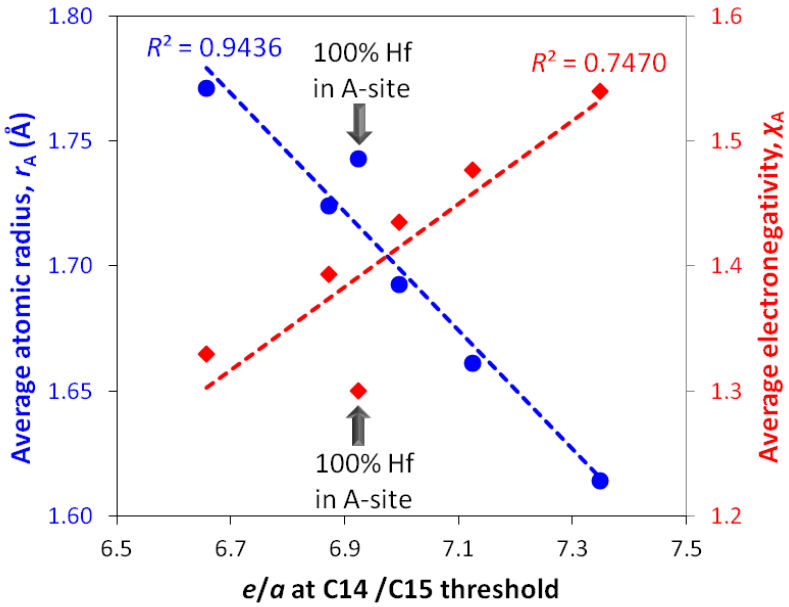

Figure 2.4 Correlations between *e*/*a* at the C14/C15 threshold and both the average atomic radius of A atoms and the average electronegativity of A atoms

The square of the difference in electronegativities of the A and B atoms has been used to standardize and fit atomic contractions as a function of the R_A/R_B ratio [48]. *e*/*a* at the C14/C15 threshold is correlated with the average electronegativity of A atoms (χ_A), χ_A^2, and the square of the difference in average electronegativity of A atoms and B atoms ($(\Delta\chi)^2$), and the relationship between the C14/C15 threshold and χ_A is shown in Figure 2.4. The correlation factors for χ_A, χ_A^2, and $(\Delta\chi)^2$ are 0.7470, 0.7613, and 0.5098, respectively, and demonstrate less significant correlations to the C14/C15 threshold due to the inconsistency seen in H10 . Since the correlation about the electronegativity was established with the geometric factor in the previous study, however it was shown that the correlation between the C14/C15 threshold and the r_A/r_B

ratio is only strong in the region where Vegard's law is in play, it's proven indirectly that the electronegativity is not a desirable parameter in describing the trend in C14/C15 threshold.

Regarding the C14/C15 structure transition, thus far the closest correlation was established between the curve of C14/C15 structure vs. the number of the valence electrons per AB_2 unit and the curve of the energy difference between cubic- and hexagonal-structures calculated by a tight-binding calculation [39]. Since the structural energy is related to the collection of the potential energies participates within the structure, the chemical potential for electronic charge can potentially be used to correlate the C14/C15 transition behavior. e/a at the C14/C15 threshold is plotted against the average chemical potential for electronic charge of A atoms (ϕ^*_A) in Figure 2.5. Only the contribution from the A-site is considered due to the similarities in B-site compositions among all alloys. A nearly perfect linear relationship (R^2 = 0.9969) indicates that an accurate prediction of C14/C15 threshold of any AB_2 alloy can be made by the correlation

$$\textbf{\textit{e/a} at C14/C15 threshold} = 1.9605\phi^*_A - 0.1115 \qquad (2.1)$$

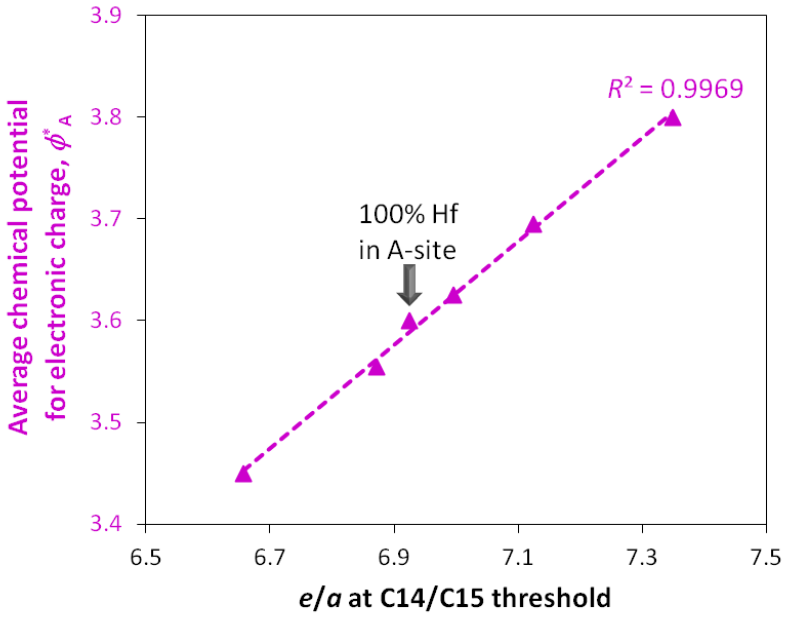

Figure 2.5 Correlation between *e*/*a* at the C14/C15 threshold and the average chemical potential for electronic charge of A atoms

2.3 Summary

In order to optimize the electrochemical properties of the AB_2 MH alloy by estimating the C14/C15 phase abundance from the chemical composition, a systematic study to acquire a model that predicts the C14/C15 transition threshold was established. Within the applicable *e*/*a* range for the negative materials used in Ni/MH battery, each series of alloys demonstrated a decrease in C14 phase abundance (an increase in C15 phase abundance) as *e*/*a* increased. However, when comparing series to series (with different A-site compositions), *e*/*a* alone cannot predict the exact C14/C15 phase abundance due to the shift in *e*/*a* as the composition in the A-site varied. The average atomic radius of A atoms was shown to be able to compensate for the shift in *e*/*a* for all Ti + Zr systems (pure or mixed), but failed when a third atom, Hf with the same number of outer-shell electrons as Ti and Zr, was included. The average chemical potential for electronic charge of A atoms provided a reasonable model for predicting the

C14/C15 threshold. The combination of *e*/*a* and the average chemical potential for electronic charge was established for the C14/C15 phase abundance prediction to assist the future AB_2 MH alloy development.

CHAPTER 3

GASEOUS PHASE HYDROGEN STORAGE AND ELECTROCHEMICAL PROPERTIES OF Zr_8Ni_{21}, Zr_7Ni_{10}, Zr_9Ni_{11}, AND ZrNi METAL HYDRIDE ALLOYS

A thorough and systematic examination of four non-Laves phase alloys, Zr_8Ni_{21}, Zr_7Ni_{10}, Zr_9Ni_{11}, and ZrNi, that correlates composition, structure, gaseous phase hydrogen storage, and electrochemical properties was established. Furthermore, due to the importance of the synergetic effect observed in AB_2 alloys, the effect of secondary phases in the close-related non-Laves phase alloys is investigated by adopting an annealing treatment.

Four alloys, Zr_8Ni_{21} (ZN0821), Zr_7Ni_{10} (ZN0710), Zr_9Ni_{11} (ZN0911), and ZrNi (ZN0101) were prepared, and the design compositions are listed in Table 3.1. The annealed ZN0821, ZN0710, ZN0911, and ZN0101 were designated as ZN0821A, ZN0710A, ZN0911A, and ZN0101A, respectively. With the lowest eutectic temperature of around 1070 °C in the neighborhood, an annealing temperature of 1000 °C was chosen for all alloy compositions to prevent partial melting during annealing. After being annealed at 1000 °C for 4 h, the XRD feature of annealed ZN0821 was the same as that of the unannealed ZN0821, which indicated longer annealing period but less intense temperature condition was required in this case. Therefore, annealing at 960 °C for 8 h was adopted to generate ZN0821A sample.

Table 3.1 Design compositions and ICP results in at.%

Alloy name		Zr	Ni
ZN0821	Design	27.6	72.4
	ICP as-cast	26.9	73.1
	ICP annealed	27.1	72.9
ZN0710	Design	41.2	58.8
	ICP as-cast	40.2	59.8
	ICP annealed	40.2	59.8
ZN0911	Design	45.0	55.0
	ICP as-cast	43.9	56.1
	ICP annealed	44.0	56.0
ZN0101	Design	50.0	50.0
	ICP as-cast	49.0	51.0
	ICP annealed	49.3	50.7

3.1 Experimental setup

Four alloys, Zr_8Ni_{21}, Zr_7Ni_{10}, Zr_9Ni_{11}, and ZrNi were prepared with raw materials from 99.999% purity metals. The sample alloys were prepared by arc melting under a continuous argon flow with a non-consumable tungsten electrode and a water-cooled copper tray. Before each arc melt, a piece of sacrificial titanium underwent a few melting-cooling cycles to reduce the residual oxygen concentration in the system. Each 10-g sample ingot was re-melted and flipped over a few times to ensure uniformity in chemical composition. Half of each sample ingot was annealed at 1000 °C for 4 h in an argon environment except for Zr_8Ni_{21}, which was annealed at 960 °C for 8 h in the same environment.

The chemical composition of each sample alloy was examined with a Varian *Liberty* 100 inductively coupled plasma (ICP) system. A Rigaku *Miniflex* XRD was used to study each alloy's microstructure. A JEOL *JSM6320F* SEM with EDS capability was used to study the phase distribution and composition. Sample alloys for SEM/EDS analysis were mounted and polished on epoxy blocks, rinsed and dried before entering the SEM chamber.

The gaseous phase hydrogen storage characteristics were studied by pressure-concentration-temperature (PCT) isotherm measurement using a Suzuki-Shokan 4-channel PCT system. Each sample alloy was first activated by a 2-h thermal cycle between 300 °C and room temperature under 2.5 MPa H_2 pressure. The PCT isotherms at 30, 60, and 90 °C were then measured. For the unannealed and annealed ZrNi samples, one additional PCT isotherm at 120 °C was measured for each.

To prepare for the electrochemical measurements, each sample ingot was first ground and sized using a 200-mesh sieve. The sieved powder was then compacted onto an expanded nickel substrate by a 10-ton press to form a test electrode (about 1 cm^2 in size and 0.2 mm thick) without any binder. The electrochemical properties of these electrodes were measured in a flooded cell configuration using a partially pre-charged $Ni(OH)_2$ pasted counter electrode as the positive electrode and a 30 wt.% KOH solution as the electrolyte. For the discharge capacity measurement, the system was first charged at a current density of 50 mA g^{-1} for 10 h and then discharged at a current density of 50 mA g^{-1} until a cut-off voltage of –0.9 V was reached, then discharged at a current density of 12 mA g^{-1} until a cut-off voltage of –0.9 V was reached, and finally discharged at a current density of 4 mA g^{-1} until a cut-off voltage at –0.9 V was reached. All electrochemical measurements were performed in an Arbin Instruments *BT4+* Portable Battery Test System.

In order to study the reaction between the surface oxide and the KOH electrolyte, hot alkaline etching experiments were conducted. Two etching conditions, 2 and 4 h in 7 ml of 30 wt.% KOH at 100 °C, were applied for each sample alloy. Each condition was performed on 1 g of –200-mesh powder in a glass vial. The concentration of metal components in the solute at the end of each etching treatment was studied by ICP. For the magnetic susceptibility measurement, dried 2- and 4-h etched powders together with the virgin powder (0-h) for each sample alloy were analyzed by a Quantum Design *MPMS-5T* SQUID magnetometer, which requires sample size of 30 to 35 mg.

3.2 Results and discussion

3.2.1 XRD structure and SEM/EDS phase analyses

ICP analysis showed that the compositions of ZN0821, ZN0710, ZN0911, and ZN0101 are very close to their design values (Table 3.1). The compositions of the alloys after annealing are also similar to their design values (Table 3.1). The microstructures of the eight samples (four before annealing and four after annealing) were studied using XRD, and the XRD patterns are displayed in Figure 3.1. The microstructures were further studied by SEM, with which both the secondary electron images (SEI) and BEI were taken. The BEI micrographs with the same magnification are presented in Figure 3.2a-h. With the help of surface morphology analysis (done by examining the SEI micrographs), the compositions in several areas (identified numerically in the micrographs) with different BEI contrasts were studied using EDS and the results are listed in Table 3.2. Combining the XRD and SEM/EDS results, the phase analyses of all samples, before and after annealing, are presented in the following sections and summarized in Table 3.3.

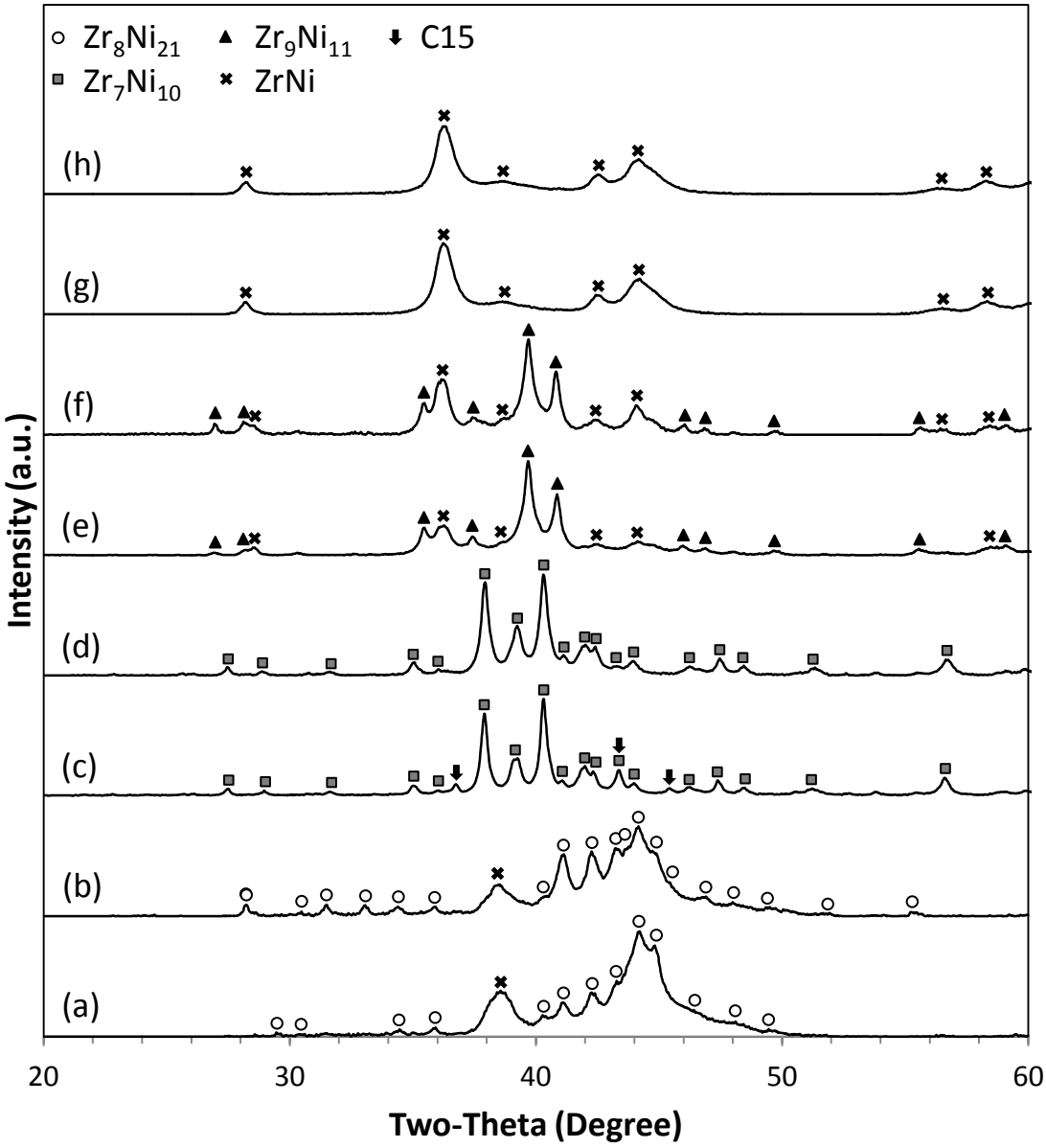

Figure 3.1 XRD patterns using Cu-K_α as the radiation source for alloys ZN0821 (a), ZN0821A (b), ZN0710 (c), ZN0710A (d), ZN0911 (e), ZN0911A (f), ZN0101 (g), and ZN0101A (h).

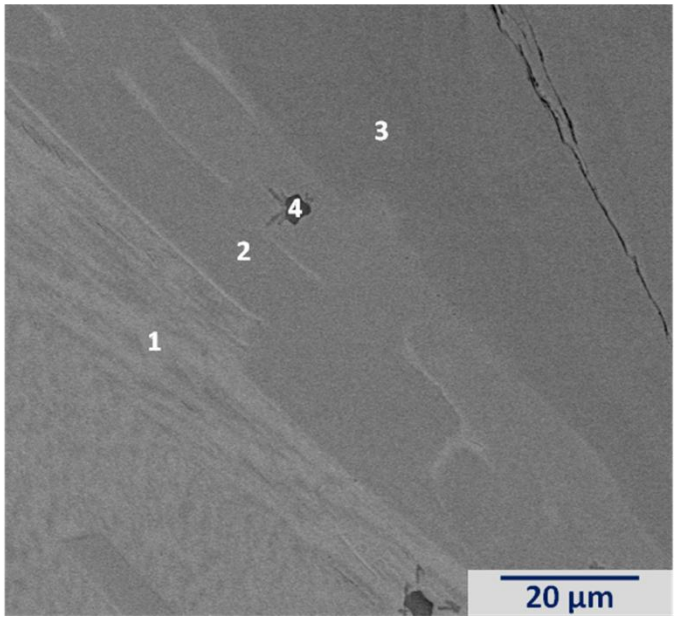

Figure 3.2a SEM BEI with 1000× magnification for ZN0821, and the chemical compositions of the indexed areas measured by EDS are summarized in Table 3.2.

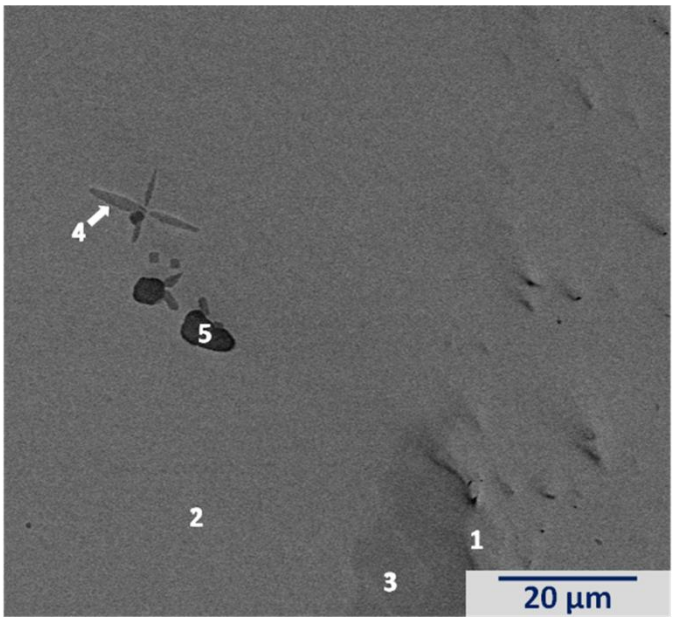

Figure 3.2b SEM BEI with 1000× magnification for ZN0821A, and the chemical compositions of the indexed areas measured by EDS are summarized in Table 3.2.

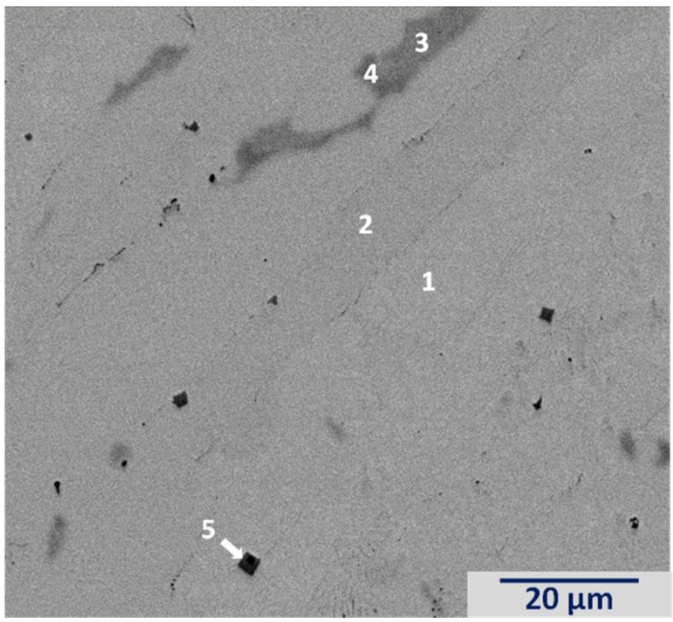

Figure 3.2c SEM BEI with 1000× magnification for ZN0710, and the chemical compositions of the indexed areas measured by EDS are summarized in Table 3.2.

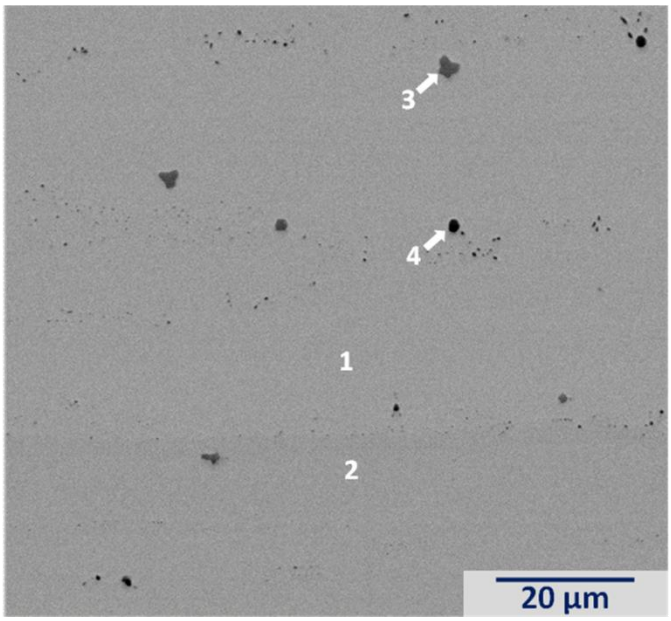

Figure 3.2d SEM BEI with 1000× magnification for ZN0710A, and the chemical compositions of the indexed areas measured by EDS are summarized in Table 3.2.

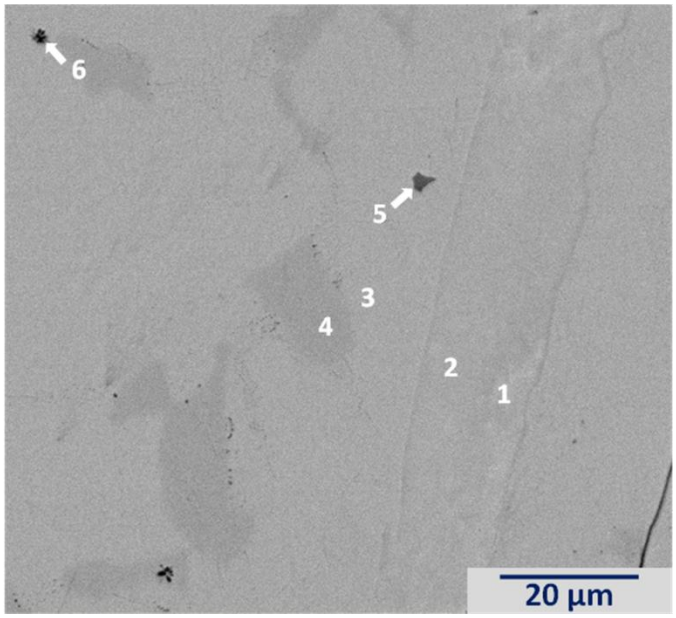

Figure 3.2e SEM BEI with 1000× magnification for ZN0911, and the chemical compositions of the indexed areas measured by EDS are summarized in Table 3.2.

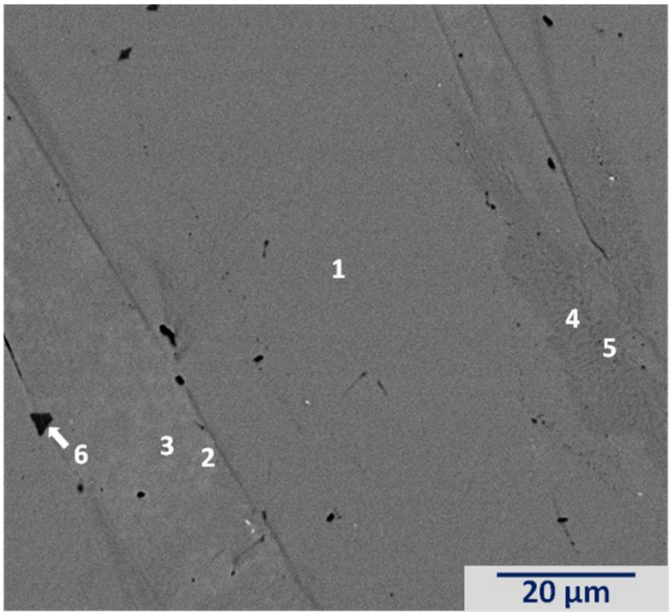

Figure 3.2f SEM BEI with 1000× magnification for ZN0911A, and the chemical compositions of the indexed areas measured by EDS are summarized in Table 3.2.

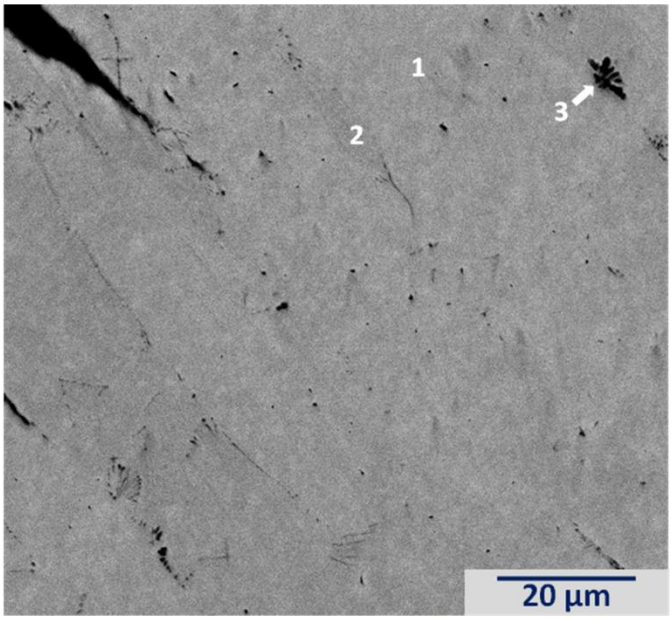

Figure 3.2g SEM BEI with 1000× magnification for ZN0101, and the chemical compositions of the indexed areas measured by EDS are summarized in Table 3.2.

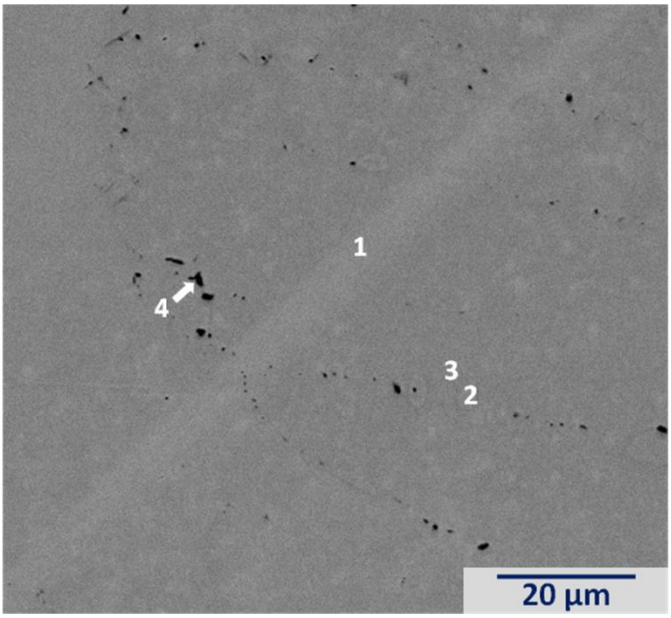

Figure 3.2h SEM BEI with 1000× magnification for ZN0101A, and the chemical compositions of the indexed areas measured by EDS are summarized in Table 3.2.

Table 3.2 Summary of EDS results in at.% from areas identified in SEM BEI micrographs (Figure 3.2a-h)

Alloy name	Area	Zr	Ni	Zr/Ni	*e/a*	Phase(s)
ZN0821	Figure 3.2a-1	41.39	58.61	0.71	7.52	Zr_8Ni_{21} + ZrNi
	Figure 3.2a-2	28.14	71.86	0.39	8.31	Zr_8Ni_{21}
	Figure 3.2a-3	22.77	77.23	0.29	8.63	Zr_8Ni_{21} + $ZrNi_5$
	Figure 3.2a-4	96.23	3.77	25.53	4.23	ZrO_2
ZN0821A	Figure 3.2b-1	36.51	63.49	0.58	7.81	Zr_8Ni_{21} + ZrNi
	Figure 3.2b-2	30.5	69.5	0.44	8.17	Zr_8Ni_{21} + ZrNi
	Figure 3.2b-3	26.78	73.22	0.37	8.39	Zr_8Ni_{21}
	Figure 3.2b-4	17.52	82.48	0.21	8.95	$ZrNi_5$
	Figure 3.2b-5	96.51	3.49	27.65	4.21	ZrO_2
ZN0710	Figure 3.2c-1	41.2	58.8	0.70	7.53	Zr_7Ni_{10}
	Figure 3.2c-2	41.2	58.8	0.70	7.53	Zr_7Ni_{10}
	Figure 3.2c-3	34.8	65.2	0.53	7.91	C15
	Figure 3.2c-4	32.2	67.8	0.47	8.07	C15
	Figure 3.2c-5	89.4	10.6	8.43	4.64	ZrO_2
ZN0710A	Figure 3.2d-1	41.1	58.9	0.70	7.53	Zr_7Ni_{10}
	Figure 3.2d-2	41.1	58.9	0.70	7.53	Zr_7Ni_{10}
	Figure 3.2d-3	92	8	11.50	4.48	ZrO_2
	Figure 3.2d-4	73	27	2.70	5.62	ZrO_2
ZN0911	Figure 3.2e-1	50.1	49.9	1.00	6.99	ZrNi
	Figure 3.2e-2	49.9	50.1	1.00	7.01	ZrNi
	Figure 3.2e-3	44.2	55.8	0.79	7.35	Zr_9Ni_{11}
	Figure 3.2e-4	41.7	58.3	0.72	7.5	Zr_7Ni_{10}
	Figure 3.2e-5	87.6	12.4	7.06	4.74	ZrO_2
	Figure 3.2e-6	71.2	28.8	2.47	5.73	ZrO_2
ZN0911A	Figure 3.2f-1	44.5	55.5	0.80	7.33	Zr_9Ni_{11}

	Figure 3.2f-2	49.9	50.1	1.00	7.01	ZrNi
	Figure 3.2f-3	49.8	50.2	0.99	7.01	ZrNi
	Figure 3.2f-4	44	56	0.79	7.36	Zr_9Ni_{11}
	Figure 3.2f-5	47.2	52.8	0.89	7.17	Zr_9Ni_{11} + ZrNi
	Figure 3.2f-6	95.4	4.6	20.74	4.28	ZrO_2
ZN0101	Figure 3.2g-1	49.7	50.3	0.99	7.02	ZrNi
	Figure 3.2g-2	44.7	55.3	0.81	7.32	Zr_9Ni_{11}
	Figure 3.2g-3	67.5	32.6	2.07	5.96	ZrO_2
ZN0101A	Figure 3.2h-1	50.1	49.9	1.00	6.99	ZrNi
	Figure 3.2h-2	44.6	55.4	0.81	7.32	Zr_9Ni_{11}
	Figure 3.2h-3	49.9	50.1	1.00	7.01	ZrNi
	Figure 3.2h-4	64.1	35.9	1.79	6.15	ZrO_2

Table 3.3 Summary of XRD and EDS results

Alloy name	Major phase	Main secondary phase	Annealing effect
ZN0821	Zr_8Ni_{21} (triclinic)	ZrNi (orthorhombic)	Decreases the amount of ZrNi.
ZN0821A	Zr_8Ni_{21} (triclinic)	ZrNi (orthorhombic)	
ZN0710	Zr_7Ni_{10} (orthorhombic)	C15 (face-center-cubic)	Eliminates C15.
ZN0710A	Zr_7Ni_{10} (orthorhombic)	-	
ZN0911	Zr_9Ni_{11} (tetragonal)	ZrNi (orthorhombic)	Increases the amount of ZrNi.
ZN0911A	Zr_9Ni_{11} (tetragonal)	ZrNi (orthorhombic)	
ZN0101	ZrNi (orthorhombic)	Zr_9Ni_{11} (tetragonal)	Decreases the amount of Zr_9Ni_{11}.
ZN0101A	ZrNi (orthorhombic)	Zr_9Ni_{11} (tetragonal)	

3.2.1.1 Zr_8Ni_{21} alloy

The inter-metallic compound Zr_8Ni_{21} has a triclinic crystal structure [82, 83]. As seen in Figure 3.1a, the majority of XRD peaks from ZN0821 belong to the Zr_8Ni_{21} structure. When compared to the XRD pattern from Hf_8Ni_{21}, which is isotropic to Zr_8Ni_{21} [82, 83], an additional broad peak at around 38.5° is observed. Similar broad peaks were found in previous studies and assigned to the (1 1 1) peak at around 36.5° of the orthorhombic ZrNi phase [16, 84] by Young et al. [10, 26, 85]. The shift of the (1 1 1) ZrNi peak to a higher angle in the current study may be a result of the hyper-stoichiometry in ZrNi caused by the higher Ni-content in the overall alloy composition. Since the peak of ZrNi is broad, the ZrNi crystallites are smaller than the resolution of the SEM instrument and thus cannot be identified in the SEM micrograph (Figure 3.2a). However, the relatively higher Zr/Ni ratio in area 1 (0.71 vs. 0.38 in Zr_8Ni_{21}) indicates that the ZrNi grains are distributed within the Zr_8Ni_{21} matrix. While $ZrNi_5$ is not detected by XRD, area 3 is suspected to be a mixture of Zr_8Ni_{21} and $ZrNi_5$ based on its relatively lower Zr/Ni ratio (0.29) and the discovery of $ZrNi_5$ existence in the annealed alloy discussed later in this section. In summary, the microstructure of the as-cast ZN0821 is mainly Zr_8Ni_{21} phase with very fine ZrNi and $ZrNi_5$ crystallites imbedded in the Zr_8Ni_{21} matrix in some areas.

After annealing, the Zr_8Ni_{21} phase predominates the microstructure (Figure 3.1b). Although the broad peak at around 38.5° still exists, its intensity is lower than the one prior to annealing, and the intensities of other peaks increase after annealing. Since annealing decreases the amount of secondary phases, the XRD results before and after annealing together further prove that the broad peak at around 38.5° does not belong to the Zr_8Ni_{21} family. In addition, the XRD result of ZN0821A is very similar to the XRD pattern of the annealed Zr_8Ni_{21} alloy obtained by Ruiz et al. [59]. From the SEM micrograph, the relatively higher Zr/Ni ratios in

areas 1 and 2 show that fine grains of ZrNi are mixed throughout the Zr_8Ni_{21} matrix (Figure 3.2b). Occasionally, dagger-shaped $ZrNi_5$ grains are found in the SEM micrograph (area 4), but its amount is too small to be detected by XRD. This observation confirms that despite not being seen in the micrograph, $ZrNi_5$ exists as fine crystallites in the unannealed alloy. The annealing process promotes the accumulation of the fine $ZrNi_5$ grains, which is evident in the SEM micrograph.

3.2.1.2 Zr_7Ni_{10} alloy

Two crystal structures for the inter-metallic compound Zr_7Ni_{10} have been reported previously: orthorhombic [86, 87] and tetragonal [65-67]. Tetragonal-structured Zr_7Ni_{10} is observed after hydride/dehydride cycling or when prepared by quenching. The XRD pattern of ZN0710 shows an orthorhombic-Zr_7Ni_{10}-predominant structure with FCC C15, one of the Laves phases with a composition of AB_2, being the secondary phase (Figure 3.1c). The SEM micrograph shows that with Zr_7Ni_{10} being the major phase, some trace of a phase with stoichiometry close to AB_2 is also detected by EDS (areas 3 and 4 in Figure 3.2c) and assigned as C15. Similar finding was reported previously [69], and the presence of C15 in unannealed Zr_7Ni_{10} alloy was attributed to the localized non-stoichiometry due to the formation of ZrO_2.

After annealing, the XRD pattern is composed of only peaks from the orthorhombic-structured Zr_7Ni_{10} phase (Figure 3.1d). The SEM micrograph confirms the Zr_7Ni_{10}-predominant nature of ZN0710A with no trace of C15 after annealing (Figure 3.2d).

3.2.1.3 Zr_9Ni_{11} alloy

Before annealing, the XRD pattern of ZN0911 shows a tetragonal-Zr_9Ni_{11}-predominant structure [88, 89] with orthorhombic-structured ZrNi as the main secondary phase (Figure 3.1e). As seen in Figure 1.8, the Zr-Ni binary phase diagram demonstrates that unlike the simple solidification path taken to form Zr_7Ni_{10} and ZrNi, Zr_9Ni_{11} is formed peritectically which begins with an overall liquid composition of Zr : Ni = 9 : 11, follows by the formation of ZrNi, and finally the formation of Zr_9Ni_{11} through the reaction between ZrNi and the remaining liquid. Therefore, the precipitation of ZrNi found in the XRD pattern is a result of incomplete peritectic reaction. Previous study on unannealed Zr_9Ni_{11} also revealed the presence of ZrNi within Zr_9Ni_{11} alloy [71]. The SEM micrograph shows a Zr_9Ni_{11} matrix with ZrNi being the main secondary phase together with occasional Zr_7Ni_{10} inclusions. Although the amount of Zr_7Ni_{10} seems substantial (around 8%), Zr_7Ni_{10} does not exist in ZN0911 according to the XRD pattern. Moreover, in the studies of modifications on AB_2 and A_7B_{10} alloys, ZrNi was found to never coexist with Zr_7Ni_{10} through composition variation [16, 26, 90]. Since the SEM micrographs chosen for the current study are the ones which show the most features, however, do not represent the general feature of the microstructure, the Zr_7Ni_{10} inclusions were suspected to be random occurrences due to the localized imbalance of stoichiometry. Figure 3.3 is the SEM micrograph at the same position but with 10 times lower in magnification of Figure 3.2e and shows that the trace of Zr_7Ni_{10} is in fact very minor in the overall picture (< 1%).

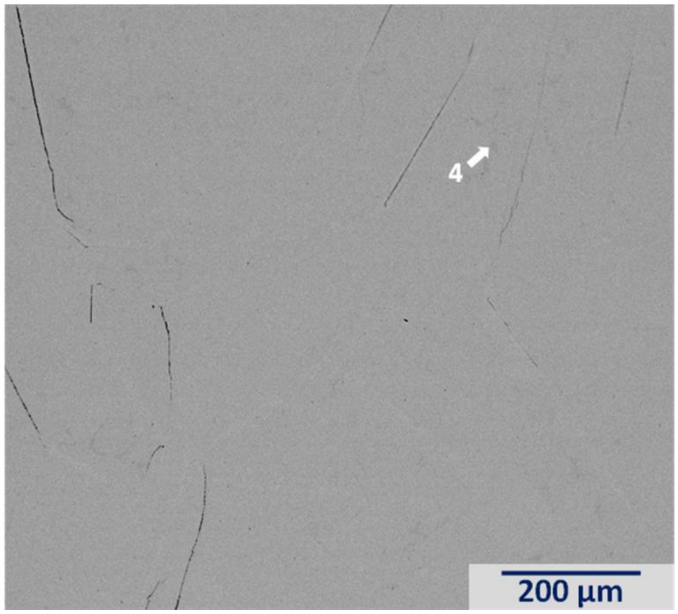

Figure 3.3 SEM BEI with 100× magnification for ZN0911

The XRD pattern of ZN0911A still shows a tetragonal-Zr_9Ni_{11}-predominant structure, however, the annealing treatment increases the amount of the secondary ZrNi phase (Figure 3.1f). This result is consistent with the XRD pattern of the annealed Zr_9Ni_{11} alloy obtained by Ruiz et al. [59]. The SEM micrograph illustrates the increase in ZrNi in the form of either individual ZrNi grain (areas 2 and 3 in Figure 3.2f) or fine ZrNi crystallites mixed within the Zr_9Ni_{11} matrix (area 5 in the same micrograph).

3.2.1.4 ZrNi alloy

The XRD patterns of ZN0101 and ZN0101A have very similar profiles and are both composed of only peaks from the orthorhombic ZrNi phase (Figure 3.1g and h, respectively) [84, 91]. Very small amount of Zr_9Ni_{11} can be found in the SEM micrograph of ZN0101 (Figure 3.2g), but its amount is below the detection limit of XRD analysis. From the comparison of the SEM micrographs, the amount of Zr_9Ni_{11} decreased after annealing (Figure 3.2h).

3.2.2 Gaseous phase PCT analysis

The gaseous phase hydrogen storage characteristics were studied by PCT isotherms measured at 30, 60, and 90 °C. Due to the extremely low plateau pressures of ZN0101 and ZN0101A, one additional PCT isotherm at 120 °C was measured for each alloy. PCT isotherms from ZN0821, ZN0821A, ZN0710, ZN0710A, ZN0911, ZN0911A, ZN0101, and ZN0101A are presented in Figure 3.4a-h. The maximum storage capacity, reversible storage capacity, absorption plateau pressures, and changes in entropy (ΔH) and enthalpy (ΔS) based on the 60 and 90 °C absorption plateau pressures for each alloy are listed in Table 3.4. The absences of plateau regions are observed in some isotherms. One possibility is that the plateau pressure may be extremely low caused by the nature of the alloy and cannot be measured due to the experimental limitation. Another reason for the unrecognized plateau region is that at high temperature, the temperature goes beyond the critical point of the temperature dome formed by connecting the end-points of all pressure plateaus [92] (for example, ZN0821A 90 °C Abs in Figure 3.4b).

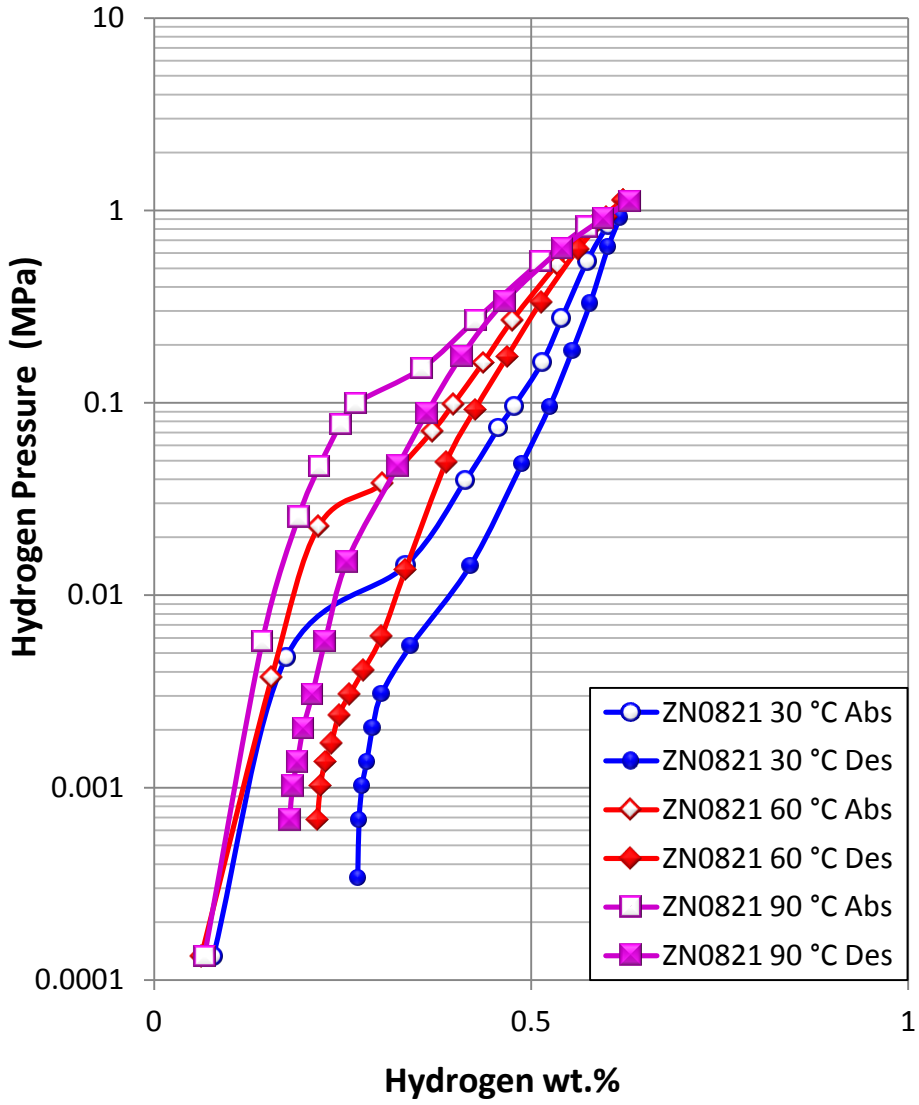

Figure 3.4a PCT isotherms of ZN0821, and open and solid symbols are for absorption and desorption curves, respectively.

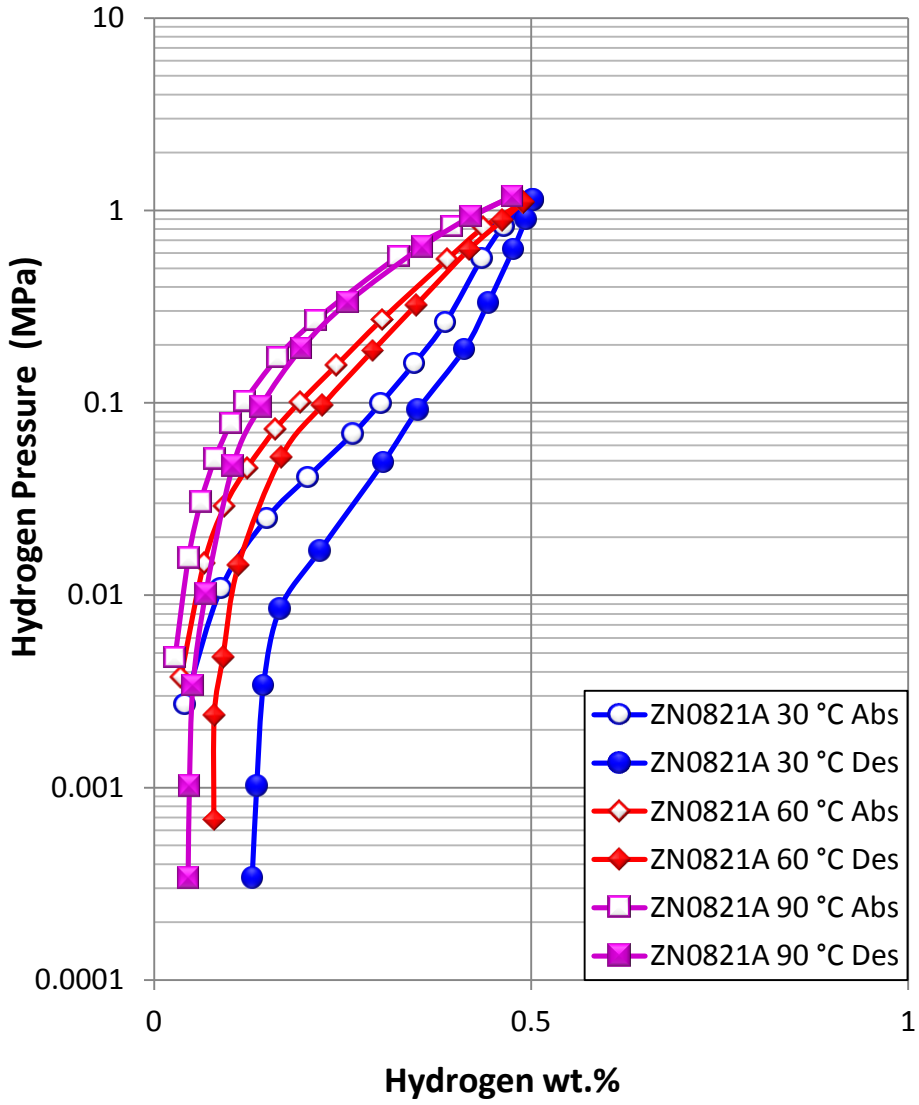

Figure 3.4b PCT isotherms of ZN0821A, and open and solid symbols are for absorption and desorption curves, respectively.

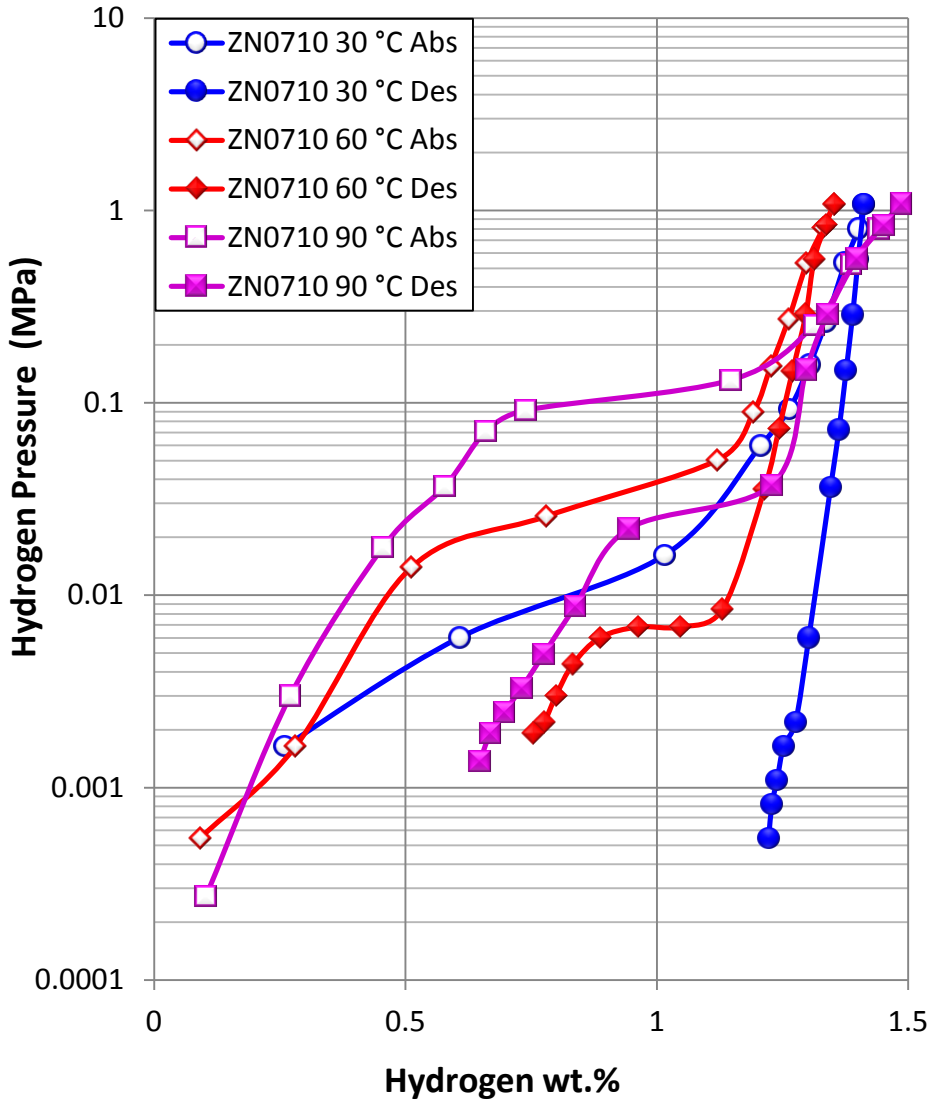

Figure 3.4c PCT isotherms of ZN0710, and open and solid symbols are for absorption and desorption curves, respectively.

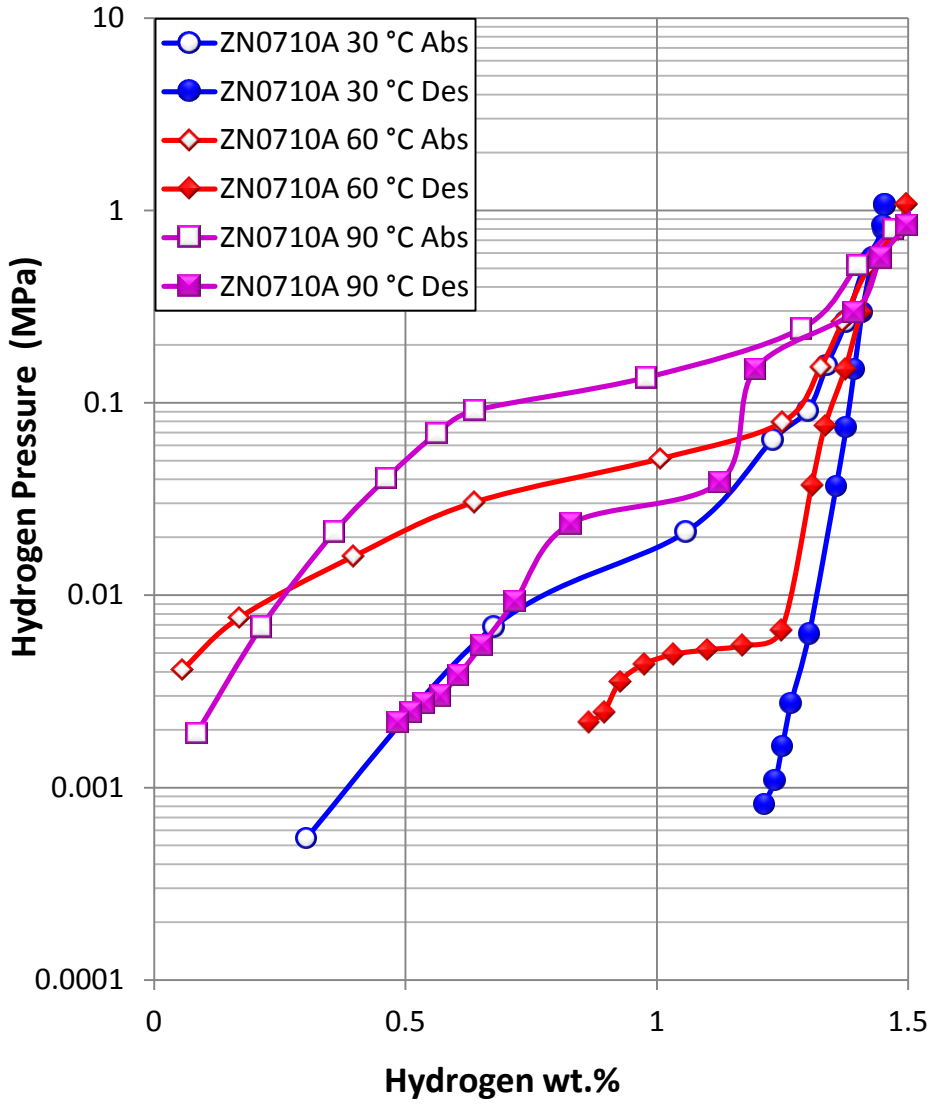

Figure 3.4d PCT isotherms of ZN0710A, and open and solid symbols are for absorption and desorption curves, respectively.

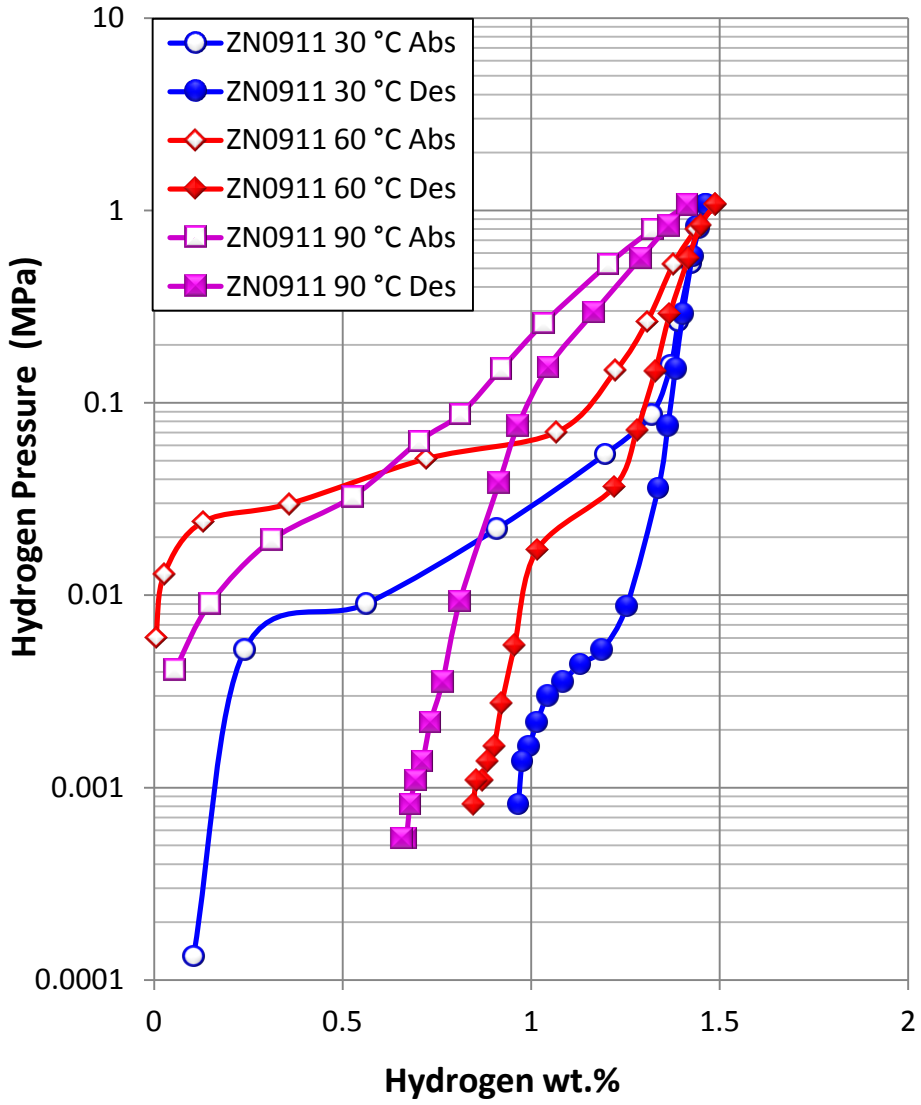

Figure 3.4e PCT isotherms of ZN0911, and open and solid symbols are for absorption and desorption curves, respectively.

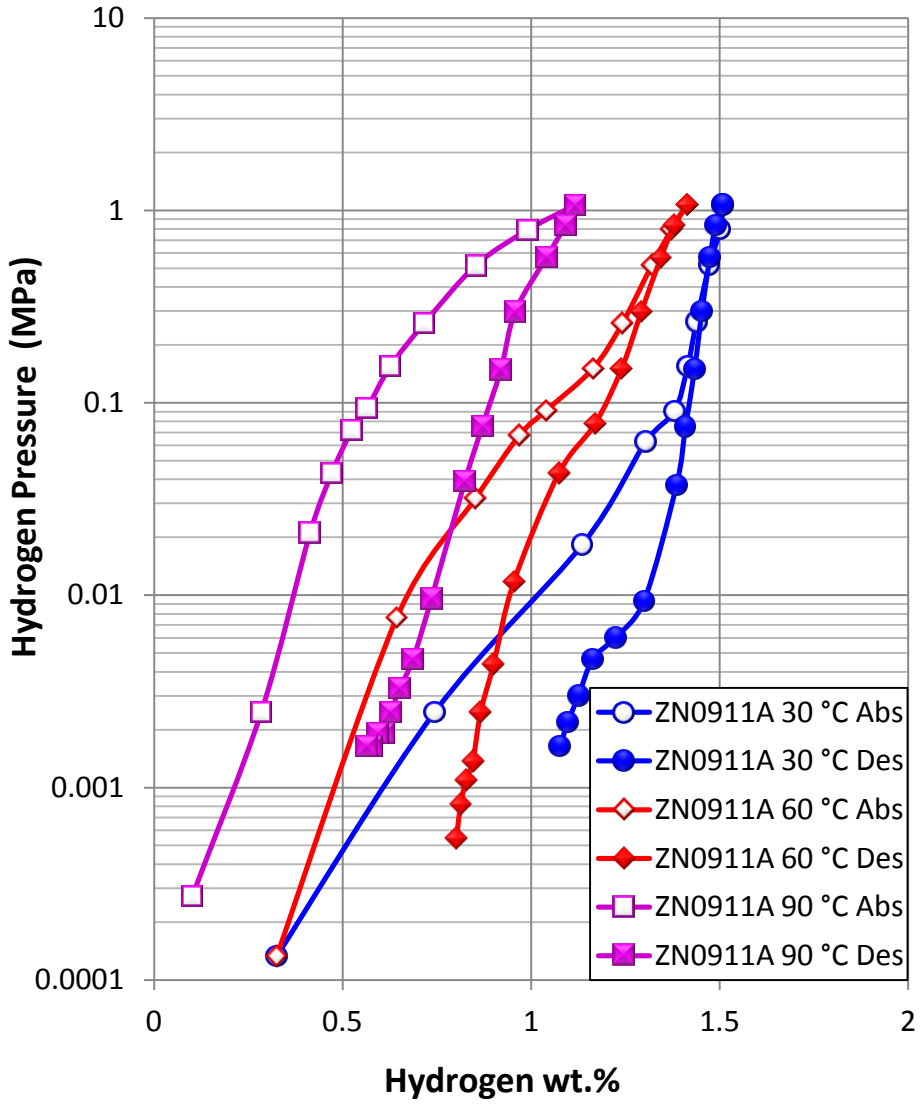

Figure 3.4f PCT isotherms of ZN0911A, and open and solid symbols are for absorption and desorption curves, respectively.

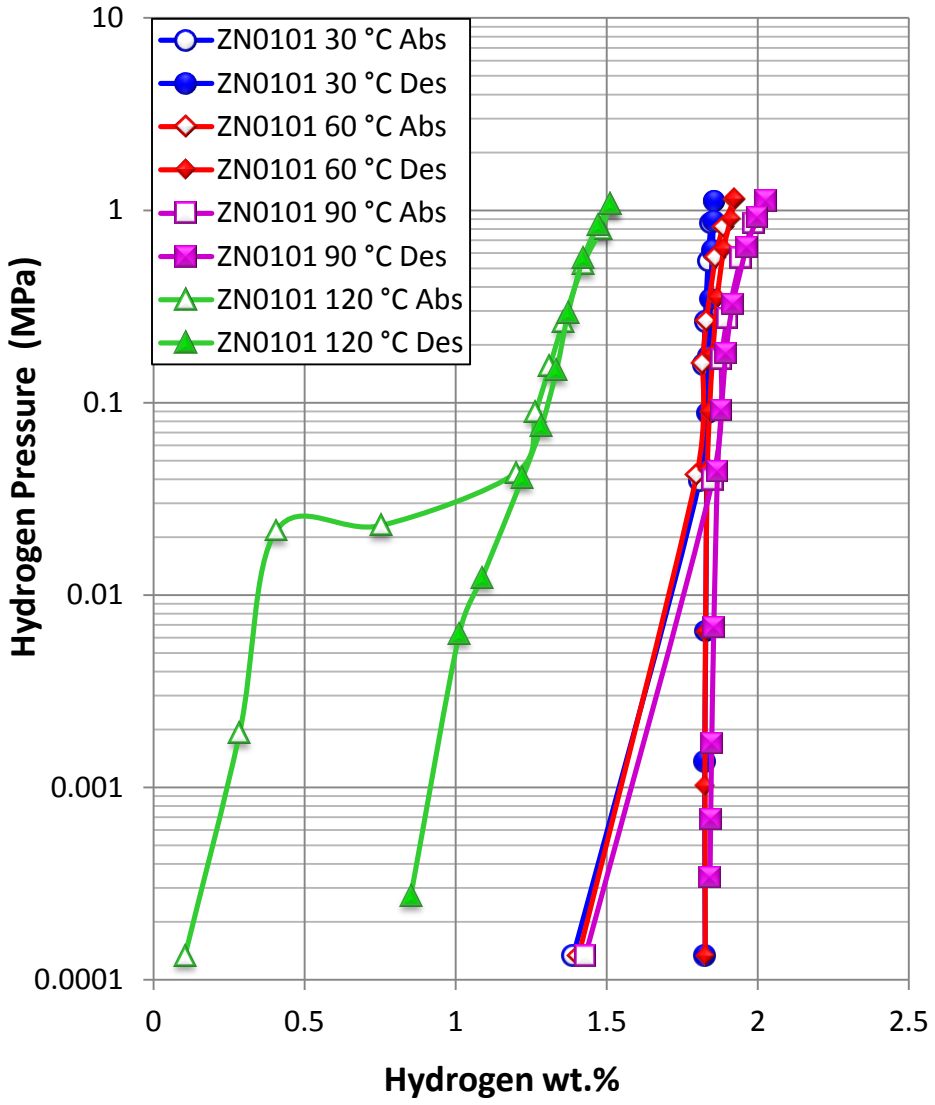

Figure 3.4g PCT isotherms of ZN0101, and open and solid symbols are for absorption and desorption curves, respectively.

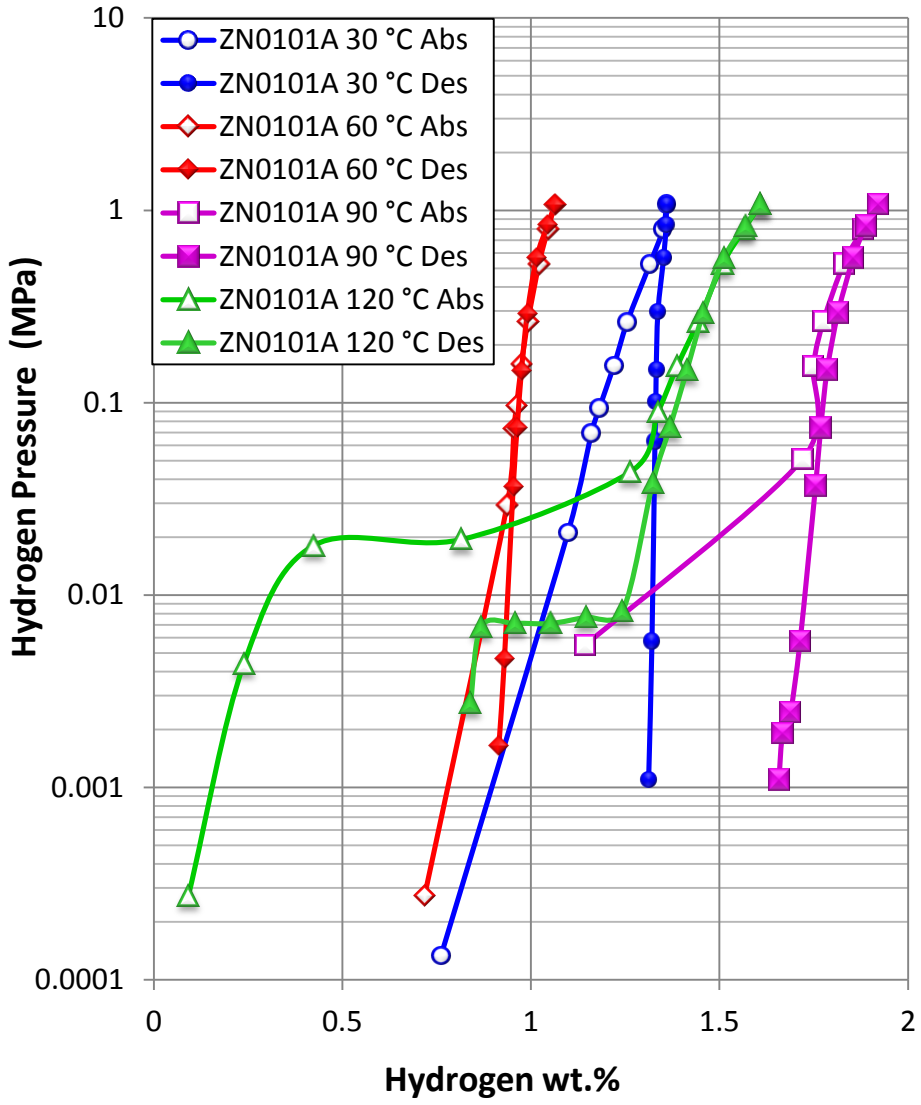

Figure 3.4h PCT isotherms of ZN0101A, and open and solid symbols are for absorption and desorption curves, respectively.

Table 3.4 Summary of PCT measurements

	Maximum storage capacity (wt.%)	**Reversible storage capacity (wt.%)**	**Absorption plateau pressure (MPa)**		**$-\Delta H$ (kJ mol^{-1} H_2)**	**$-\Delta S$ (J K^{-1} mol^{-1} H_2)**
Temperature	30 °C	30 °C	60 °C	90 °C	Abs	Abs
ZN0821	0.63	0.36	0.0320	0.1200	44	123
ZN0821A	0.50	0.37	0.0867	-	-	-
ZN0710	1.41	0.19	0.0240	0.1067	50	138
ZN0710A	1.45	0.24	0.0333	0.1333	46	130
ZN0911	1.46	0.50	-	-	-	-
ZN0911A	1.51	0.43	-	-	-	-
ZN0101	1.86	0.03	-	-	-	-
ZN0101A	1.36	0.05	-	0.0167	-	-

The maximum storage capacities measured at 30 °C of each alloy before and after annealing are plotted in Figure 3.5. From the alloy designing point, it is predicted that as the Zr/Ni ratio increases, the metal-hydrogen bond becomes stronger and the storage capacity increases. Among the annealed alloys, which consist of features that are more single-phase or "pure" (except for ZN0911A. However, the performances before and after annealing are comparable, and therefore using the result from ZN0911A for evaluation will not change the performance trend among alloys and at the same time keep the comparison consistent among annealed alloys) and were the focuses for most previous research efforts, the maximum storage capacity increases with the increasing trend of the Zr/Ni ratio but decreases at ZN0101A. More specifically, the maximum storage capacities of ZN0821A, ZN0710A, ZN0911A, and ZN0101A at 30 °C are 0.50, 1.45, 1.51, and 1.36 wt.%, respectively, which can be compared with Joubert et al.'s results of 0.50, 1.38, 1.25 and 1.70 wt.% @ 25 °C measured from alloys with the same compositions after annealing at 1000 °C for 30 days, respectively [12, 58]. While the maximum storage capacities of ZN0821A and ZN0710A are in agreement with the previous study, the results from ZN0911A and ZN0101A contradict. As stated earlier, the maximum storage capacity increases as the Zr/Ni ratio increases and then decreases at higher Zr/Ni ratio in both Joubert et al.'s and the current studies, however, the onset decreasing points are different (Zr : Ni = 9 : 11 by Joubert et al. vs. Zr : Ni = 1 : 1 in the current study). Another difference is in the maximum storage capacity of annealed ZrNi: Joubert et al. showed that after obtaining the lowest capacity from Zr_9Ni_{11}, ZrNi demonstrated the highest capacity among all alloys possibly due to its highest Zr/Ni ratio; in the current study, ZN0101A has one of the lowest capacities among all alloys (only higher than ZN0821A). On a different note, similar maximum storage capacity of ZrNi at 27 °C to the result in the current study was reported previously [60].

Although the Zr/Ni ratio shows significant impact on the maximum storage capacity, an adequate balance between Zr and Ni may be more important in obtaining the optimum result.

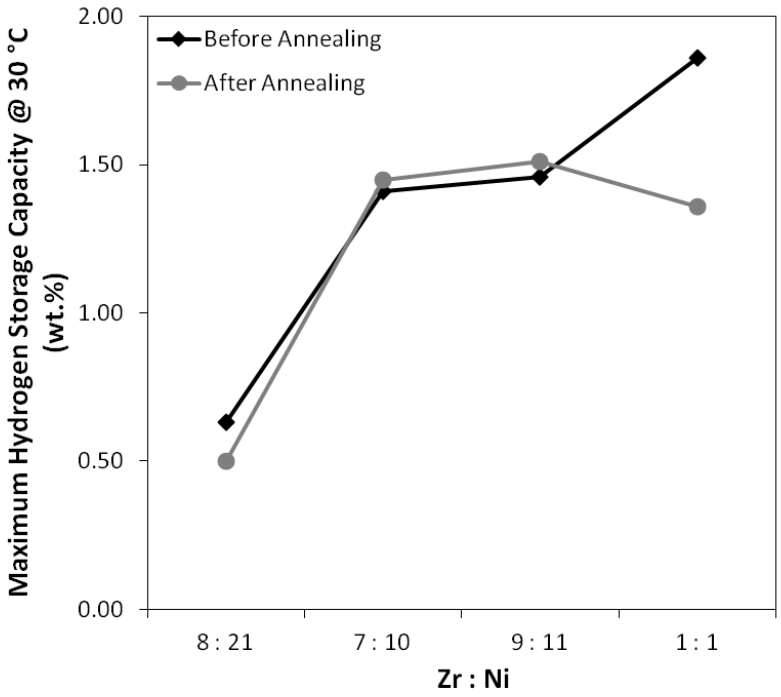

Figure 3.5 30 °C maximum gaseous phase hydrogen storage capacity in wt.% measured by PCT for all alloys in this study

With the knowledge of "pure" alloys (based on the comparison of the annealed alloys), the effect of annealing on the maximum storage capacity is evaluated. Annealing ZN0821 decreases the maximum storage capacity. The reduction of the secondary ZrNi phase and the increase of the major Zr_8Ni_{21} phase after annealing decreases the capacity in ZN0821A due to Zr_8Ni_{21}'s lower maximum storage capacity compared to ZrNi as seen in the after annealing curve in Figure 3.5. The effect of annealing on ZN0101 is especially significant. After annealing, the amounts of the major ZrNi phase and the secondary Zr_9Ni_{11} phase are increased and decreased, respectively, and since the maximum storage capacity of ZrNi is lower than that of Zr_9Ni_{11} as

discussed earlier and seen in the after annealing curve in Figure 3.5, the maximum storage capacity is reduced. The maximum storage capacities for ZN0710/ZN0710A and ZN0911/ZN0911A are comparable.

The reversible storage capacities measured at 30 °C of each alloy before and after annealing are plotted in Figure 3.6. Among the annealed alloys, the reversible storage capacity decreases with the increasing trend of Zr/Ni ratio with the exception of ZN0710A. Zr/Ni ratio, an important indicator of the behavior of storage capability, is clearly not the only factor that affects the overall reversible storage capacity. Hydrogen desorption rate is another issue that needs to be taken into consideration. It is suspected that although ZN0710A should demonstrate relatively higher reversible storage capacity than ZN0911A does according to their Zr/Ni ratios, the hydrogen desorption rate of ZN0911A may be so much higher than the rate of ZN0710A and overpowers the overall reversible storage performance at 30 °C. As temperature increases, the hydrogen desorption rates of ZN0710A and ZN0911A are both improved, and the Zr/Ni ratio becomes the more major player in determining the overall reversible storage performance. Figure 3.7 illustrates this surpassing trend of the reversible capacity in ZN0710A over that in ZN0911A as temperature rises.

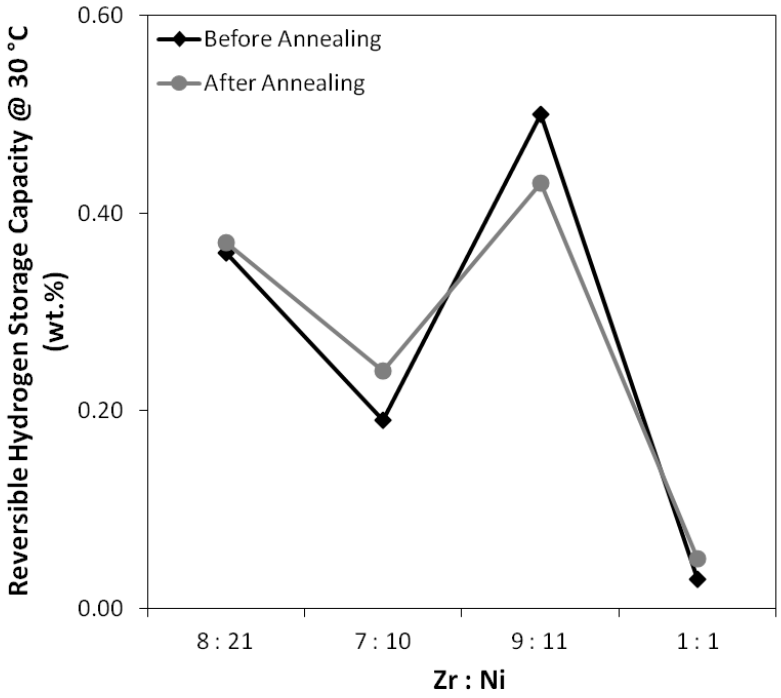

Figure 3.6 30 °C reversible hydrogen storage capacities in wt.% measured by PCT for all alloys in this study

Annealing influences the reversible storage capacities of Zr_8Ni_{21}, Zr_7Ni_{10}, Zr_9Ni_{11}, and ZrNi in different ways. After annealing ZN0710, the reversible capacity increases. As discussed previously, tetragonal-structured Zr_7Ni_{10} can be introduced into the alloy system after hydride/dehydride cycling [65-67], which is evidently the case based on the double plateaus of the PCT isotherm ZN0710A 90 °C Des in Figure 3.4d. However, such phenomenon is not observed in unannealed ZN0710. Moreover, from the same standpoint, the unit cell volume of orthorhombic-structured Zr_7Ni_{10} is larger than that of tetragonal-structured Zr_7Ni_{10} [66], which will be discussed further in CHAPTER 5. Therefore, the smaller unit cell of tetragonal-structured Zr_7Ni_{10} in ZN0710A assists in achieving better reversible storage capacity when compared to ZN0710. Comparing ZN0911 and ZN0911A, the reversible storage capacity decreases after annealing due to the increase in secondary ZrNi phase, which has non-reversible

hydrogen storage capability [74, 93]. The reversible storage capacities for ZN0821/ZN0821A and ZN0101/ZN0101A are comparable.

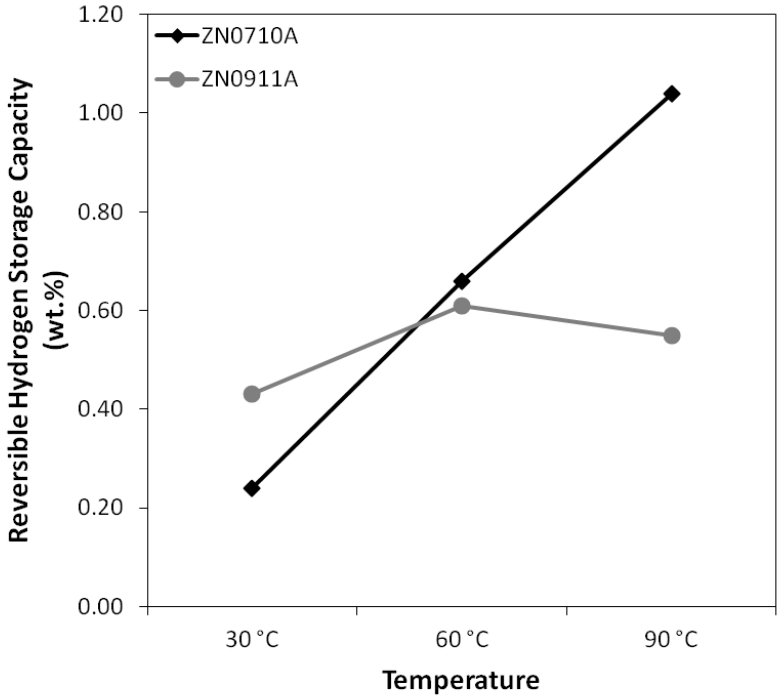

Figure 3.7 30, 60, and 90 °C reversible hydrogen storage capacities in wt.% measured by PCT for ZN0710 and ZN0911

Both ΔH and ΔS were calculated based on the 60 and 90 °C absorption isotherms by the equation

$$\Delta G = \Delta H - T\Delta S = RT \ln P \qquad (3.1)$$

where R is the ideal gas constant, and T is the absolute temperature. Among the annealed alloys, only ΔH (heat of hydride formation) and ΔS of ZN0710A can be obtained (–46 kJ mol^{-1} H_2 and –130 J K^{-1} mol^{-1} H_2, respectively), and the results are very similar to the previously reported

values of annealed Zr_7Ni_{10} (–50 to –47 kJ mol^{-1} H_2 and –144 to –132 J K^{-1} mol^{-1} H_2 [60, 61, 65, 69, 94], respectively).

3.2.3 Electrochemical measurement

Half-cell capacity measurements were conducted at discharge rates of 50 mA g^{-1} first and followed by two pulls at 12 and 4 mA g^{-1}. The full discharge capacities (sum of capacities measured at 50, 12, and 4 mA g^{-1} for each cycle, which is the same as if the capacity is measured at 4 mA g^{-1}) of the first 10 cycles of each sample is plotted in Figure 3.8, and the stabilized full discharge capacity for each sample is listed in Table 3.5. For easy comparison, the full discharge capacities of each alloy before and after annealing are plotted in Figure 3.9. Among the annealed alloys, the full discharge capacity increases, maximizes at ZN0710A, and then decreases as the Zr/Ni ratio increases. In other words, the full discharge capacity can be correlated to the Zr/Ni ratio parabolically with the maximum value at ZN0710A. Maximum gaseous phase hydrogen storage capacity can be converted and used as a guide to estimate the electrochemical discharge capacity [93, 95]. Furthermore, electrochemical discharging capability is also possibly connected to the hydrogen desorption/discharging rate. The theoretical trends of both maximum gaseous phase hydrogen storage capacity and hydrogen desorption/discharging rate according to the Zr/Ni ratio are presented in Figure 3.10, and when combining the effects of both, a parabolic relationship with a maximum appears as the Zr/Ni ratio increases. Therefore, the electrochemical discharge capacities of the annealed alloys are influenced heavily by both the storage and rate factors. The high-rate discharge capacities (capacities measured at 50 mA g^{-1}) of ZN0821A, ZN0710A, ZN0911A, and ZN0101A are 106, 63, 41, and 11 mAh g^{-1}, respectively. Compared to the results given by Ruiz et al. [56, 59], which are 91, 51, and 45 mAh g^{-1}

measured at 53 mA g^{-1} for Zr_8Ni_{21}, Zr_7Ni_{10}, and Zr_9Ni_{11} annealed at 1000 °C for 30 days, respectively, the results are comparable.

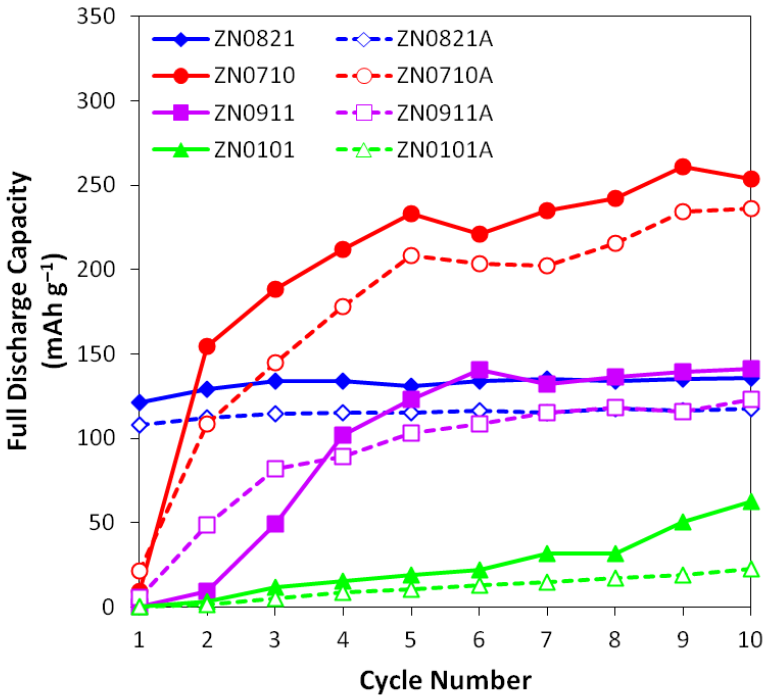

Figure 3.8 Half-cell capacities of alloys ZN0821, ZN0821A, ZN0710, ZN0710A, ZN0911, ZN0911A, ZN0101, and ZN0101A vs. cycle number.

Table 3.5 Summary of room temperature electrochemical half-cell measurements and results of 4-h hot alkaline etching experiments

	Full discharge capacity (mAh g^{-1})	**HRD (%)**	**Number of activation cycles**	**Zr (ppm)**	**M_s (memu g^{-1})**
ZN0821	136	73	1	102	90
ZN0821A	118	90	1	129	59
ZN0710	253	32	5	56	35.2
ZN0710A	235	27	5	81	20.2
ZN0911	141	23	5	39	15.6
ZN0911A	122	34	5	41	32.6
ZN0101	62	20	>10	38	18.9
ZN0101A	23	49	8	56	16.1

As shown in Figure 3.9, the full discharge capacity before annealing follows the same exact evolution trend of the full discharge capacity after annealing with the respect to the Zr/Ni ratio. Annealing decreases the full discharge capacity in each alloy composition due to the reduction in secondary phase and the consequent decrease in synergetic effect. In the case of annealing ZN0911, although the amount of the secondary phase is increased, the non-reversible nature of ZrNi introduced by annealing lowers the full discharge capacity.

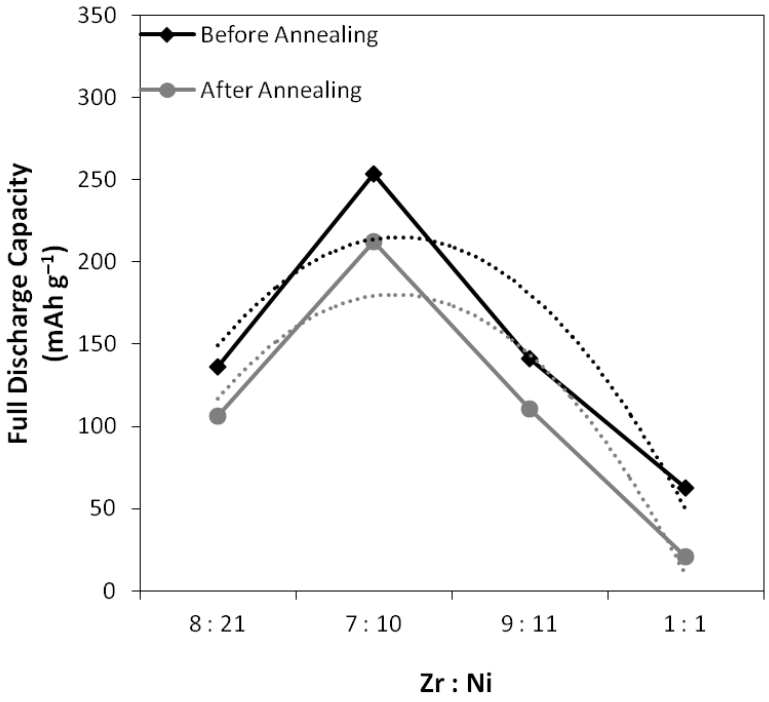

Figure 3.9 Full half-cell discharge capacities measured at a discharge current of 4 mA g^{-1} for all alloys in this study

HRD, defined as the ratio between the high-rate and full discharge capacities, for each sample is listed in Table 3.5. Among the annealed alloys, HRD decreases as the Zr/Ni ratio increases with the exception of ZN0101A. Due to the much lower discharge capacity of ZN0101A, the result of the HRD calculation is not as reliable. After annealing, HRD increases or stays comparable.

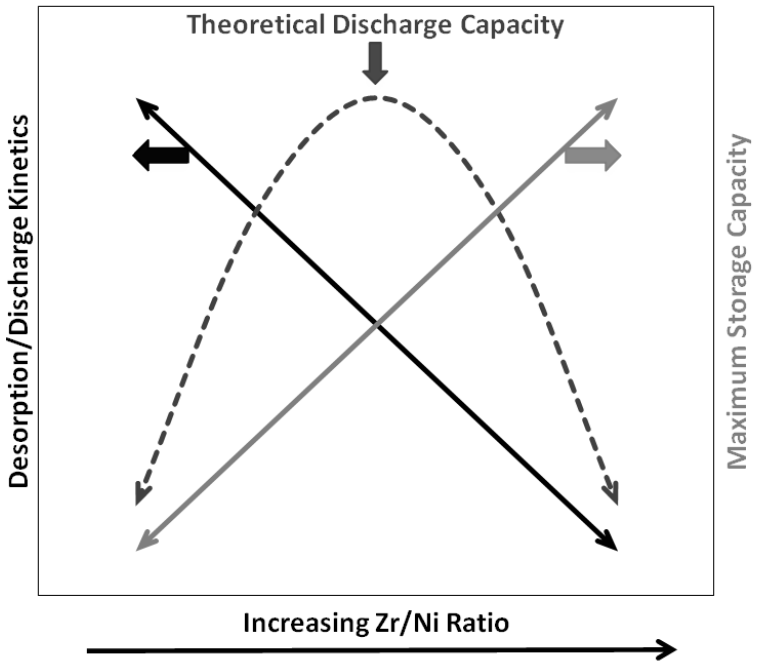

Figure 3.10 Theoretical desorption/discharge kinetics, maximum gaseous phase hydrogen storage capacity, and discharge capacity as functions of Zr/Ni ratio.

The number of activation cycles, defined as the cycle number when stabilized full discharge capacity is reached, for each sample is listed in Table 3.5. Among the annealed alloys, the number of activation cycles increases as the Zr/Ni ratio increases. Compared to Ruiz et al.'s results of 1, 55, and 60 activation cycles for Zr_8Ni_{21}, Zr_7Ni_{10}, and Zr_9Ni_{11} annealed at 1000 °C for 30 days, respectively [56, 59], the results obtained from the current study of 1, 5, and 5 activations cycles for ZN0821A, ZN0710A, and ZN0911A, respectively show similar trend, however, much easier activation. The use of teflonized carbon as binder in Ruiz et al.'s electrode preparation may be the reason of the more difficult activation. The numbers of activation cycles before and after annealing are comparable for each alloy composition.

3.2.4 Hot alkaline etching

Bathing in alkaline at an elevated temperature is a commonly-used technique for formatting AB_2 MH alloys [96-99]. 2- and 4-h hot alkaline experiments were performed on each sample. Zr in the form of $HZrO_3^-$ is expected to be detected in 30 wt.% KOH bath according to the Pourbaix diagram [100]; furthermore, it is predicted that as the Zr/Ni ratio increases, the concentration of Zr in the bath would increase. The results of the hot alkaline etching baths of 2 and 4 h examined by ICP analysis are listed in Table 3.5 and plotted in Figure 3.11. Contradictory to the prediction, as the Zr/Ni ratio increases, the concentration of Zr in solution decreases among the annealed alloys. According to the heats of formation (ΔH_f) data of Zr-Ni binary alloys [101], as the Zr/Ni ratio increases in the region of interest (Zr/Ni = 0.38 to 1.00), ΔH_f decreases, which corresponds to a more corrosion-resistant nature. Therefore, as the Zr/Ni ratio increases, the formation process becomes harder. After annealing, the concentration of Zr in solution increases for each alloy composition. Annealing treatment promotes the formation of surface oxide, and dissolution of the more abundant surface oxide causes the increase in concentration of Zr.

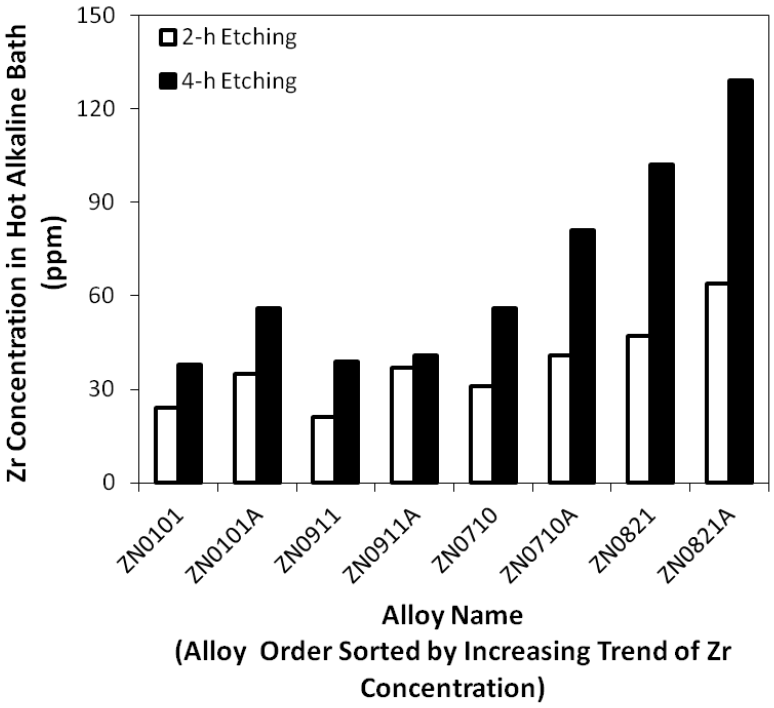

Figure 3.11 Evolution of concentration of Zr in solution after hot alkaline bath for all alloys in this study

3.2.5 Magnetization measurement

Metallic Ni clusters embedded in the surface oxide of the MH electrode were proven to be crucial catalysts in the surface reaction and influence HRD and low temperature performance of Ni/MH battery [1, 2, 102]. The magnetic susceptibility of the ferromagnetic metallic Ni clusters is several orders of magnitude larger than that of the paramagnetic Ni in the bulk alloy [103], therefore the amount of metallic Ni in the surface oxide can be quantified by the magnetization measurement. Room temperature magnetization curves ($M(H)$) were measured as a function of applied magnetic field (H), and one sample curve is shown in Figure 3.12. These magnetization curves can be fitted into the Langevin function [103]

$$M(H) - \chi_B H = M_S \left\{ \coth\left(\frac{\mu H}{kT} - \frac{kT}{\mu H}\right) \right\} \quad \textbf{(3.2)}$$

where χ_B is the intrinsic paramagnetic susceptibility of the alloy (estimated by the value of the high field magnetization), M_S is the saturation magnetization of the ferromagnetic metallic Ni, μ is the average magnetic moment of each metallic cluster, k is the Boltzmann constant, and T is the absolute temperature.

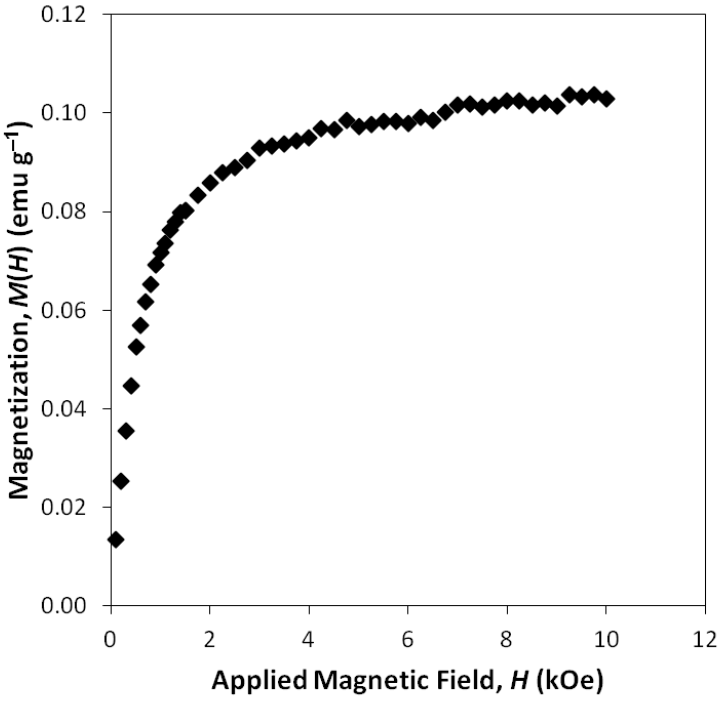

Figure 3.12 Sample graph of magnetization vs. applied magnetic field for obtaining saturated magnetic susceptibility

The obtained M_S is a measure of the total content of metallic Ni in the surface oxide, and the results are listed in Table 3.5 and plotted in Figure 3.13. Among the annealed alloys, as the Zr/Ni ratio increases, M_S decreases (the content of metallic Ni in the surface oxide decreases)

due to the increase in corrosion resistance. This trend corresponds to that observed in HRD and can be summarized as follows: as the Zr/Ni ratio in the alloy composition increases, the content of metallic Ni in the surface oxide decreases and consequently HRD decreases. It should be noted that M_S decreases in the first 2 h of etching experiment of most samples. This observation is a result of the fast dissolution of the native oxide formed during sample processing, where some metallic Ni is lost into the solution [104, 105]. At the 4-h mark, a new oxide layer is accumulated from prolong etching, and therefore M_S increases.

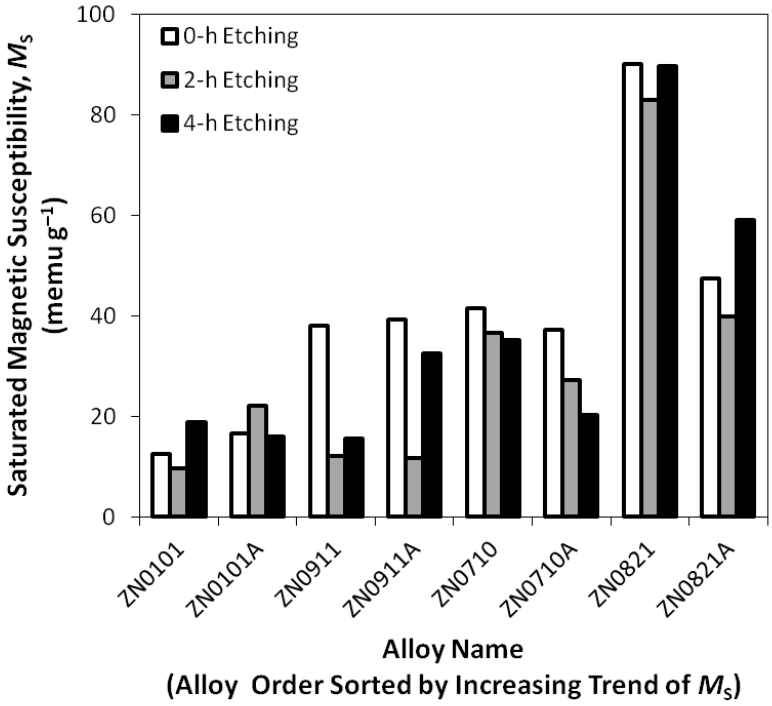

Figure 3.13 Evolution of saturated magnetic susceptibility in surface oxide after hot alkaline bath for all alloys in this study

3.3 Summary

A systematic study of four alloys with the average compositions targeting at Zr_8Ni_{21}, Zr_7Ni_{10}, Zr_9Ni_{11}, and ZrNi that correlated among composition, structure, gaseous phase hydrogen

storage, and electrochemical properties were presented. In addition, the synergetic effect between the major and secondary phases of the four alloy compositions was examined by comparing the results between as-cast and annealed counterparts. The results of this thorough investigation on Zr-Ni binary system can be summarized as follows:

- Annealing removed secondary phases except for the case of Zr_9Ni_{11}, where its secondary ZrNi phase increased;
    - With the help of annealing treatment, the structural stability trend was established to be Zr_7Ni_{10} > C15 ~ Zr_8Ni_{21} > ZrNi > Zr_9Ni_{11}.
- As the Zr/Ni ratio in the average composition increased, the maximum gaseous phase hydrogen storage capacity increased but maximized at Zr : Ni = 9 : 11;
- Natures of constituent phases influenced the gaseous phase storage;
- The combination of hydrogen desorption rate and theoretical reversible hydrogen storage affected the actual reversible gaseous phase storage;
- The combination of hydrogen desorption/discharge rate and theoretical maximum hydrogen storage affected the electrochemical discharge;
- As the Zr/Ni ratio in the average composition increased, HRD decreased;
- As the Zr/Ni ratio in the average composition decreased, the content of metallic Ni in the surface oxide increased, and HRD also increased.

Among all, the unannealed Zr_7Ni_{10} demonstrated the best overall gaseous phase hydrogen storage and electrochemical capacity and can be a candidate to replace AB_5 and AB_2 MH alloys in Ni/MH battery applications. Moreover, the unannealed Zr_8Ni_{21} showed a good balance between HRD and ease of formation. Since the compositional modifications on Zr_7Ni_{10} were studied extensively by Young et al. previously [69, 85, 90, 93], Zr_8Ni_{21} is selected for further

investigation in hopes to develop an alternative MH alloy for Ni/MH battery applications, which is presented in CHAPTER 4 and CHAPTER 5.

CHAPTER 4

EFFECTS OF ANNEALING ON $Zr_8Ni_{19}X_2$ (*X* = Ni, Mg, Al, Sc, V, Mn, Co, Sn, La, and Hf): STRUCTURAL CHARACTERISTICS

As discussed earlier, the stoichiometry of AB_2 was chosen for the transition-metal based MH alloys by considering the balance between large storage capacity (lower heat of hydride formation) and high rate discharge capability (higher heat of hydride formation) [3-5]. However, there is no AB_2 inter-metallic alloy for either Zr-Ni or Ti-Ni binary system. In Figure 1.8, the Zr-Ni binary phase diagram shows eight inter-metallic alloys: $ZrNi_5$, Zr_2Ni_7, $ZrNi_3$, Zr_8Ni_{21}, Zr_7Ni_{10}, Zr_9Ni_{11}, ZrNi, and Zr_2Ni, of which the closest inter-metallic compounds to AB_2 are Zr_7Ni_{10} and Zr_8Ni_{21}. Compared to AB_2 alloys, the former alloy, Zr_7Ni_{10}, has a slightly stronger metal-hydrogen bond strength due to its higher A to B ratio (0.70) and solidifies congruently from liquid. It should be noted that this version of the Zr-Ni binary phase diagram was recently proposed by Okamoto [57] and shows a very narrow solubility range of the Zr_7Ni_{10} phase. This differs from the conventional phase diagram that shows a broad composition range for the Zr_7Ni_{10} phase [106]. In a practical MH alloy, Zr was replaced partially by Ti to reduce the metal-hydrogen bond strength [69]. Other substituting elements have also been studied in order to improve the electrochemical properties [85, 90, 93]. The latter alloy, Zr_8Ni_{21}, was chosen as the focus of this chapter. Contrary to the property of Zr_7Ni_{10}, Zr_8Ni_{21} has a slightly weaker metal-hydrogen bond due to its higher concentration of B; therefore, adjusting B by partially replacing Ni with other elements is applied in this study to potentially increase the metal-hydrogen bond strength. Furthermore, Zr_8Ni_{21} does not solidify directly from the liquid as in the case of Zr_7Ni_{10}. Instead, Zr_2Ni_7 is first solidified from the liquid with a composition of Zr : Ni = 8 : 21 and later reacts with the remaining liquid to form Zr_8Ni_{21} alloy peritectically [82]. If the

condition of equilibrium is not reached during cooling, one or more secondary phases will precipitate out. Therefore, an annealing process was adopted for this study.

The crystal structure of Zr_8Ni_{21} is triclinic [82, 83], which is isotropic to that of Hf_8Ni_{21} [107]. The lattice parameters are a = 6.476 Å, b = 8.064 Å, c = 8.594 Å, α = 75.15°, β = 68.07°, and γ = 75.23° as determined by XRD analysis. The coordination number of Zr in this structure is 15 and that from other 11 non-equivalent Ni varies between 12 and 13. The XRD pattern reported by Ruiz et al. on a Zr_8Ni_{21} sample annealed at 1000 °C for 30 days includes an additional broad peak between 37.5° and 39.5° besides those identified as reflections from the Zr_8Ni_{21} structure when compared to Hf_8Ni_{21} [59]. This extra broad peak is believed to belong to a microcrystalline ZrNi phase according to the current study and will be discussed in later sections. Although the properties of un-modified Zr_8Ni_{21} were reported in the past, a systematic study of the effects from compositional modification and annealing on Zr_8Ni_{21} has not been performed in the past and will be presented in this chapter, focusing on the phase constituents before and after the annealing treatment.

4.1 Experimental setup

Samples were prepared by arc melting under a continuous argon flow with a non-consumable tungsten electrode and a water-cooled copper tray. Before each arc melt, a piece of sacrificial titanium underwent a few melting-cooling cycles to reduce the residual oxygen concentration in the system. Each 10-g sample ingot was re-melted and flipped over a few times to ensure uniformity in chemical composition. Half of each sample was annealed at 960 °C for 8 h in an argon environment. The chemical composition of each sample was examined with a Varian *Liberty* 100 ICP system. A Rigaku *Miniflex* XRD was used to study each alloy's

microstructure. A JEOL *JSM6320F* SEM with EDS capability was used to study the phase distribution and composition. Samples for SEM/EDS analysis were mounted and polished on epoxy blocks, rinsed and dried before entering the SEM chamber.

4.2 Results and discussion

10 alloys, Zr_8Ni_{21} (ZN-Ni), $Zr_8Ni_{19}Mg_2$ (ZN-Mg), $Zr_8Ni_{19}Al_2$ (ZN-Al), $Zr_8Ni_{19}Sc_2$ (ZN-Sc), $Zr_8Ni_{19}V_2$ (ZN-V), $Zr_8Ni_{19}Mn_2$ (ZN-Mn), $Zr_8Ni_{19}Co_2$ (ZN-Co), $Zr_8Ni_{19}Sn_2$ (ZN-Sn), $Zr_8Ni_{19}La_2$ (ZN-La), and $Zr_8Ni_{19}Hf_2$ (ZN-Hf), were prepared with raw materials from 99.999% purity metals except for ZN-Mg, where a $MgNi_2$ mother ingot was the source of Mg due to Mg's low boiling point. ICP analysis showed the compositions of these alloys to be very close to their designed values. The annealed samples were designated as samples ZN-*X*A, where *X* is the substituting element in the formula $Zr_8Ni_{19}X_2$. An annealing temperature of 960 °C was chosen to prevent liquid from forming during annealing. The sample ZN-MgA had very little Mg-content after the annealing process and therefore was removed from the experiment matrix of this study.

Al, Mn, and Co are frequently used to modify the electrochemical properties of AB_5, A_2B_7, and AB_2 MH alloys [108-117]. Sn has been added to AB_2 MH alloys for performance studies due to the potential to reduce raw material cost [118]. V is commonly used as a modifier in AB_2 MH alloys [21, 119]. Mg, Sc, La, and Hf were chosen with the intention to enlarge the unit cell and increase the hydrogen storage capacity. A few important properties of the modifying elements, such as atomic number, electronegativity, metallic radius, number of outer-shell electrons, and oxidation potential are listed in Table 4.1. The phase transformations during cooling for target compositions of Zr_8X_{21} and X_2Ni_{19}, where *X* is the one of the ten substituting

elements, are summarized in Table 4.2. The solidification processes of Zr_8X_{21} are very different, from immiscible (Mg, La) to eutectic (Al, Mn, Sn), eutectoid (V), peritectic (Ni), to solid solution (Sc, Co, Hf). The XRD patterns of the 19 samples (10 before annealing and 9 after annealing) are displayed in Figure 4.1. All peaks, except for the one near 38.4°, are identified and indexed according to the Powder Diffraction File database [120]. With the help of Jade 9 software, the lattice constants and unit cell volumes of major phases in each sample were calculated based on its XRD pattern and are listed in Table 4.3 together with the reference data. Notably, the lattice constants of some phases could not be calculated due to insufficient number of peaks and are therefore not shown in Table 4.3. The microstructures of the 19 samples were studied using SEM, with which both the SEI and the BEI were taken. The BEI micrographs are presented in Figure 4.2a-s with the same magnification. With the help of surface morphology analysis (done by examining the SEI micrographs), the compositions in several areas (identified numerically in the micrographs) were studied using EDS and the results are listed in Table 4.4. Combining the XRD and SEM/EDS results, the phase analyses of all samples, before and after annealing, are presented in the following sections.

Table 4.1 Basic properties of all elements used in this study. Electronegativity of an element represents the affinity to additional electron. Metallic radius is from 12-coordinated metal. Oxidation potential is measured between the metal and the lowest oxidation state.

	Zr	Ni	Mg	Al	Sc	V	Mn	Co	Sn	La	Hf
Atomic number	40	28	12	13	21	23	25	27	50	57	72
Electronegativity [77]	1.33	1.91	1.31	1.61	1.36	1.63	1.55	1.88	1.96	1.10	1.30
Metallic radius (Å) [121]	1.60	1.25	1.60	1.43	1.64	1.35	1.26	1.25	1.55	1.88	1.58
Number of outer-shell electrons	4	10	2	3	3	5	7	9	14	3	4
Oxidation potential (Volt vs. SHE) [122]	–1.45	–0.257	–2.70	–1.662	–2.077	–1.175	–1.185	–0.28	–0.138	–2.379	–1.55

Table 4.2 Phase transformations during cooling for target compositions of Zr_8X_{21} and X_2Ni_{19} [106]

	Zr_8X_{21} (Zr = 27.6 at.%)	X_2Ni_{19} (X = 9.5 at.%)
X = Ni	Peritectic @ 1180 °C	Congruent
X = Mg	Immiscible	Eutectic @ 1097 °C ($MgNi_2$ + Ni)
X = Al	Eutectic @ 1490°C ($ZrAl_2$ + $ZrAl_3$)	Eutectic @ 1385 °C ($AlNi_3$ + Ni)
X = Sc	Solid solution	Eutectic @ 1140 °C ($ScNi_5$ + Ni)
X = V	Eutectoid @ 1300°C (V + C15-ZrV_2)	Congruent @ 405 °C
X = Mn	Eutectic @ 1160°C (Mn + C14-$ZrMn_2$)	Solid solution
X = Co	Solid solution	Solid solution
X = Sn	Eutectic @ 232 °C (Sn + C54-$ZnSn_2$)	Eutectoid @ 920.5 °C ($SnNi_3$ + Ni)
X = La	Immiscible	Eutectic @ 1270 °C ($LaNi_5$ + Ni)
X = Hf	Solid solution	Eutectic @ 1190 °C ($HfNi_5$ + Ni)

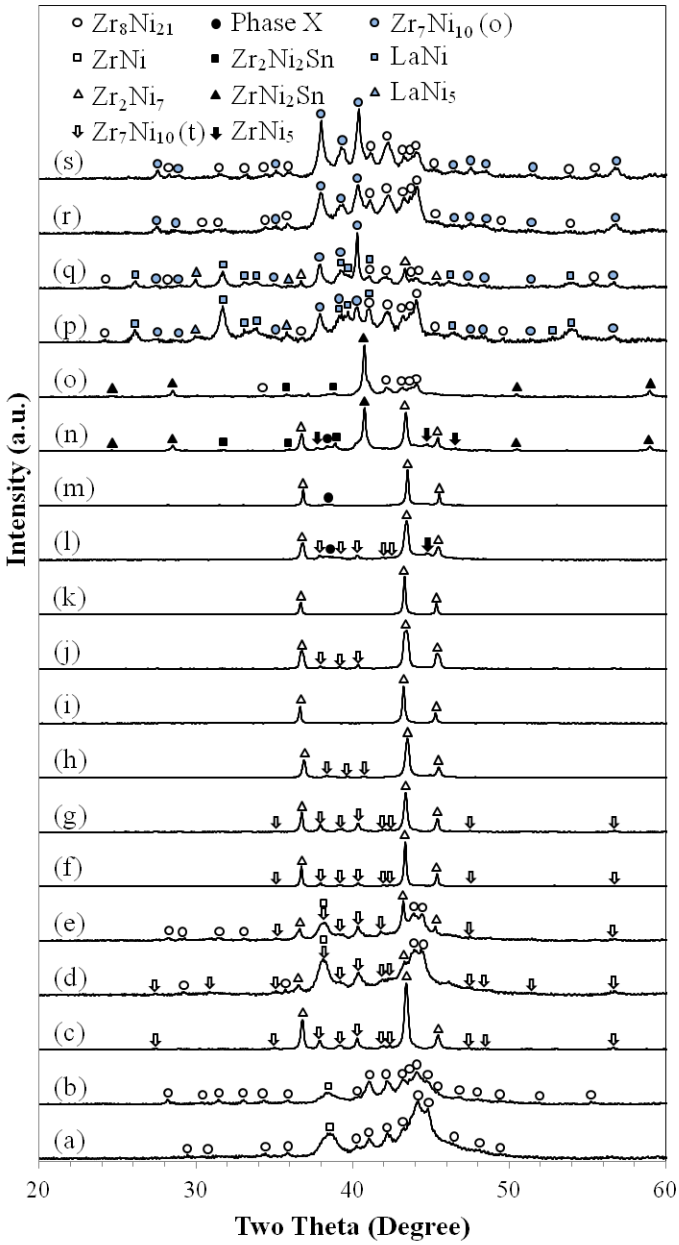

Figure 4.1 XRD patterns using Cu-K_α as the radiation source for alloys ZN-Ni (a), ZN-NiA (b), ZN-Mg (c), ZN-Al (d), ZN-AlA (e), ZN-Sc (f), ZN-ScA (g), ZN-V (h), ZN-VA (i), ZN-Mn (j), ZN-MnA (k), ZN-Co (l), ZN-CoA (m), ZN-Sn (n), ZN-SnA (o), ZN-La (p), ZN-LaA (q), ZN-Hf (r), and ZN-HfA (s).

Table 4.3 Lattice constants of major phases in each sample and their corresponding reference data [120]. *a*, *b*, and *c* are in Å, α, β, and γ are in degrees, and volumes are in $Å^3$.

	Phase	**Structure**	**PDF file #**	**Reference data**	**Reference volume**	**Measured data**	**Measured volume**
ZN-Ni	Zr_8Ni_{21}	Triclinic	04-002-9932	(*a*, *b*, *c*) = (6.4721, 8.0645, 8.5878) (α, β, γ) = (75.19, 68.04, 75.26)	395.54	(6.479, 8.045, 8.522) (75.30, 67.87, 75.15)	391.55
ZN-NiA	Zr_8Ni_{21}	Triclinic	04-002-9932	(*a*, *b*, *c*) = (6.4721, 8.0645, 8.5878) (α, β, γ) = (75.19, 68.04, 75.26)	395.54	(6.497, 8.021, 8.515) (75.34, 67.88, 75.33)	391.47
ZN-Mg	Zr_7Ni_{10}	Tetragonal	00-056-1231	(*a*, *b*, *c*) = (6.4956, 6.4956, 12.3610)	521.55	(6.487, 6.487, 12.338)	519.20
	Zr_2Ni_7	Cubic	00-037-0925	(*a*, *b*, *c*) = (6.68, 6.68, 6.68)	298.08	(6.90, 6.90, 6.90)	328.51
ZN-Al	Zr_7Ni_{10}	Tetragonal	00-056-1231	(*a*, *b*, *c*) = (6.4956, 6.4956, 12.3610)	521.55	(6.488, 6.488, 12.271)	516.54
	Zr_2Ni_7	Cubic	00-037-0925	(*a*, *b*, *c*) = (6.68, 6.68, 6.68)	298.08	(6.93, 6.93, 6.93)	332.81
ZN-AlA	Zr_7Ni_{10}	Tetragonal	00-056-1231	(*a*, *b*, *c*) = (6.4956, 6.4956, 12.3610)	521.55	(6.495, 6.495, 12.254)	516.94
	Zr_2Ni_7	Cubic	00-037-0925	(*a*, *b*, *c*) = (6.68, 6.68, 6.68)	298.08	(6.93, 6.93, 6.93)	332.81
ZN-Sc	Zr_7Ni_{10}	Tetragonal	00-056-1231	(*a*, *b*, *c*) = (6.4956, 6.4956, 12.3610)	521.55	(6.483, 6.483, 12.313)	517.51
	Zr_2Ni_7	Cubic	00-037-0925	(*a*, *b*, *c*) = (6.68, 6.68, 6.68)	298.08	(6.91, 6.91, 6.91)	329.94
ZN-ScA	Zr_7Ni_{10}	Tetragonal	00-056-1231	(*a*, *b*, *c*) = (6.4956, 6.4956, 12.3610)	521.55	(6.483, 6.483, 12.313)	517.51
	Zr_2Ni_7	Cubic	00-037-0925	(*a*, *b*, *c*) = (6.68, 6.68, 6.68)	298.08	(6.91, 6.91, 6.91)	329.94
ZN-V	Zr_7Ni_{10}	Tetragonal	00-056-1231	(*a*, *b*, *c*) = (6.4956, 6.4956, 12.3610)	521.55	(6.421, 6.421, 12.190)	502.58
	Zr_2Ni_7	Cubic	00-037-0925	(*a*, *b*, *c*) = (6.68, 6.68, 6.68)	298.08	(6.89, 6.89, 6.89)	327.08

ZN-VA	Zr_2Ni_7	Cubic	00-037-0925	(*a*, *b*, *c*) = (6.68, 6.68, 6.68)	298.08	(6.90, 6.90, 6.90)	328.51
ZN-Mn	Zr_7Ni_{10}	Tetragonal	00-056-1231	(*a*, *b*, *c*) = (6.4956, 6.4956, 12.3610)	521.55	(6.498, 6.498, 12.302)	519.44
	Zr_2Ni_7	Cubic	00-037-0925	(*a*, *b*, *c*) = (6.68, 6.68, 6.68)	298.08	(6.91, 6.91, 6.91)	329.94
ZN-MnA	Zr_2Ni_7	Cubic	00-037-0925	(*a*, *b*, *c*) = (6.68, 6.68, 6.68)	298.08	(6.92, 6.92, 6.92)	331.37
ZN-Co	Zr_7Ni_{10}	Tetragonal	00-056-1231	(*a*, *b*, *c*) = (6.4956, 6.4956, 12.3610)	521.55	(6.491, 6.491, 12.320)	519.08
	Zr_2Ni_7	Cubic	00-037-0925	(*a*, *b*, *c*) = (6.68, 6.68, 6.68)	298.08	(6.90, 6.90, 6.90)	328.51
	$ZrNi_5$	Cubic	00-037-0924	(*a*, *b*, *c*) = (6.68, 6.68, 6.68)	298.08	(6.71, 6.71, 6.71)	302.11
ZN-CoA	Zr_2Ni_7	Cubic	00-037-0925	(*a*, *b*, *c*) = (6.68, 6.68, 6.68)	298.08	(6.89, 6.89, 6.89)	327.08
ZN-Sn	Zr_2Ni_7	Cubic	00-037-0925	(*a*, *b*, *c*) = (6.68, 6.68, 6.68)	298.08	(6.91, 6.91, 6.91)	329.94
	$ZrNi_5$	Cubic	00-037-0924	(*a*, *b*, *c*) = (6.68, 6.68, 6.68)	298.08	(6.61, 6.61, 6.61)	288.80
	Zr_2SnNi_2	Tetragonal	00-048-1703	(*a*, *b*, *c*) = (7.0659, 7.0659, 3.4145)	170.48	(7.054, 7.054, 3.406)	169.48
	$ZrSnNi_2$	Cubic	00-023-1282	(*a*, *b*, *c*) = (6.27, 6.27, 6.27)	246.49	(6.25, 6.25, 6.25)	244.14
ZN-SnA	Zr_2SnNi_2	Tetragonal	00-048-1703	(*a*, *b*, *c*) = (7.0659, 7.0659, 3.4145)	170.48	(7.085, 7.084, 3.390)	170.12
	$ZrSnNi_2$	Cubic	00-023-1282	(*a*, *b*, *c*) = (6.27, 6.27, 6.27)	246.49	(6.28, 6.28, 6.28)	248.01
ZN-La	Zr_7Ni_{10}	Orthorhombic	00-047-1027	(*a*, *b*, *c*) = (12.385, 9.154, 9.216)	1044.84	(12.436, 9.166, 9.162)	1044.36
	Zr_8Ni_{21}	Triclinic	004-002-9932	(*a*, *b*, *c*) = (6.4721, 8.0645, 8.5878) (*α*, *β*, *γ*) = (75.19, 68.04, 75.26)	395.54	(6.430, 8.033, 8.645) (75.33, 68.03, 75.39)	394.39
	LaNi	Orthorhombic	00-019-0654	(*a*, *b*, *c*) = (3.907, 10.810, 4.396)	185.66	(3.910, 10.810, 4.385)	185.34
	$LaNi_5$	Hexagonal	00-055-0277	(*a*, *b*, *c*) = (5.0167, 5.0167, 3.9783)	260.13	(5.019, 5.019, 4.054)	265.32
ZN-LaA	Zr_7Ni_{10}	Orthorhombic	00-047-1027	(*a*, *b*, *c*) = (12.385, 9.154, 9.216)	1044.84	(12.301, 9.199, 9.175)	1038.21

	Zr_2Ni_7	Cubic	00-037-0925	(a, b, c) = (6.68, 6.68, 6.68)	298.08	(6.92, 6.92, 6.92)	331.37
	LaNi	Orthorhombic	00-019-0654	(a, b, c) = (3.907, 10.810, 4.396)	185.66	(3.904, 10.797, 4.389)	185.00
	$LaNi_5$	Hexagonal	00-055-0277	(a, b, c) = (5.0167, 5.0167, 3.9783)	260.13	(5.065, 5.065, 4.005)	270.27
ZN-Hf	Zr_7Ni_{10}	Orthorhombic	00-047-1027	(a, b, c) = (12.385, 9.154, 9.216)	1044.84	(12.384, 9.190, 9.130)	1039.08
	Zr_8Ni_{21}	Triclinic	04-002-9932	(a, b, c) = (6.4721, 8.0645, 8.5878) (α, β, γ) = (75.19, 68.04, 75.26)	395.54	(6.451, 8.047, 8.531) (75.12, 67.94, 75.15)	390.30
ZN-HfA	Zr_7Ni_{10}	Orthorhombic	00-047-1027	(a, b, c) = (12.385, 9.154, 9.216)	1044.84	(12.317, 9.151, 9.141)	1030.31
	Zr_8Ni_{21}	Triclinic	04-002-9932	(a, b, c) = (6.4721, 8.0645, 8.5878) (α, β, γ) = (75.19, 68.04, 75.26)	395.54	(6.493, 8.004, 8.504) (75.67, 67.75, 75.54)	390.28

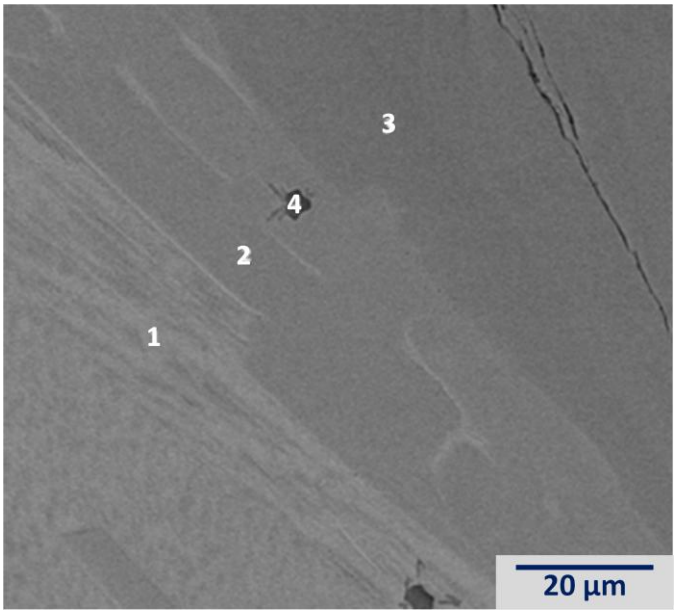

Figure 4.2a SEM BEI for ZN-Ni, and the chemical compositions of the indexed areas measured by EDS are summarized in Table 4.4.

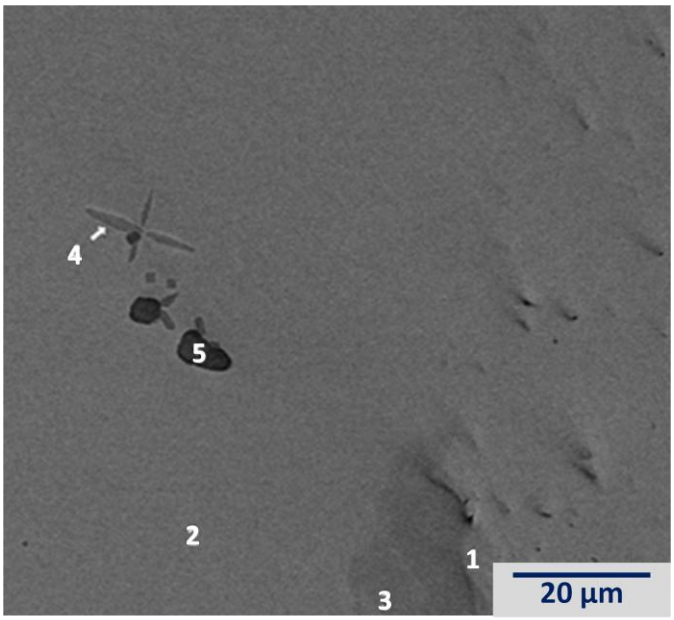

Figure 4.2b SEM BEI for ZN-NiA, and the chemical compositions of the indexed areas measured by EDS are summarized in Table 4.4.

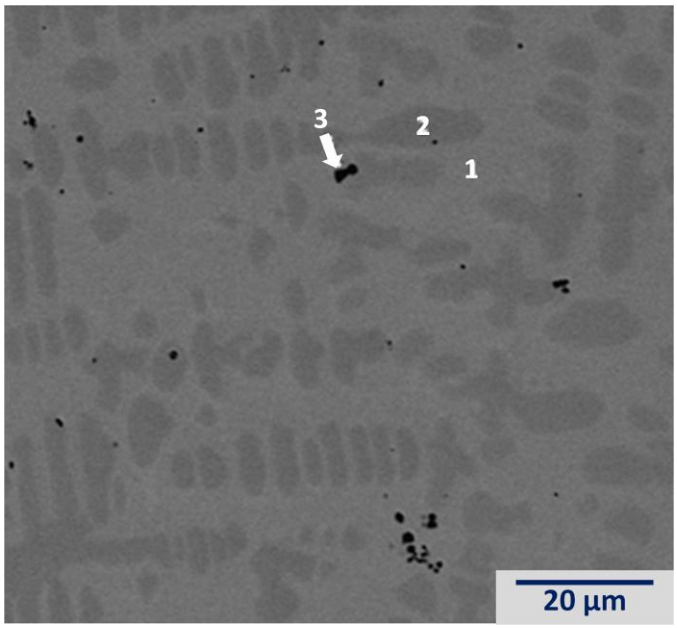

Figure 4.2c SEM BEI for ZN-Mg, and the chemical compositions of the indexed areas measured by EDS are summarized in Table 4.4.

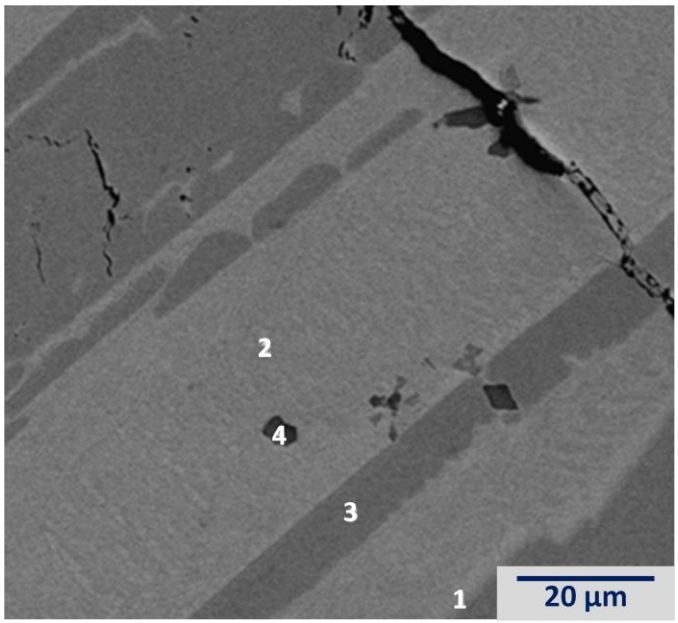

Figure 4.2d SEM BEI for ZN-Al, and the chemical compositions of the indexed areas measured by EDS are summarized in Table 4.4.

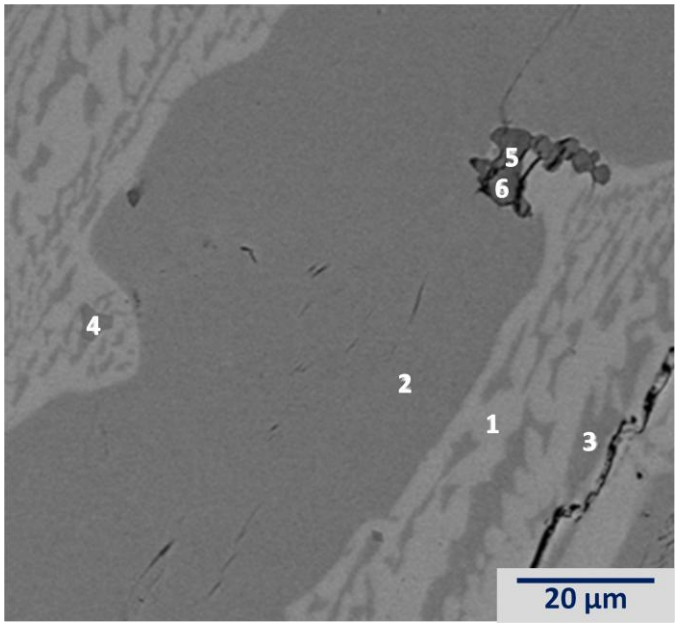

Figure 4.2e SEM BEI for ZN-AlA, and the chemical compositions of the indexed areas measured by EDS are summarized in Table 4.4.

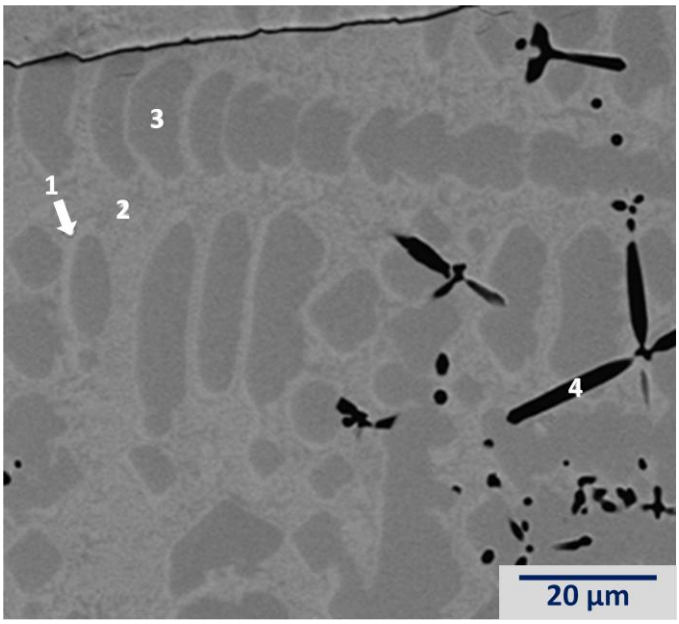

Figure 4.2f SEM BEI for ZN-Sc, and the chemical compositions of the indexed areas measured by EDS are summarized in Table 4.4.

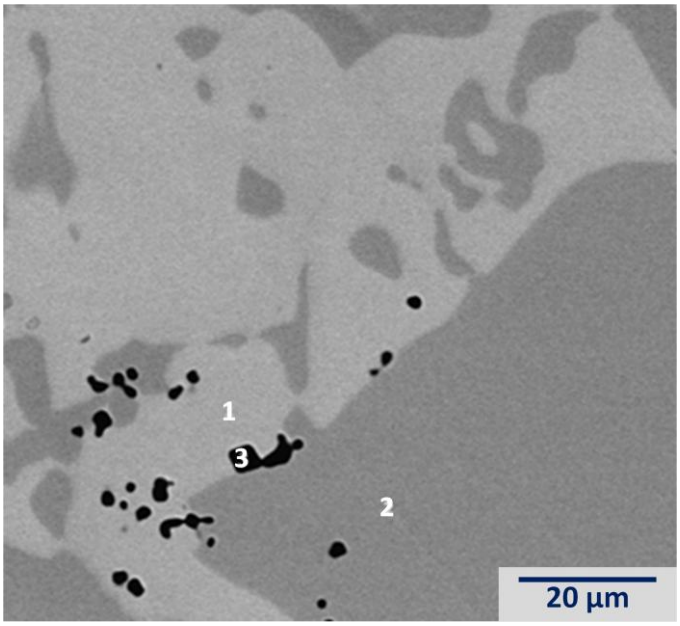

Figure 4.2g SEM BEI for ZN-ScA, and the chemical compositions of the indexed areas measured by EDS are summarized in Table 4.4.

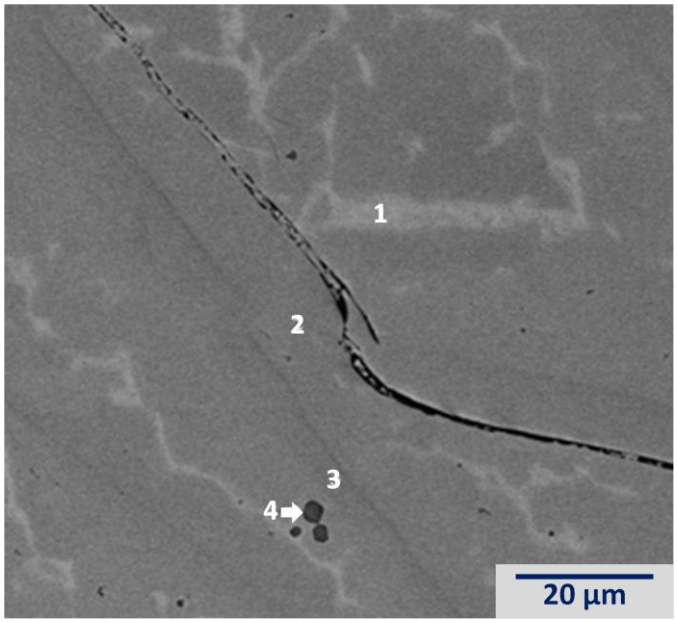

Figure 4.2h SEM BEI for ZN-V, and the chemical compositions of the indexed areas measured by EDS are summarized in Table 4.4.

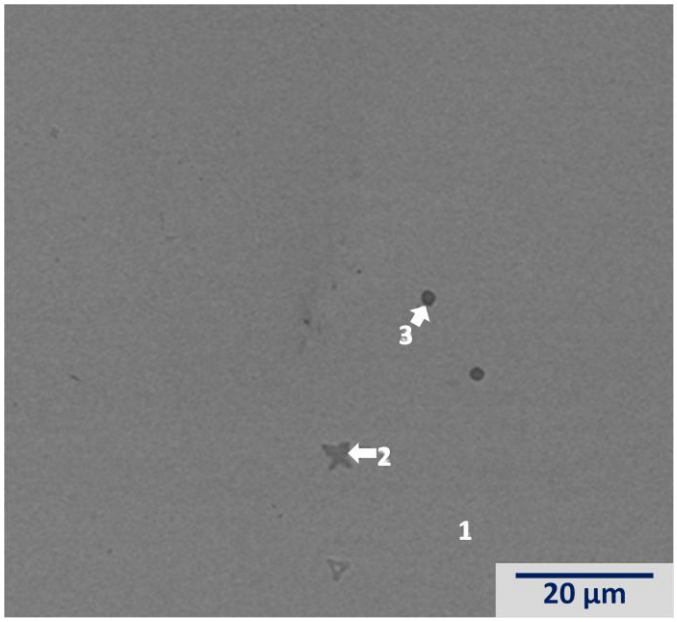

Figure 4.2i SEM BEI for ZN-VA, and the chemical compositions of the indexed areas measured by EDS are summarized in Table 4.4.

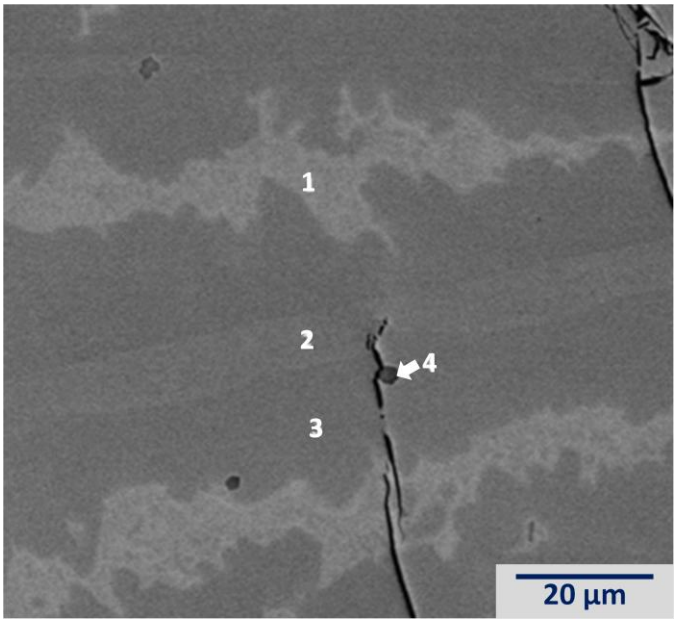

Figure 4.2j SEM BEI for ZN-Mn, and the chemical compositions of the indexed areas measured by EDS are summarized in Table 4.4.

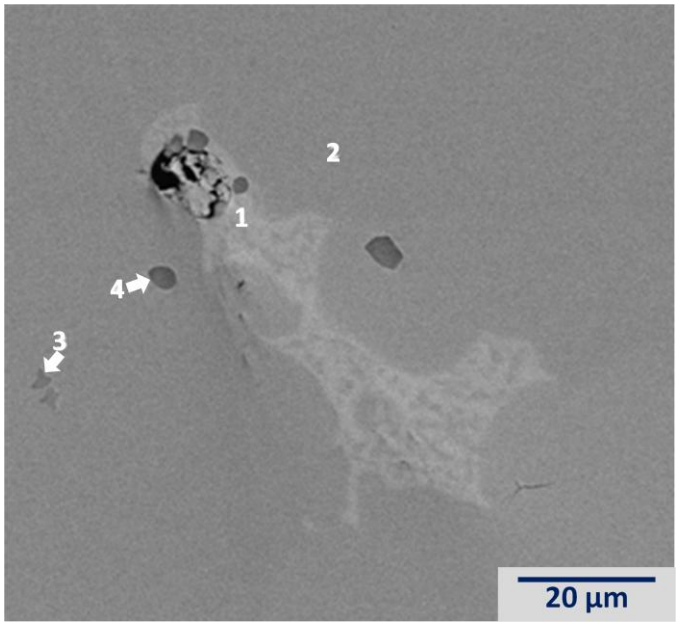

Figure 4.2k SEM BEI for ZN-MnA, and the chemical compositions of the indexed areas measured by EDS are summarized in Table 4.4.

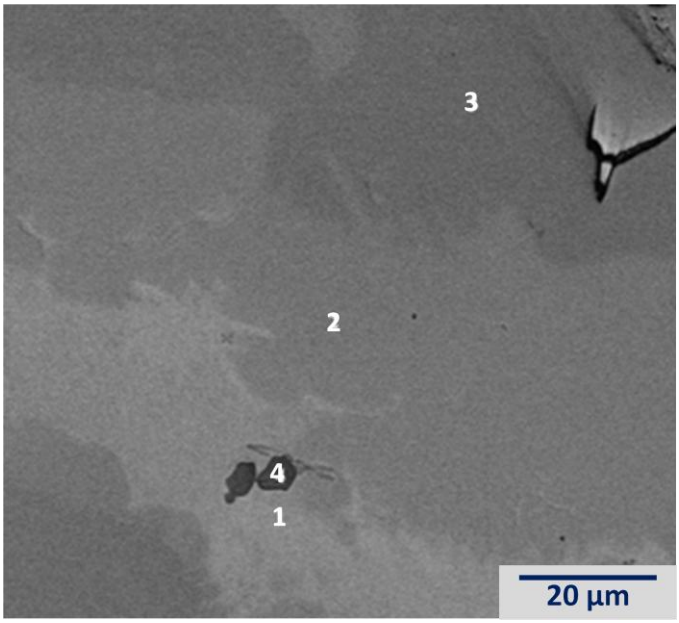

Figure 4.2l SEM BEI for ZN-Co, and the chemical compositions of the indexed areas measured by EDS are summarized in Table 4.4.

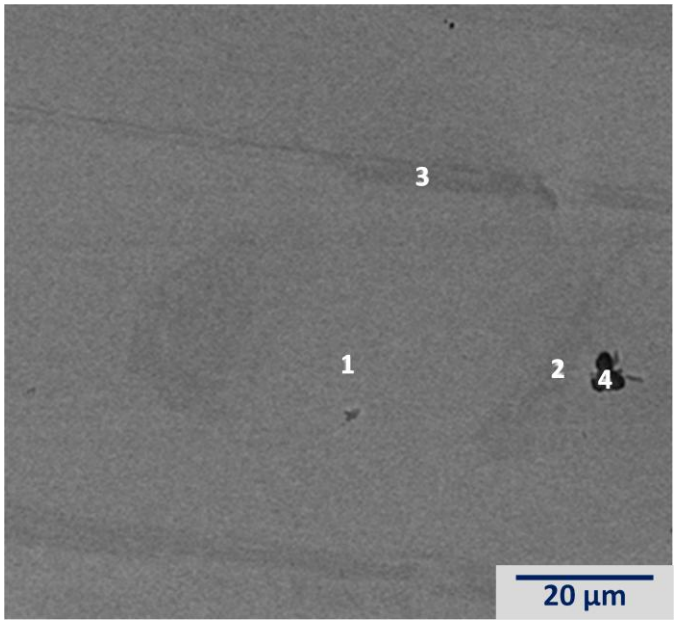

Figure 4.2m SEM BEI for ZN-CoA, and the chemical compositions of the indexed areas measured by EDS are summarized in Table 4.4.

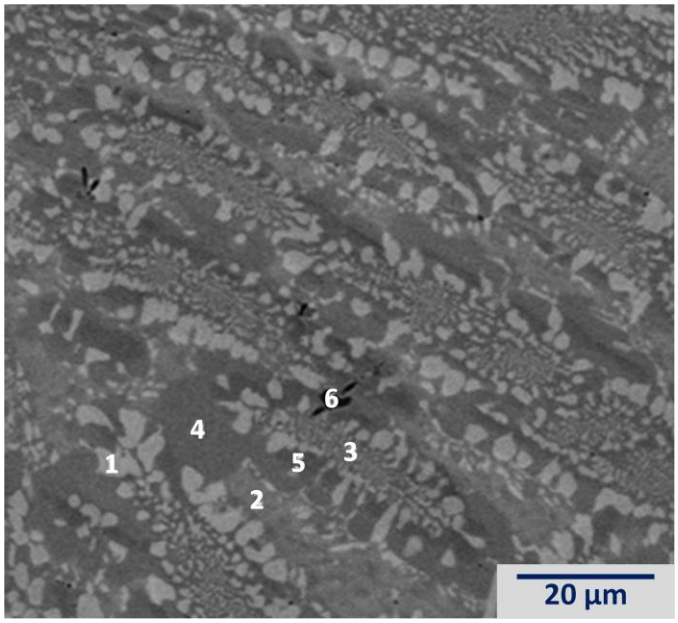

Figure 4.2n SEM BEI for ZN-Sn, and the chemical compositions of the indexed areas measured by EDS are summarized in Table 4.4.

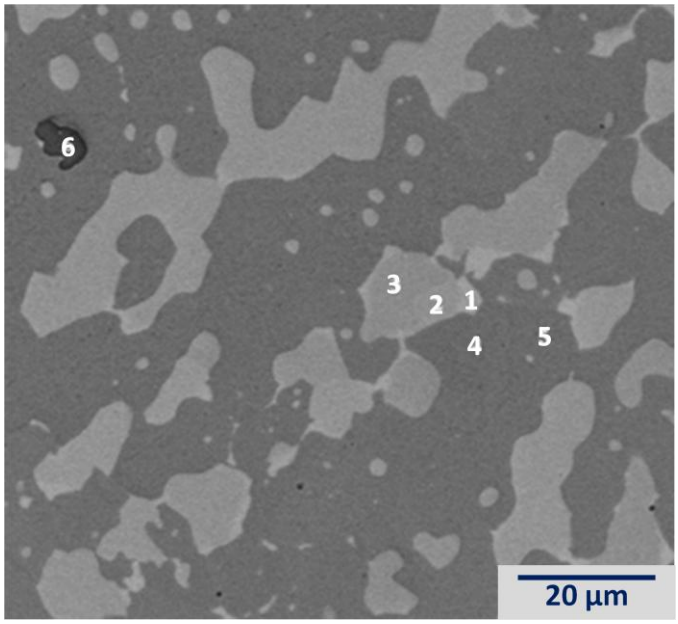

Figure 4.2o SEM BEI for ZN-SnA, and the chemical compositions of the indexed areas measured by EDS are summarized in Table 4.4.

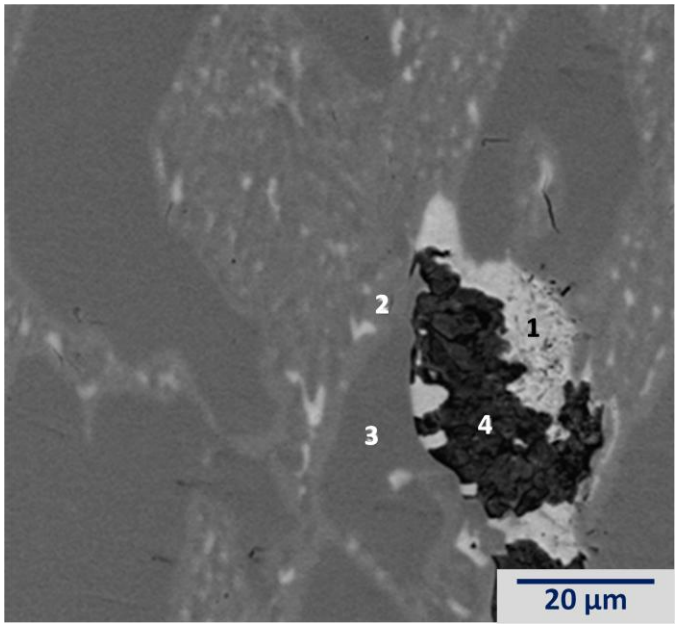

Figure 4.2p SEM BEI for ZN-La, and the chemical compositions of the indexed areas measured by EDS are summarized in Table 4.4.

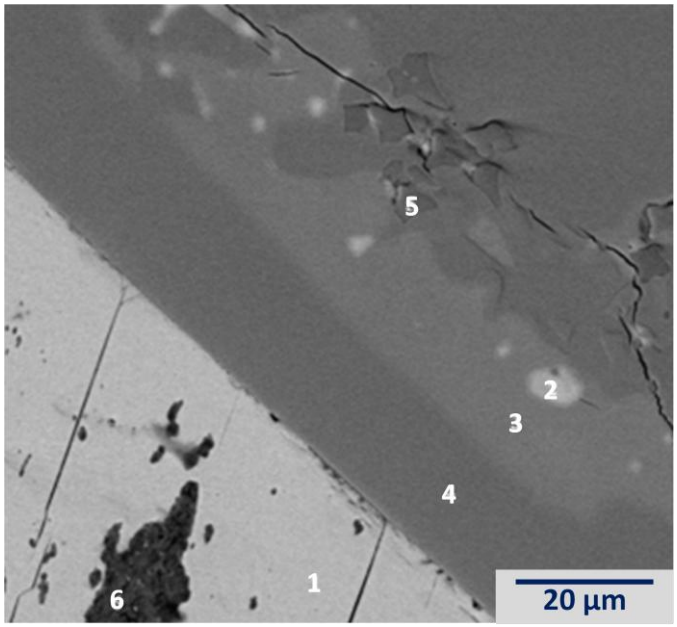

Figure 4.2q SEM BEI for ZN-LaA, and the chemical compositions of the indexed areas measured by EDS are summarized in Table 4.4.

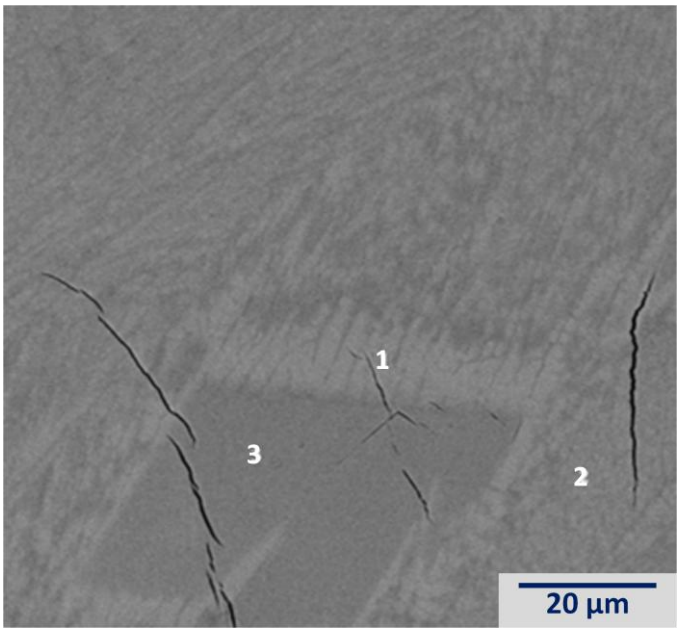

Figure 4.2r SEM BEI for ZN-Hf, and the chemical compositions of the indexed areas measured by EDS are summarized in Table 4.4.

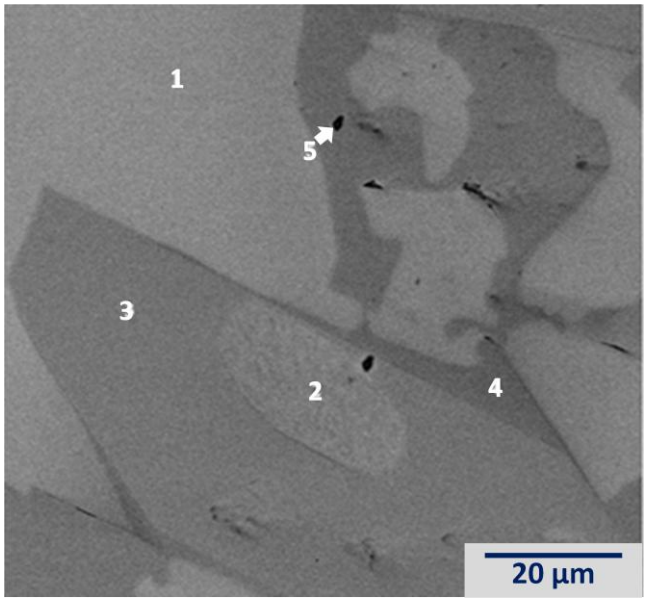

Figure 4.2s SEM BEI for ZN-HfA, and the chemical compositions of the indexed areas measured by EDS are summarized in Table 4.4.

Table 4.4 Summary of EDS results and assigned phases according to the stoichiometry and XRD results. All composition data are in at.%. Zr_7Ni_{10} (t) and Zr_7Ni_{10} (o) are tetragonal and orthorhombic structures of Zr_7Ni_{10}, respectively.

Alloy	**Area**	**Zr**	**Ni**	***X***	**(Ni+*X*)/Zr**	***e*/*a***	**Phase(s)**
ZN-Ni	Figure 4.2a-1	41.39	58.61	0.00	1.42	7.52	Zr_8Ni_{21} + ZrNi
	Figure 4.2a-2	28.14	71.86	0.00	2.55	8.31	Zr_8Ni_{21}
	Figure 4.2a-3	22.77	77.23	0.00	3.39	8.63	Zr_8Ni_{21} + $ZrNi_5$
	Figure 4.2a-4	96.23	3.77	0.00	0.04	4.23	ZrO_2
ZN-NiA	Figure 4.2b-1	36.51	63.49	0.00	1.74	7.81	Zr_8Ni_{21} + ZrNi
	Figure 4.2b-2	30.50	69.50	0.00	2.28	8.17	Zr_8Ni_{21} + ZrNi
	Figure 4.2b-3	26.78	73.22	0.00	2.73	8.39	Zr_8Ni_{21}
	Figure 4.2b-4	17.52	82.48	0.00	4.71	8.95	$ZrNi_5$
	Figure 4.2b-5	96.51	3.49	0.00	0.04	4.21	ZrO_2
ZN-Mg	Figure 4.2c-1	37.80	62.20	0.00	1.65	7.73	Zr_7Ni_{10} (t)
	Figure 4.2c-2	28.39	70.11	1.50	2.52	8.18	Zr_2Ni_7
	Figure 4.2c-3	12.61	24.92	62.47	6.93	4.25	Mg_2Ni

ZN-Al	Figure 4.2d-1	36.60	59.20	4.19	1.73	7.51	Zr_7Ni_{10} (t)
	Figure 4.2d-2	32.68	59.81	7.51	2.06	7.51	Zr_8Ni_{21} + Zr_7Ni_{10} (t)
	Figure 4.2d-3	21.49	66.94	11.57	3.65	7.90	Zr_2Ni_7
	Figure 4.2d-4	95.71	3.21	1.08	0.04	4.18	ZrO_2
ZN-AlA	Figure 4.2e-1	38.16	58.53	3.31	1.62	7.48	Zr_7Ni_{10} (t)
	Figure 4.2e-2	20.75	69.19	10.06	3.82	8.05	Zr_2Ni_7
	Figure 4.2e-3	20.62	68.53	10.85	3.85	8.00	Zr_2Ni_7
	Figure 4.2e-4	95.46	3.84	0.71	0.05	4.22	ZrO_2
	Figure 4.2e-5	92.50	6.38	1.12	0.08	4.37	ZrO_2
	Figure 4.2e-6	95.44	3.73	0.83	0.05	4.22	ZrO_2
ZN-Sc	Figure 4.2f-1	33.64	61.34	5.02	1.97	7.63	Zr_7Ni_{10} (t)
	Figure 4.2f-2	35.56	59.26	5.18	1.81	7.50	Zr_7Ni_{10} (t)
	Figure 4.2f-3	25.40	68.17	6.43	2.94	8.03	Zr_2Ni_7
	Figure 4.2f-4	10.32	25.70	63.99	8.69	4.90	Sc-Zr solid solution
ZN-ScA	Figure 4.2g-1	39.99	56.75	3.26	1.50	7.37	Zr_7Ni_{10} (t)
	Figure 4.2g-2	26.01	68.18	5.81	2.84	8.03	Zr_2Ni_7
	Figure 4.2g-3	4.76	7.56	87.68	20.01	3.58	Sc-Zr solid solution
ZN-V	Figure 4.2h-1	37.16	60.29	2.55	1.69	7.64	Zr_7Ni_{10} (t)
	Figure 4.2h-2	29.52	62.83	7.65	2.39	7.85	Zr_2Ni_7
	Figure 4.2h-3	23.24	71.40	5.36	3.30	8.34	Phase X
	Figure 4.2h-4	93.79	5.70	0.52	0.07	4.35	ZrO_2
ZN-VA	Figure 4.2i-1	28.69	64.65	6.67	2.49	7.95	Zr_2Ni_7
	Figure 4.2i-2	90.75	8.46	0.79	0.10	4.52	ZrO_2
	Figure 4.2i-3	89.63	9.35	1.02	0.12	4.57	ZrO_2
ZN-Mn	Figure 4.2j-1	37.00	59.32	3.68	1.70	7.67	Zr_7Ni_{10} (t)
	Figure 4.2j-2	22.93	72.27	4.80	3.36	8.48	Phase X
	Figure 4.2j-3	26.20	65.94	7.86	2.82	8.19	Zr_2Ni_7
	Figure 4.2j-4	93.51	5.94	0.55	0.07	4.37	ZrO_2

ZN-MnA	Figure 4.2.2k-1	39.54	58.53	1.93	1.53	7.57	Zr_7Ni_{10} (t)
	Figure 4.2k-2	28.46	64.92	6.63	2.51	8.09	Zr_2Ni_7
	Figure 4.2k-3	84.00	14.50	1.50	0.19	4.92	ZrO_2
	Figure 4.2k-4	92.76	6.58	0.66	0.08	4.41	ZrO_2
ZN-Co	Figure 4.2l-1	40.14	57.92	1.94	1.49	7.57	Zr_7Ni_{10} (t)
	Figure 4.2l-2	28.79	63.30	7.91	2.47	8.19	Zr_2Ni_7
	Figure 4.2l-3	23.31	68.73	7.97	3.29	8.52	Phase X
	Figure 4.2l-4	96.58	3.18	0.24	0.04	4.20	ZrO_2
ZN-CoA	Figure 4.2m-1	28.58	64.95	6.47	2.50	8.22	Zr_2Ni_7
	Figure 4.2m-2	29.16	64.68	6.17	2.43	8.19	Zr_2Ni_7
	Figure 4.2m-3	23.15	71.36	5.50	3.32	8.56	Phase X
	Figure 4.2m-4	93.81	5.87	0.31	0.07	4.37	ZrO_2
ZN-Sn	Figure 4.2n-1	27.13	48.88	23.99	2.69	9.33	Zr_2Ni_2Sn
	Figure 4.2n-2	37.33	60.98	1.69	1.68	7.83	Zr_7Ni_{10} (t)
	Figure 4.2n-3	26.40	63.04	10.56	2.79	8.84	$ZrNi_2Sn$
	Figure 4.2n-4	28.46	71.09	0.44	2.51	8.31	Zr_2Ni_7
	Figure 4.2n-5	24.68	75.54	0.77	3.09	8.65	Phase X
	Figure 4.2n-6	89.72	9.38	0.90	0.11	4.65	ZrO_2
ZN-SnA	Figure 4.2o-1	40.80	40.69	18.51	1.45	8.29	Zr_2Ni_2Sn
	Figure 4.2o-2	27.39	48.00	24.61	2.65	9.34	$ZrNi_2Sn$
	Figure 4.2o-3	26.89	48.10	25.01	2.72	9.39	$ZrNi_2Sn$
	Figure 4.2o-4	28.71	70.88	0.42	2.48	8.30	Zr_8Ni_{21}
	Figure 4.2o-5	29.62	69.62	0.76	2.38	8.25	Zr_8Ni_{21}
	Figure 4.2o-6	93.36	5.63	1.01	0.07	4.44	ZrO_2
ZN-La	Figure 4.2p-1	0.21	49.51	50.28	475.19	6.47	LaNi
	Figure 4.2p-2	40.23	59.33	0.45	1.49	7.56	Zr_7Ni_{10} (o)
	Figure 4.2p-3	28.67	71.04	0.29	2.49	8.26	Zr_8Ni_{21}
	Figure 4.2p-4	0.26	80.64	19.10	383.62	8.65	$LaNi_5$

ZN-LaA	Figure 4.2q-1	0.10	49.67	50.23	999.00	6.48	LaNi
	Figure 4.2q-2	4.71	53.71	41.58	20.23	6.81	LaNi
	Figure 4.2q-3	42.56	57.27	0.17	1.35	7.43	Zr_7Ni_{10} (o)
	Figure 4.2q-4	28.65	71.16	0.19	2.49	8.27	Zr_8Ni_{21}
	Figure 4.2q-5	96.15	3.61	0.24	0.04	4.21	ZrO_2
	Figure 4.2q-6	0.27	77.66	22.07	369.37	8.44	La_2Ni_7
ZN-Hf	Figure 4.2r-1	30.55	66.55	2.90	2.27	7.99	Zr_8Ni_{21} + Zr_7Ni_{10} (o)
	Figure 4.2r-2	26.93	70.64	2.43	2.71	8.24	Zr_8Ni_{21} + Zr_7Ni_{10} (o)
	Figure 4.2r-3	19.66	77.94	2.40	4.09	8.68	Zr_8Ni_{21}
ZN-HfA	Figure 4.2s-1	32.02	65.14	2.83	2.12	7.91	Zr_8Ni_{21} + Zr_7Ni_{10} (o)
	Figure 4.2s-2	29.46	68.12	2.41	2.39	8.09	Zr_8Ni_{21} + Zr_7Ni_{10} (o)
	Figure 4.2s-3	19.62	77.94	2.44	4.10	8.68	Zr_8Ni_{21}
	Figure 4.2s-4	22.36	76.16	1.47	3.47	8.57	Zr_8Ni_{21}
	Figure 4.2s-5	96.12	0.81	3.08	0.04	4.04	ZrO_2

4.2.1 Zr_8Ni_{21} base alloy

The XRD pattern of ZN-Ni is composed of mainly Zr_8Ni_{21} peaks (Figure 4.1a). Besides the reflections from Zr_8Ni_{21}, there is one extra broad peak at around 38.5°. In the studies of AB_2 and A_7B_{10} alloys, similar broad peaks were found and assigned to orthorhombic ZrNi phase [10, 26, 85]. A peak at the same angle had also been recorded in the XRD pattern of Zr_8Ni_{21} reported previously [59]. The unit cell of Zr_8Ni_{21} is smaller than that listed in the database (Table 4.3). Due to the formation of ZrNi, the Zr/Ni ratio in Zr_8Ni_{21} phase is decreased. This hyper-stoichiometry may have caused anti-site defect (partial replacement of Zr by Ni in the A-site) or vacancy defect (vacant A-site as a result of insufficient amount of Zr) in the structure and consequently reduces the unit cell volume. Since the peak of ZrNi is broad, which corresponds to very fine crystallites, individual ZrNi grains are too fine to be seen in the SEM micrograph

(Figure 4.2a). Instead, ZrNi grains are distributed throughout the Zr_8Ni_{21} matrix and form area 1. Although $ZrNi_5$ is not detected by XRD, area 3 is suspected to be a mixture of Zr_8Ni_{21} and $ZrNi_5$ due to its (Ni + *X*)/Zr ratio and the discovery of $ZrNi_5$ existence in the annealed sample discussed later in this section.

After annealing, the Zr_8Ni_{21} phase predominates the microstructure, and the broad peak at around 38.5° is still present (Figure 4.1b) with an intensity lower than the one prior to annealing while the intensities of other peaks increase after annealing. Since annealing decreases the amount of secondary phases, the XRD results before and after annealing further show that the broad peak at around 38.5° does not belong to Zr_8Ni_{21} family and should be ZrNi. The unit cell volume of Zr_8Ni_{21} is similar to that from the unannealed sample. From the SEM micrograph (Figure 4.2b), fine grains of ZrNi are mixed throughout the Zr_8Ni_{21} matrix and increase the Zr-contents in areas 1 and 2. Occasionally, dagger-shaped $ZrNi_5$ grains are found in the SEM micrograph (area 4), but the amount is too small to be detected by XRD. This observation also shows that despite not being seen in the micrograph, $ZrNi_5$ exists as fine crystallite in the unannealed alloy. The annealing process promotes the accumulation of the fine $ZrNi_5$ grains, which is evident in the SEM micrograph.

4.2.2 $Zr_8Ni_{19}Mg_2$ alloy

Mg is much larger and lighter than Ni with large differences in both electronegativity and number of outer-shell electrons. The XRD pattern of ZN-Mg shows a peak profile composed of tetragonal Zr_7Ni_{10} phase (Zr_7Ni_{10} (t)) and a FCC-structured phase, which is designated as Zr_2Ni_7 on the basis of the EDS result and understanding of possible phase formation discussed later in this section (Figure 4.1c). Zr_7Ni_{10} is an important secondary phase formed by a solid

transformation from B2 during the solidification of common AB_2 MH alloys [25]. Two structures are available for Zr_7Ni_{10} stoichiometry: the as-prepared Zr_7Ni_{10}, which usually shows an orthorhombic structure, and the material after hydride/dehydride cycling or prepared by quenching, which exhibits a tetragonal structure [66, 67]. While the unit cell of Zr_7Ni_{10} (t) is slightly smaller than the one calculated based on the database, the unit cell of Zr_2Ni_7 is 10% larger than the stoichiometric Zr_2Ni_7 crystal.

The SEM micrograph shows a Zr_7Ni_{10} matrix with granular Zr_2Ni_7 and occasional Mg_2Ni inclusions (Figure 4.2c). The solubility of Mg in the Zr_7Ni_{10} matrix is not detectable by EDS due to the immiscible nature of Mg and Zr (Table 4.2). The (Ni + *X*)/Zr ratio in Zr_7Ni_{10} phase is higher than the stoichiometric value (1.43), which can be used to explain its slightly smaller unit cell when compared to that listed in the database. This hyper-stoichiometry indicates a composition range of the Zr_7Ni_{10} phase, which is closer to the original phase diagram proposed by Massalski [106]. It is suspected that the raw materials used in Massalski's version of the phase diagram are not 100% pure, which is similar to this study where additional modifiers are added into the formula, so the composition range of Zr_7Ni_{10} widens from the narrow line suggested by Okamoto [57] (Figure 1.8). Regarding the peaks from an FCC structure, in the Zr-Ni system, an AB_2 (C15) FCC structure is not available. Both Zr_2Ni_7 and $ZrNi_5$ have similar reflection patterns in the same neighborhood. Considering the (Ni + *X*)/Zr ratio, this FCC-structured phase is assigned to Zr_2Ni_7. However, this ratio is much lower than the stoichiometry of Zr_2Ni_7 (3.50). In contrast with the effect of hyper-stoichiometry discussed previously, this hypo-stoichiometry increases the unit cell volume of the Zr_2Ni_7 phase.

4.2.3 $Zr_8Ni_{19}Al_2$ alloy

Al is another light element used in this study. Similar to the case of Mg, Al is larger than Ni with smaller differences in electronegativity and number of outer-shell electrons. The XRD pattern from unannealed ZN-Al shows a mixture of Zr_7Ni_{10} (t), Zr_2Ni_7, Zr_8Ni_{21}, and ZrNi phases (Figure 4.1d). Due to the hyper-stoichiometry in Zr_7Ni_{10} (t) (Table 4.4), which is similar to the case in ZN-Mg, the unit cell of Zr_7Ni_{10} (t) in ZN-Al is smaller than that listed in the database. The unit cell of Zr_2Ni_7 in ZN-Al is the largest among all the Zr_2Ni_7 phases observed in this study (all are higher than the published data). Although the metallic radius of Al is not the largest among the modifying elements and the Zr_2Ni_7 phase in ZN-Al is the only one that doesn't show hypo-stoichiometry among the Zr_2Ni_7 phases observed in this study, Al shows exceptional solubility in Zr_2Ni_7 (the highest among all modifying elements), as seen in Table 4.4. The addition of the larger Al in the B-site is responsible for the Zr_2Ni_7 unit cell enlargement in ZN-Al. The SEM micrograph shows parallel band-structure of the Zr_7Ni_{10}, Zr_2Ni_7, and Zr_8Ni_{21} + Zr_7Ni_{10} phases (Figure 4.2d).

After annealing, the major features in the XRD pattern remain unchanged. The abundance of the main phase Zr_7Ni_{10} (t) increases while the minor phases such as ZrNi and Zr_8Ni_{21} decrease (Figure 4.1e). The unit cell volumes of both Zr_7Ni_{10} (t) and Zr_2Ni_7 remain the same after annealing due to their similar compositions compared to before annealing. The SEM micrograph shows a different banded pattern where a uniform band and a matrix-intergrowth band alternate throughout the sample (Figure 4.2e). In the area covered by this micrograph, the uniform band is Zr_2Ni_7 while the other is Zr_2Ni_7 imbedded in the Zr_7Ni_{10} matrix.

4.2.4 $Zr_8Ni_{19}Sc_2$ alloy

Sc has an electronegativity and metallic radius similar to those of Mg but has a smaller difference in number of outer-shell electrons when compared to Ni. Additionally, Sc forms a total solid solution with Zr, which is contrary to the case for Mg. Therefore a higher ratio of Sc to Zr than in the case of ZN-Mg is expected in all Zr-containing phases. The XRD pattern of ZN-Sc shows Zr_7Ni_{10} (t) and FCC Zr_2Ni_7 phases (Figure 4.1f). The unit cell volume of Zr_7Ni_{10} (t) is similar to that from ZN-Mg and ZN-Al. However, the unit cell volume of Zr_2Ni_7 is between those of ZN-Mg and Zn-Al due to the following phenomena: also affected by the hypo-stoichiometry in Zr_2Ni_7 phase, the solubility of Sc in Zr_2Ni_7 is higher than that of Mg as predicted and evidently seen in the EDS results; moreover, although Sc is larger than Al in size, the solubility of Sc in Zr_2Ni_7 is lower. The SEM micrograph shows a matrix mainly of Zr_7Ni_{10} with Zr_2Ni_7 intergrowth grains (Figure 4.2f). It is possible that the matrix contains one or more finer phases that are beyond the SEM resolution. The Ni-content in Zr_7Ni_{10} phase is higher than that in Zr_7Ni_{10} phase in ZN-Mg due to the incorporation of other Ni-rich phases (for example, $ZrNi_3$ or Zr_2Ni_7). These small crystallites cannot be seen in the XRD pattern due to their broad peak width. There is also a Sc-rich inclusion embedded in the solid (area 4).

After annealing, the phase abundance of Zr_7Ni_{10} (t) increases (Figure 4.1g). The lattice constants of both Zr_7Ni_{10} (t) and Zr_2Ni_7 remain the same after annealing. Small and large areas of Zr_2Ni_7 are seen in the SEM micrograph (Figure 4.2g). Therefore, it is likely that the fine grains in the matrix of unannealed ZN-Sc are Zr_2Ni_7 and grow into the small granules in the annealed sample (also, the Zr_2Ni_7 intergrowth grains of the unannealed sample grow into the large Zr_2Ni_7 in the annealed sample). The Sc-rich inclusion becomes even higher in Sc-content after annealing. As a consequence, the Sc-content in Zr_7Ni_{10} reduces after annealing.

4.2.5 $Zr_8Ni_{19}V_2$ alloy

V is slightly larger and has a lower electronegativity and fewer number of outer-shell electrons than Ni. The XRD pattern of the unannealed alloy shows a Zr_2Ni_7-predominant structure with a small amount of Zr_7Ni_{10} (t) (Figure 4.1h). Although still larger than the unit cell listed in the database, the unit cell of Zr_2Ni_7 is slightly smaller than those of ZN-Mg, ZN-Al, and ZN-Sc due to V's smaller size compared to Mg, Al, and Sc. The unit cell of Zr_7Ni_{10} (t) is much smaller than those from ZN-Mg, ZN-Al, and ZN-Sc and may have been caused by the partial replacement of Zr by the smaller-sized V in the A-site. This finding is different from the result found in the study conducted by Young et al. where V was added into pure $(TiZr)_7Ni_{10}$ alloy, and the unit cell expands due to the partial substitution of Ni by V [85]. The SEM micrograph of ZN-V shows a Zr_2Ni_7 matrix with Zr_7Ni_{10} dendritic secondary phase within (Figure 4.2h). There is also a Ni-rich phase shown as a narrow line (area 3) in the micrograph. Although the XRD analysis did not pick up any extra phase, an XRD reflection peak is found at round 38.4° in some samples (see sections 4.2.7 and 4.2.8) with approximately the same EDS (Ni + *X*)/Zr ratio compared to area 3 of the ZN-V micrograph. Therefore, this composition of the Ni-rich phase will be designated as Phase X in the rest of this chapter.

After annealing, the XRD pattern is composed of only peaks from the Zr_2Ni_7 phase (Figure 4.1i), with a unit cell slightly greater than that from the annealed sample. There is no trace of either Zr_7Ni_{10} or Phase X in the SEM micrograph (Figure 4.2i).

4.2.6 $Zr_8Ni_{19}Mn_2$ alloy

Mn is similar in size but has a lower electronegativity and fewer number of outer-shell electrons than Ni. Similar to the case of V-substitution, the XRD of ZN-Mn shows a Zr_2Ni_7-

predominant structure with a small amount of Zr_7Ni_{10} (t) (Figure 4.1j). While the unit cell of Zr_2Ni_7 is larger than that listed in the database due to its hypo-stoichiometry, the unit cell of the Zr_7Ni_{10} (t) phase is smaller due to its hyper-stoichiometry. Area 2 is labeled as Phase X based on its composition although no corresponding XRD peaks are found. Moreover, the micrograph shows the alternating pattern of Zr_7Ni_{10} (t), Phase X, and Zr_2Ni_7 (Figure 4.2j).

After annealing, while peaks from the Zr_7Ni_{10} minor phase cannot be detected by the XRD analysis (Figure 4.1k), a small area of the Zr_7Ni_{10} minor phase can still be observed in the SEM micrograph (Figure 4.2k). The unit cell volume of the main phase Zr_2Ni_7 increases slightly after annealing as a result of the reduction in (Ni + *X*)/Zr ratio.

4.2.7 $Zr_8Ni_{19}Co_2$ alloy

Co is similar to Ni in size as in the case of Mn. Moreover, due to their neighboring positions in the periodic table, the electronegativity of Co is very close to that of Ni, and the number of outer-shell electrons of Co is only slightly fewer than that of Ni. As discussed in the cases of V and Mn partial replacements, the XRD of ZN-Co shows a Zr_2Ni_7-predominant structure with a small amount of Zr_7Ni_{10} (t) (Figure 4.1l). In addition, small peaks attributed to $ZrNi_5$ (around 44.8°) and Phase X (around 38.4°) are also observed. Both unit cell volumes of Zr_2Ni_7 and Zr_7Ni_{10} (t) are similar to those from ZN-Mn alloy due to the same deviations from the stoichiometric ratios in ZN-Mn. In the SEM micrograph, area 3 with slightly darker contrast has a high Ni-content and is assigned as Phase X (Figure 4.2l). The $ZrNi_5$ phase identified by XRD is not visible in the SEM micrograph. A more random-shape alternating pattern of Zr_7Ni_{10} (t), Zr_2Ni_7, and Phase X is observed.

After annealing, the XRD peaks from the Zr_7Ni_{10} minor phase disappear, but the peak from Phase X remains (Figure 4.1m). The unit cell volume of the main phase Zr_2Ni_7 reduces slightly after annealing. The SEM micrograph exhibits a uniform Zr_2Ni_7 background with occasional streaks of Phase X (Figure 4.2m).

Since only Zr_2Ni_7 peaks and the peak at 38.4° are present in the XRD pattern and only Zr_2Ni_7 and a high Ni-content phase are observed in the SEM micrograph, ZN-CoA has directly validated the linking of the peak at 38.4° to an EDS calculated Ni-rich stoichiometry of approximately Zr_2Ni_7, or Phase X. This finding in ZN-CoA is the base of all Phase X designations in the samples discussed earlier. Furthermore, Phase X may be another crystal structure with a nominal Zr_2Ni_7 stoichiometry, which has not been formerly reported.

4.2.8 $Zr_8Ni_{19}Sn_2$ alloy

Sn has a larger metallic radius than Ni. Also, Sn is the only modifying element used in this study having more outer-shell electrons and a larger electronegativity than Ni. Sn as an additive in AB_2 MH alloy has been studied extensively for the purpose of reducing raw material costs by using zircaloy scrap (Zr-Sn) [118]. The research shows that small amounts of Sn occupy the A-site and replace Zr, while larger amounts of Sn occupy the B-site [118]. The XRD pattern of ZN-Sn shows a Zr_2Ni_7-predominant structure with many secondary phases such as $ZrNi_5$, Phase X, and two Sn-containing $ZrNi_2Sn$ and Zr_2Ni_2Sn (Figure 4.1n). The unit cell of the Zr_2Ni_7 phase is larger than that listed in the database due to its hypo-stoichiometry. The SEM micrograph shows a large number of small intergrowths of various secondary phases (mainly $ZrNi_2Sn$) within the matrix of Zr_2Ni_7 (Figure 4.2g). The Sn-content in Zr_xNi_y phases are lower due to the formation of Sn-containing phases.

The XRD pattern of ZN-SnA shows a substantial reduction in Zr_2Ni_7 and the appearance of Zr_8Ni_{21} (Figure 4.1o). The phase abundance of $ZrNi_2Sn$ increases at the expense of Zr_2Ni_2Sn. In the SEM micrograph, larger inclusions of $ZrNi_2Sn$ and Zr_2Ni_2Sn Sn-rich phases can be observed within the Sn-poor Zr_8Ni_{21} matrix (Figure 4.2o). Sn, when combined with annealing, is the only supplemental element that promotes an increase in Zr_8Ni_{21} phase abundance.

4.2.9 $Zr_8Ni_{19}La_2$ alloy

La is the largest modifying element of the series; however, it has one of the lower numbers of outer-shell electrons and the lowest electronegativity among all the modifying elements. La was selected as a supplement that would potentially enlarge the unit cell and increase the M-H bonding, consequently enhance the storage capacity. The XRD pattern of ZN-La shows two predominant Zr_8Ni_{21} and orthorhombic-structured Zr_7Ni_{10} phases with two La-containing LaNi and $LaNi_5$ phases (Figure 4.1p). The unit cell volumes of Zr_7Ni_{10} (o) and Zr_8Ni_{21} are similar to those listed in the database. Additionally, the unit cell of the Zr_8Ni_{21} phase is larger than that of the base alloy ZN-Ni due to the larger-sized La occupying the B-site and its lower (Ni + *X*)/Zr ratio compared to that in ZN-Ni. The SEM micrograph shows random crisscrossing matrices of larger Zr_8Ni_{21} grains and granular mixtures of the Zr_7Ni_{10} and Zr_8Ni_{21} phases (Figure 4.2p). Occasionally, large inclusions of LaNi and $LaNi_5$ mixtures are found due to the immiscibility between La and Zr. Only very small amounts of La are present in Zr_xNi_y phases.

After annealing, the phase abundance of Zr_7Ni_{10} (o) increases and a new Zr_2Ni_7 phase appears at the expense of Zr_8Ni_{21} (Figure 4.1q). Due to the hypo-stoichiometry in the Zr_2Ni_7 phase, its unit cell is larger than that listed in the database. According to the EDS results, the

unit cell of Zr_7Ni_{10} (o) is smaller than that from the unannealed sample as a result of the reduction in La. In the SEM micrograph, the main phase Zr_7Ni_{10} and La-containing phases have grown into larger grains after annealing (Figure 4.2q). Also, after annealing, each phase becomes more distinct. It should be noted that the stoichiometries in Zr_7Ni_{10} (o) and Zr_8Ni_{21} phases are very close to the ideal ratio.

4.2.10 $Zr_8Ni_{19}Hf_2$ alloy

Hf is the only substituting element in the same group as Zr. Along with Zr and Ti, Hf is one of the commonly used A-site elements for AB_2 alloys. Ti was not chosen due to its smaller size and its modifying effect of increasing the already higher heat of hydride formation of Zr_8Ni_{21} [95]. Other than its slightly smaller metallic radius, Hf has very similar chemical properties to Zr and forms a solid solution with Zr during solidification. Therefore, Hf is expected to occupy the A-site and partially replaces Zr. The XRD pattern of ZN-Hf shows a combination of Zr_8Ni_{21} and Zr_7Ni_{10} (o) (Figure 4.1r). No new Hf-containing phase is found as in the cases of other large atom-substitutions, such as Mg, Sc, Sn, and La. The unit cells of Zr_7Ni_{10} (o) and Zr_8Ni_{21} are smaller than those listed in the database. In fact, the unit cell of Zr_8Ni_{21} is the smallest among all Zr_8Ni_{21} phases observed in this study. Since Hf is likely in the A-site, its smaller size compared to Zr reduces the unit cell volumes of Zr_7Ni_{10} (o) and Zr_8Ni_{21}. The SEM micrograph shows an uneven distribution of small Zr_7Ni_{10} grains in the matrix of Zr_8Ni_{21} phase (Figure 4.2r). Occasionally, large grains of Zr_8Ni_{21} are apparent (area 3). In other areas, Zr_7Ni_{10} is mixed in with Zr_8Ni_{21} at difference ratios. The assigned Zr_8Ni_{21} phase has a (Ni + *X*)/Zr ratio that is higher than the stoichiometry of Zr_8Ni_{21} due to the possible occupancy of Hf in the A-site.

After annealing, there is no major change in the XRD pattern (Figure 4.1s). While the unit cell volume of Zr_8Ni_{21} remains the same, the unit cell of Zr_7Ni_{10} (o) is smaller than that of the unannealed sample. According to the SEM micrograph of ZN-HfA, the sizes of grains are greater after annealing (Figure 4.2s). Areas 1 and 2 are from the mixtures of Zr_7Ni_{10} and Zr_8Ni_{21} determined by the compositions, and areas 3 and 4 are Zr_8Ni_{21} with different compositions. Since both Zr_8Ni_{21} and Hf_8Ni_{21} phases are stable inter-metallic alloys, the $(ZrHf)_8Ni_{21}$ alloy should exist over a large range of Zr/Hf composition. Moreover, not all A-sites are equivalent [83]; therefore, there may be some preferential A-sites for the Hf atom in the A_8B_{21} structure, which accounts for the two phases that have the same structure but slightly different compositions (area 3 and 4).

4.3 Summary

The effects of partial-Ni substitution and annealing treatment on the structural properties of Zr_8Ni_{21}, a candidate to replace the currently used misch-metal based AB_5 MH alloy, have been presented. With the exception of Sn-substitution, the general effect of annealing is an increase in abundance of the predominant phase and reductions in both number and abundance of secondary phases. The major phase of the Sn-containing alloy transforms from Zr_2Ni_7 to Zr_8Ni_{21}. Summarized in Table 4.5, the microstructures of materials in this study can be classified into four groups according to their main phase: Zr_8Ni_{21}, Zr_7Ni_{10} (t), Zr_2Ni_7, and Zr_7Ni_{10} (o).

Table 4.5 Summary of XRD and EDS results

	Main phase	**Phase distribution**
ZN-Ni	Zr_8Ni_{21} (triclinic)	Zr_8Ni_{21} matrix with very fine ZrNi grains
ZN-NiA	Zr_8Ni_{21} (triclinic)	Zr_8Ni_{21} matrix with very fine ZrNi grains
ZN-Mg	Zr_7Ni_{10} (tetragonal)	Zr_7Ni_{10} matrix with Zr_2Ni_7 grains
ZN-Al	Zr_7Ni_{10} (tetragonal)	Zr_7Ni_{10}-Zr_2Ni_7-(Zr_8Ni_{21} + Zr_7Ni_{10}) banded pattern
ZN-AlA	Zr_7Ni_{10} (tetragonal)	Zr_7Ni_{10}-Zr_2Ni_7 banded pattern
ZN-Sc	Zr_7Ni_{10} (tetragonal)	Zr_7Ni_{10} matrix with Zr_2Ni_7 grains
ZN-ScA	Zr_7Ni_{10} (tetragonal)	Zr_7Ni_{10} matrix with Zr_2Ni_7 grains
ZN-V	Zr_2Ni_7 (cubic)	Zr_2Ni_7 with Zr_7Ni_{10} secondary phase
ZN-VA	Zr_2Ni_7 (cubic)	Zr_2Ni_7 only
ZN-Mn	Zr_2Ni_7 (cubic)	Zr_2Ni_7-Zr_7Ni_{10} banded pattern
ZN-MnA	Zr_2Ni_7 (cubic)	Zr_2Ni_7 with Zr_7Ni_{10} secondary phase
ZN-Co	Zr_2Ni_7 (cubic)	Zr_2Ni_7 with Zr_7Ni_{10} secondary phase
ZN-CoA	Zr_2Ni_7 (cubic)	Zr_2Ni_7 only
ZN-Sn	Zr_2Ni_7 (cubic)	Zr_2Ni_7 matrix with Zr_7Ni_{10} and Sn-rich grains
ZN-SnA	Zr_8Ni_{21} (triclinic)	Zr_8Ni_{21} matrix with Sn-rich grains (ZN-SnA)
ZN-La	Zr_7Ni_{10} (orthorhombic)	Zr_7Ni_{10} matrix with Zr_8Ni_{21} secondary phase and La-rich grains
ZN-LaA	Zr_7Ni_{10} (orthorhombic)	Zr_7Ni_{10} matrix with Zr_8Ni_{21} secondary phase and La-rich grains
ZN-Hf	Zr_7Ni_{10} (orthorhombic)	Zr_7Ni_{10} matrix with Zr_8Ni_{21} secondary phase
Zn-HfA	Zr_7Ni_{10} (orthorhombic)	Zr_7Ni_{10} matrix with Zr_8Ni_{21} secondary phase

By comparing this summary to the properties of the supplement elements as listed in Table 4.1, it can be seen that the number of outer-shell electrons has a direct correlation with the choice of the main phase. As the number of outer-shell electrons, which determines the average electron density (*e*/*a*), increases in the order of (Mg < Sc = Al) = (La < Hf) < (V< Mn < Co) < (Ni < Sn), the main phase of the annealed samples evolves from Zr_7Ni_{10} (t), to Zr_7Ni_{10} (o), Zr_2Ni_7,

and finally Zr_8Ni_{21}. As discussed in CHAPTER 2, the same parameter also controls the choice between the two main structures for AB_2 alloys [23, 40, 41, 80, 123-125], where, as *e*/*a* increases, the structure transforms from hexagonal C14 to FCC C15. As the B-content in main phase increases, the maximum and reversible gaseous hydrogen storage capacities are expected to decrease and increase, respectively. The detailed gaseous hydrogen storage and electrochemical properties analyzed based on the structural characteristics obtained from this chapter will be presented in CHAPTER 5.

CHAPTER 5

EFFECTS OF ANNEALING ON $Zr_8Ni_{19}X_2$ (X = Ni, Mg, Al, Sc, V, Mn, Co, Sn, La, and Hf): HYDROGEN STORAGE AND ELECTROCHEMICAL PROPERTIES

Based on previous studies and information presented in CHAPTER 3, Zr_8Ni_{21} shows good reversibility in gaseous hydrogen storage [58], fast activation [56, 59], and excellent HRD [56, 59] and therefore is investigated as the potential metal hydride (MH) alloy for use as the negative electrode in nickel/metal hydride (Ni/MH) batteries. Due to the lack of AB_2 inter-metallic compound in the Zr-Ni binary phase diagram, the closest stoichiometries with suitable metal-hydrogen bond strengths for room temperature Ni/MH operation are Zr_7Ni_{10} and Zr_8Ni_{21}. The Zr_7Ni_{10} alloy system has been studied with three, four, and five constituent elements and reported previously [69, 85, 90, 93]. Zr_8Ni_{21} may provide improvement for high-rate applications due to its higher B-content [105]. Zr_8Ni_{21} is not formed congruently from the liquid; instead, Zr_2Ni_7 first solidifies from the liquid with a Zr-to-Ni ratio of 8 : 21 and later reacts with the remaining liquid to form Zr_8Ni_{21} alloy peritectically [82]. As a consequence, if the cooling temperature cannot be controlled at a very slow rate (as in the case of mass production processes), an annealing treatment is required to increase the abundance of the Zr_8Ni_{21} phase. However, previous studies on AB_2 alloys indicated that annealing deteriorates the electrochemical properties as a result of the removal of the secondary phases, which are beneficial due to the synergetic effects between the main Laves phases and the secondary phases [23, 26, 55, 56]. Therefore, a study of the annealing effects is crucial to the development of suitable MH alloys for Ni/MH applications. As a continuation of CHAPTER 4, this chapter will present both the gaseous phase hydrogen storage and the electrochemical properties of the same series of alloys and correlate these properties to the structural characteristics.

5.1 Experimental setup

Gaseous phase hydrogen storage characteristics were studied by PCT isotherm measurement using a Suzuki-Shokan 4-channel PCT system. Each sample was first activated by a 2-h thermal cycle between 300˚C and room temperature under 2.5 MPa H_2 pressure. The PCT isotherms at 30, 60, and 90˚C were then measured.

To prepare for the electrochemical measurements, each sample ingot was first ground and sized using a 200-mesh sieve. The sieved powder was then compacted onto an expanded nickel substrate by a 10-ton press to form a test electrode (about 1 cm^2 in size and 0.2 mm thick) without any binder. The electrochemical properties of these electrodes were measured in a flooded cell configuration using a partially pre-charged $Ni(OH)_2$ pasted counter electrode as the positive electrode and a 30 wt.% KOH solution as the electrolyte. For the discharge capacity measurement, the system was first charged at a current density of 50 mA g^{-1} for 10 h and then discharged at a current density of 50 mA g^{-1} until a cut-off voltage of –0.9 V was reached, then discharged at a current density of 12 mA g^{-1} until a cut-off voltage of –0.9 V was reached, and finally discharged at a current density of 4 mA g^{-1} until a cut-off voltage at –0.9 V was reached. For the surface reaction exchange current measurement, the linear polarization was performed by first fully charging the system, then discharging to 50% of depth-of-discharge, and followed by scanning the current in the potential range of –20 to +20 mV of the open circuit voltage at a rate of 0.1 mV s^{-1}. For the bulk hydrogen diffusion coefficient measurement, the system in a fully charged state was polarized at 0.6 V for 7200 s. All electrochemical measurements were performed in an Arbin Instruments *BT4+* Portable Battery Test System.

5.2 Results and discussion

5.2.1 Gaseous phase PCT analysis

The gaseous phase hydrogen storage characteristics of 19 samples (10 before and 9 after annealing) were studied by PCT isotherms measured at 30, 60, and 90 °C. Six PCT isotherms from ZN-Ni, ZN-NiA, ZN-La, ZN-LaA, ZN-Hf, and ZN-HfA were chosen to represent the general trends of the absorption and desorption curves (Figure 5.1a-f). The maximum storage capacity, reversible storage capacity, absorption and desorption plateau pressures, absorption/desorption hysteresis calculated from the 60 °C isotherm, and changes in entropy (ΔH) and enthalpy (ΔS) based on the 60 and 90 °C absorption plateau pressures for each alloy are listed in Table 5.1. Since the kinetics is slow at lower temperature (for instance, ZN-Ni 30 °C Des in Figure 5.1a), and at higher temperature, the temperature goes beyond the critical point of the temperature dome formed by connecting the end-points of all pressure plateaus [92] (ZN-NiA 90 °C Abs in Figure 5.1b), the absences of plateau regions are observed in some isotherms at lower and higher temperatures.

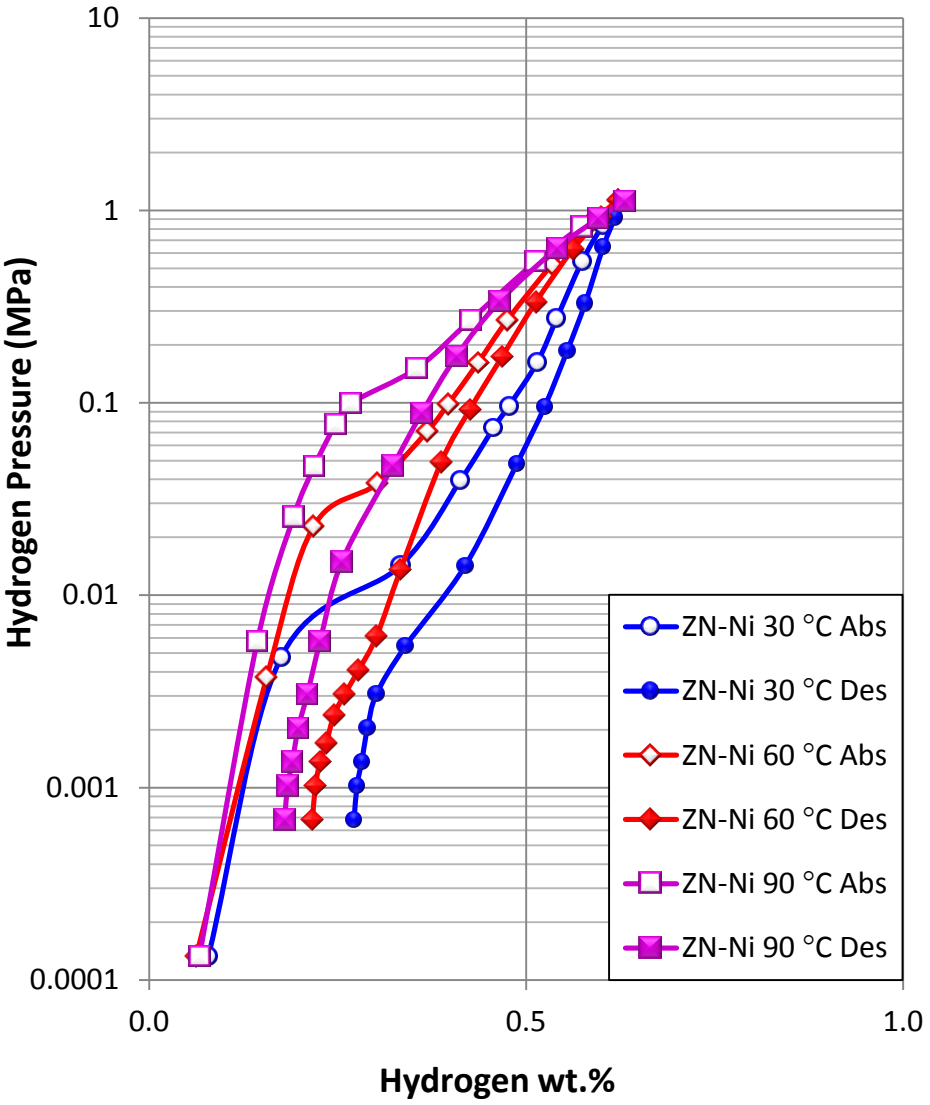

Figure 5.1a PCT isotherms of ZN-Ni, and open and solid symbols are for absorption and desorption curves, respectively.

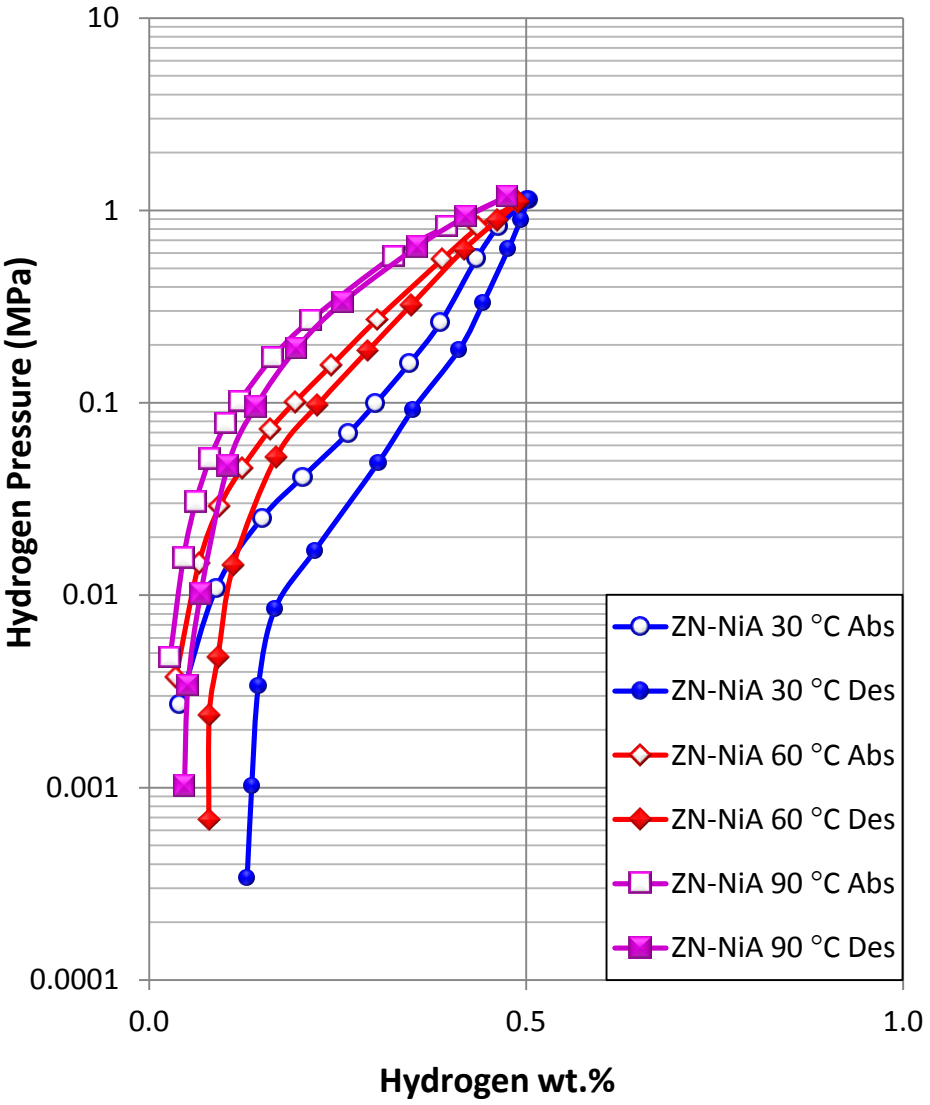

Figure 5.1b PCT isotherms of ZN-NiA, and open and solid symbols are for absorption and desorption curves, respectively.

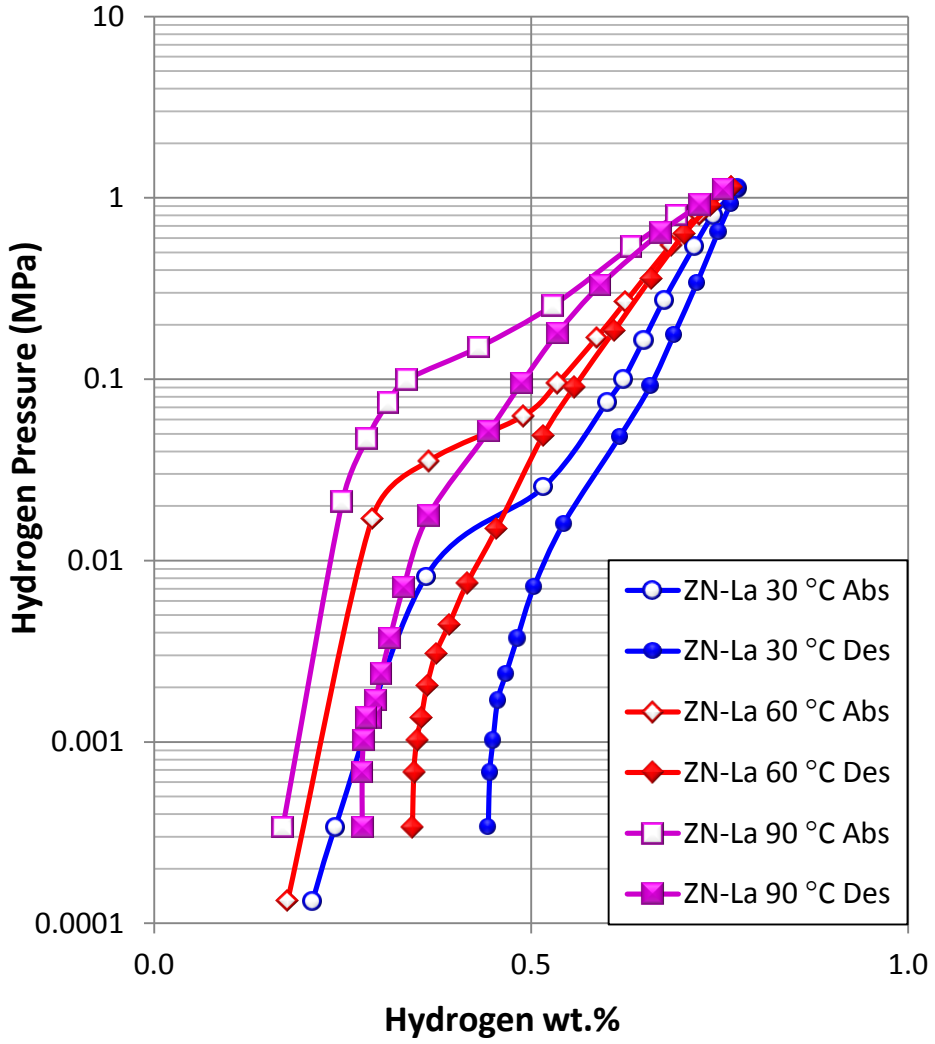

Figure 5.1c PCT isotherms of ZN-La, and open and solid symbols are for absorption and desorption curves, respectively.

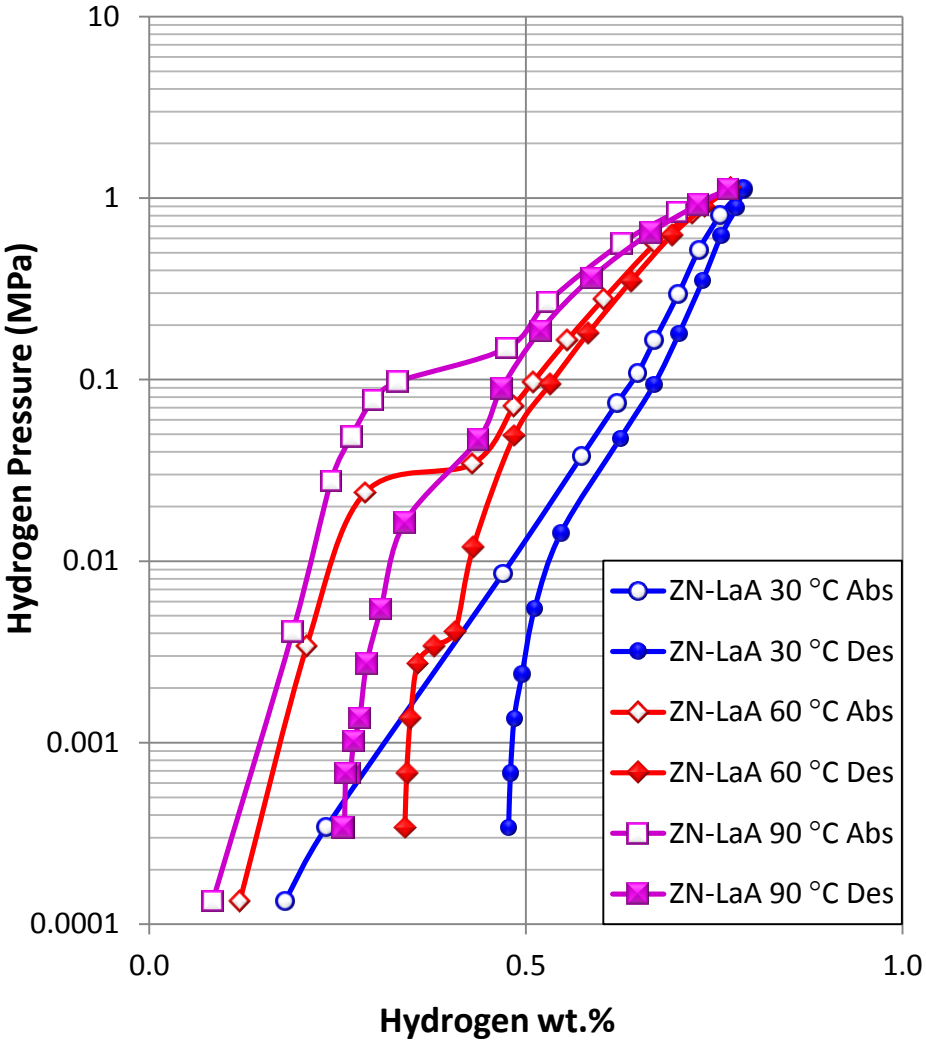

Figure 5.1d PCT isotherms of ZN-LaA, and open and solid symbols are for absorption and desorption curves, respectively.

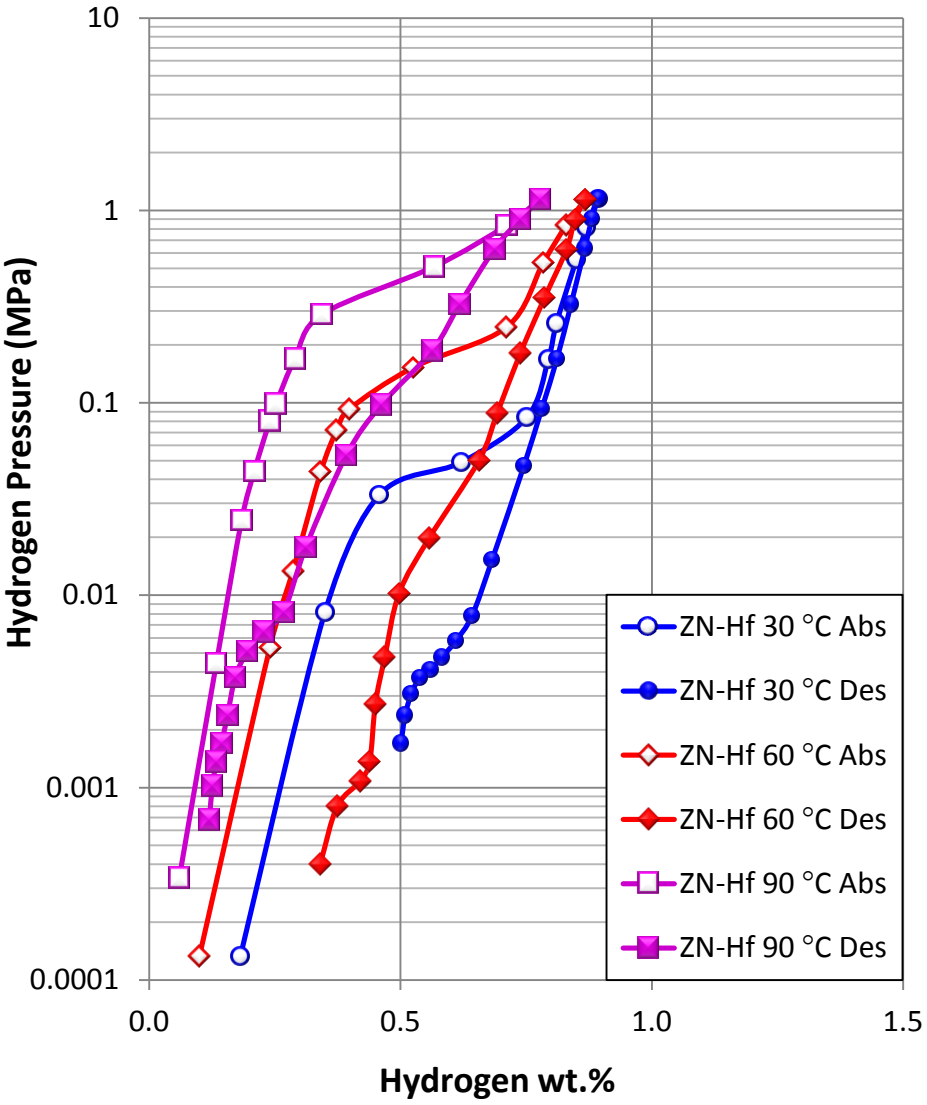

Figure 5.1e PCT isotherms of ZN-Hf, and open and solid symbols are for absorption and desorption curves, respectively.

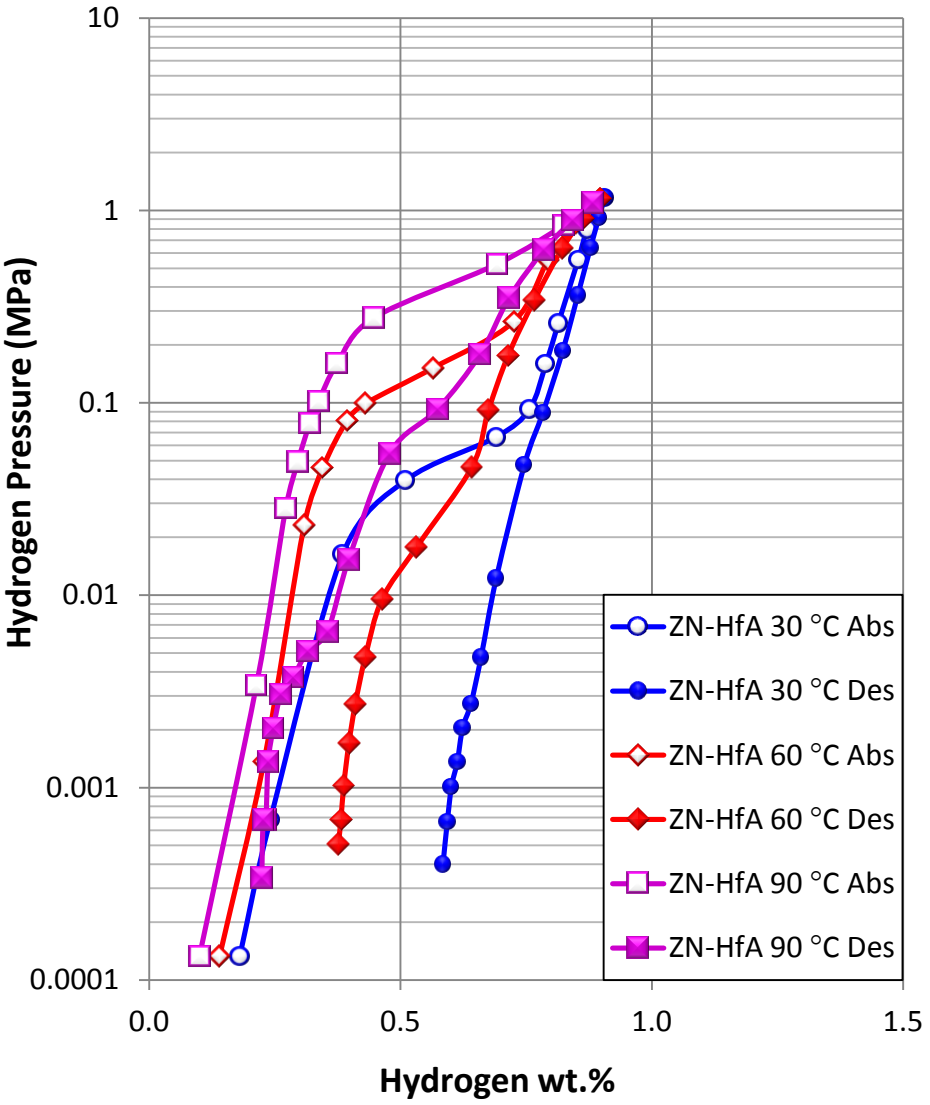

Figure 5.1f PCT isotherms of ZN-HfA, and open and solid symbols are for absorption and desorption curves, respectively.

Table 5.1 Summary of PCT measurements

	Maximum storage capacity (wt.%)			**Reversible storage capacity (wt.%)**			**Absorption plateau pressure (MPa)**			**Desorption plateau pressure (MPa)**			**Hysteresis**	**$-\Delta H$ (kJ mol^{-1} H_2)**	**$-\Delta S$ (J K^{-1} mol^{-1} H_2)**
Temperature	30 °C	60 °C	90 °C	30 °C	60 °C	90 °C	30 °C	60 °C	90 °C	30 °C	60 °C	90 °C	60 °C	Abs	Abs
ZN-Ni	0.63	0.62	0.63	0.36	0.41	0.45	0.0100	0.0320	0.1200	-	0.0024	0.0240	2.6	44	123
ZN-NiA	0.50	0.49	0.47	0.37	0.41	0.43	0.0267	0.0867	-	-	0.0127	-	1.9	-	-
ZN-Mg	0.48	0.47	0.47	0.11	0.26	0.36	-	0.0107	0.0373	-	0.0067	0.0253	0.5	42	107
ZN-Al	0.62	0.61	0.61	0.31	0.36	0.42	0.1200	0.1067	-	0.0037	0.0440	-	0.9	-	-
ZN-AlA	0.62	0.61	0.57	0.25	0.39	0.39	0.0827	0.0293	-	0.0067	0.0080	-	1.3	-	-
ZN-Sc	0.58	0.57	0.54	0.13	0.29	0.40	0.0160	0.0400	0.1413	0.0009	0.0051	0.0253	2.1	42	119
ZN-ScA	0.53	0.52	0.51	0.09	0.25	0.41	0.0080	0.0387	0.1173	-	0.0043	0.0227	2.2	37	104
ZN-V	0.31	0.31	0.30	0.20	0.24	0.25	-	0.1400	-	0.0160	0.0400	0.0667	1.3	-	-
ZN-VA	0.18	0.17	0.16	0.17	0.16	0.16	-	0.4267	-	-	0.3467	-	0.2	-	-
ZN-Mn	0.41	0.40	0.38	0.10	0.24	0.28	0.0333	0.1733	-	-	0.1067	-	0.5	-	-
ZN-MnA	0.20	0.20	0.19	0.19	0.19	0.17	-	0.0733	0.1200	-	-	-	-	-	-
ZN-Co	0.47	0.46	0.45	0.09	0.24	0.27	0.0133	0.0360	0.1333	-	0.0024	0.0240	2.7	44	123
ZN-CoA	0.25	0.24	0.21	0.19	0.21	0.19	0.1200	0.2800	0.3067	0.0051	0.0019	0.0053	5.0	36	109
ZN-Sn	0.38	0.37	0.36	0.21	0.29	0.32	0.0173	0.0307	0.0933	0.0040	0.0024	-	2.5	37	102
ZN-SnA	0.34	0.33	0.33	0.28	0.31	0.30	0.0320	0.0533	0.1600	0.0120	0.0240	-	0.8	37	105
ZN-La	0.77	0.77	0.76	0.32	0.42	0.49	0.0173	0.0480	0.1400	-	0.0100	0.0293	1.6	36	102
ZN-LaA	0.79	0.77	0.77	0.31	0.43	0.51	-	0.0307	0.1200	-	0.0037	0.0293	2.1	46	127
ZN-Hf	0.89	0.87	0.78	0.39	0.50	0.67	0.0507	0.1373	0.3867	0.0043	0.0187	0.1067	2.0	35	107
ZN-HfA	0.91	0.90	0.88	0.32	0.52	0.65	0.0520	0.1133	0.3067	-	0.0213	0.0773	1.7	33	101

The maximum storage capacities measured at 30 °C of each sample before and after annealing are plotted in Figure 5.2. Two horizontal lines are drawn for the ease of comparison with the capacities of the base alloys ZN-Ni and ZN-NiA (0.63 and 0.50 wt.%, respectively). These two storage capacities are consistent with 0.50 wt.% @ 25 °C measured from an alloy with the same composition after annealing at 1000 °C for 30 days [58]. Annealing decreases the maximum storage capacity in the base alloy due to the reduction of the ZrNi secondary phase as discussed in CHAPTER 3. While La- and Hf-substitutions improve the maximum storage capacities considerably, the capacity decreases for V-, Mn-, Co-, and Sn-substitutions. The maximum storage capacities before and after annealing are correlated to the metallic radius (listed in Table 4.1) of the supplemental element, and the resulting linear correlation factors (R^2) are 0.24 and 0.47, respectively. The correlation is improved after annealing and follows the MH alloy design trend: supplemental elements with larger metallic radii increase the cell volumes, and the larger cell volumes promote more stable hydrides with higher maximum storage capacities [116]. The main phase of each alloy based on the structural analysis reported in CHAPTER 4 is labeled in Figure 5.2. While alloys with Zr_7Ni_{10} (o) main phase have the highest maximum storage capacities, those with Zr_7Ni_{10} (t) main phase have the second highest, followed by those with Zr_8Ni_{21} main phase, and those with Zr_2Ni_7 main phase have the lowest capacities. This trend follows the B/A ratios of 1.43, 2.63, and 3.5 for Zr_7Ni_{10}, Zr_8Ni_{21}, and Zr_2Ni_7, respectively. The result also agrees with the maximum storage capacities of these three alloys reported by Joubert et al. [58]. Moreover, the difference in unit cell volumes of Zr_7Ni_{10} (o) and Zr_7Ni_{10} (t) causes the variation in their maximum storage capacities. With the purpose to compare the unit cell volumes of Zr_7Ni_{10} (o) and Zr_7Ni_{10} (t) from the same standpoint, a rhombus related to the base rectangle of Zr_7Ni_{10} (o) unit cell is constructed (Figure 5.3), where *a'* is the

side length (half of the diagonal of the original rectangle) and $\theta \neq 90°$ is the internal angle of the rhombus. For an alloy with the same composition, two possible structure alternations from Zr_7Ni_{10} (t) to Zr_7Ni_{10} (o) are presented in Figure 5.4, where both show that tilting of the tetragonal structure forms the orthorhombic structure. In order for the central atom in the base square of the tetragonal structure to remain fitted in the base rhombus of the orthorhombic structure, the unit cell is forced to expand as the structure changes from tetragonal to orthorhombic. This assumption is further confirmed by the observation of unit cell expansion reported by Takeshita et al. [66]. Therefore, as noted previously, although with the same composition, alloys with Zr_7Ni_{10} (o) main phase have higher maximum storage capacities than those with Zr_7Ni_{10} (t) main phase. For alloys with Zr_7Ni_{10} (o) main phase, the maximum storage capacities increase slightly after annealing due to the increases in abundance of the main phase. The maximum storage capacities of alloys with Zr_7Ni_{10} (t) main phase remain the same or slightly decrease after annealing as a result of the presence of the Zr_2Ni_7 secondary phase according to their XRD patterns as shown in CHAPTER 4. For alloys with Zr_8Ni_{21} or Zr_2Ni_7 main phase, the capacities decrease after annealing due to the reduction of secondary phases that assist in hydrogen absorption.

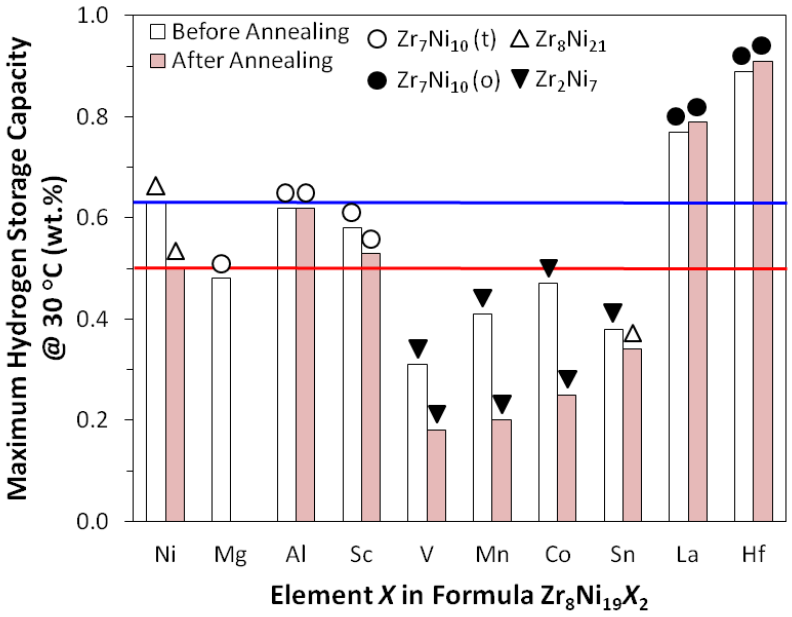

Figure 5.2 30 °C maximum gaseous phase hydrogen storage capacities measured by PCT for all alloys in this study. Horizontal lines mark the capacities from the base alloy ZN-Ni for easy comparison. Symbol on top of the data bar shows the main phase of the specific alloy.

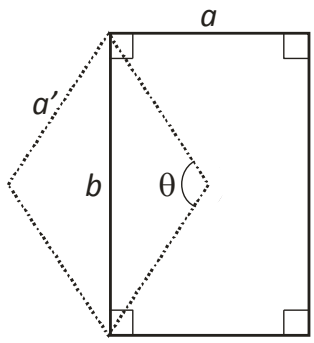

Figure 5.3 Schematic diagram of the two different presentations of the *a*-*b* plane of orthorhombic-structured Zr_7Ni_{10}

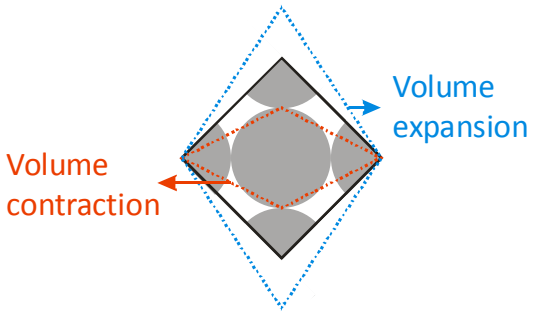

Figure 5.4 Schematic diagram of possible structure transformations from orthorhombic to tetragonal Zr_7Ni_{10}

The reversible storage capacities measured at 30 °C of each sample before and after annealing are plotted in Figure 5.5. Because of the higher B-content in Zr_8Ni_{21} and the outstanding maximum storage capacity in Zr_7Ni_{10} (o), alloys with Zr_8Ni_{21} or Zr_7Ni_{10} (o) main phase have higher reversible storage capacities than alloys with Zr_7Ni_{10} (t) or Zr_2Ni_7 main phase. After annealing, the reversible storage capacities of alloys with Zr_7Ni_{10} (o) or Zr_7Ni_{10} (t) main phases decrease due to the reduction or elimination of useful secondary phases for hydrogen desorption. For the base alloy, the reversible storage capacity after annealing shows marginal improvement as a result of the reduction of ZrNi phase that has non-reversible hydrogen capability [74, 93]. In most of alloys with Zr_2Ni_7 main phase, the reversible hydrogen storage capacities increase after annealing due to the increases in abundance of the main phase.

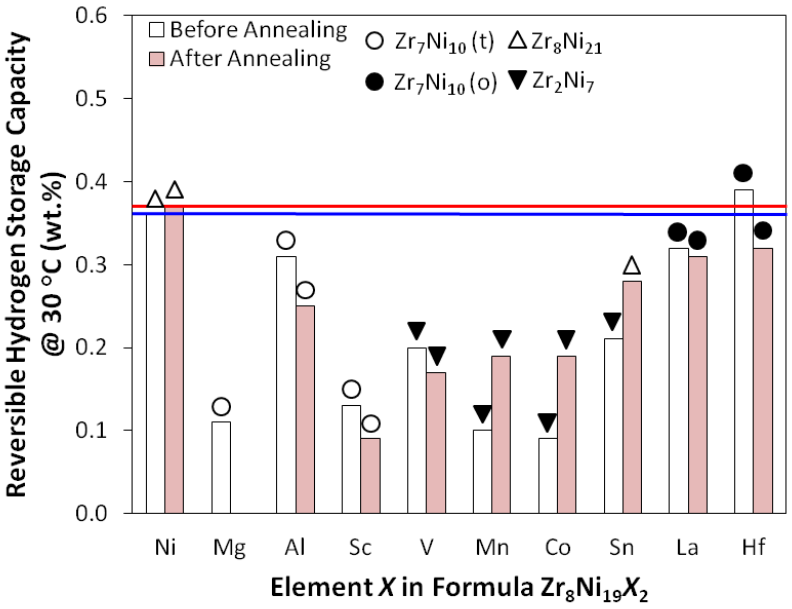

Figure 5.5 30 °C reversible gaseous hydrogen storage capacities measured by PCT for all alloys in this study. Horizontal lines mark the capacities from the base alloy ZN-Ni for easy comparison. Symbol on top of the data bar shows the main phase of the specific alloy.

The equilibrium plateau pressure is a measure of metal-hydrogen bond strength of MH alloys. Alloys with higher absorption plateau pressures have relatively weaker metal-hydrogen bonds. The 60 °C absorption plateau pressures of each sample before and after annealing are plotted in Figure 5.6. The plateau pressures of most alloys in this study fall into the range capable of room temperature hydrogen absorption/desorption [5]. Alloys with Zr_2Ni_7 main phase show relatively higher plateau pressures due to its highest B/A ratio. No clear relationship between the plateau pressure and the main phase can be established in other alloys. After annealing, the plateau pressures of alloys with Zr_7Ni_{10} (o) or Zr_7Ni_{10} (t) main phase decrease while those of alloys with Zr_8Ni_{21} main phase increase. However, alloys with Zr_2Ni_7 main phase show mixed results.

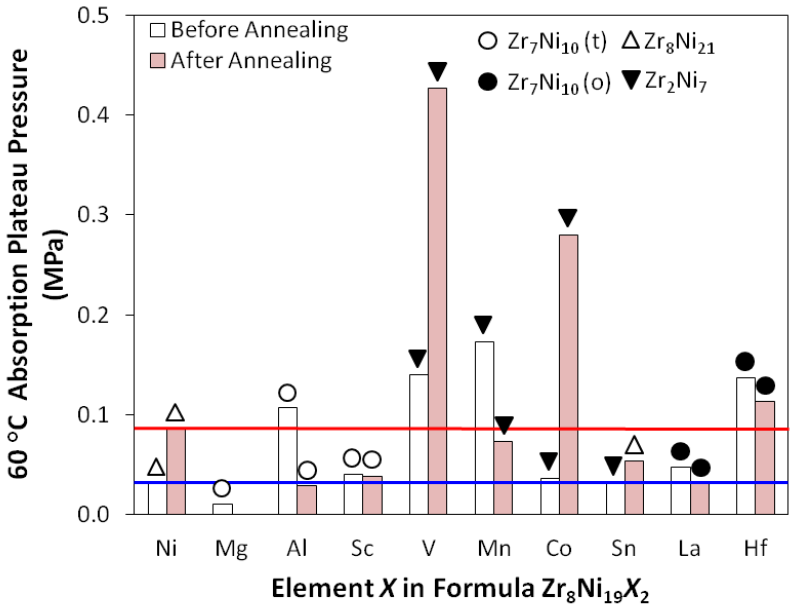

Figure 5.6 60 °C absorption plateau pressures measured by PCT for all alloys in this study. Horizontal lines mark the plateau pressures from the base alloy ZN-Ni for easy comparison. Symbol on top of the data bar shows the main phase of the specific alloy.

The PCT absorption/desorption hysteresis, defined as the difference between the absorption and desorption plateau pressures, was calculated by the equation

$$\textbf{Hysteresis} = \ln\left(\frac{P_a}{P_d}\right) \qquad \textbf{(5.1)}$$

where P_a is the absorption plateau pressure, and P_d is the desorption plateau pressure. Hysteresis can be used to predict the pulverization rate during hydride/dehydride cycling in AB_2 and AB_5 MH alloys [76, 92, 126, 127]. The hystereses measured at 60 °C in this study are in general larger than those from typical AB_2 and AB_5 MH alloys, which is an indication of a higher pulverization rate during hydride/dehydride cycling. The average electron density calculated based on the numbers of outer-shell electrons of constituent elements has been shown to have a

strong correlation to the PCT hysteresis in the as-cast AB_2 alloy system [76, 126, 127]. In this study, R^2 between the PCT hysteresis at 60 °C before annealing and the number of outer-shell electrons of the supplemental element is 0.36, which indicates the existence of some correlation. The more electrons in the outer shell of the supplemental element, the larger hysteresis the alloy has. The correlation between the PCT hysteresis after annealing and the number of outer-shell electron is nonexistent ($R^2 = 0.00$).

Both ΔH and ΔS were calculated based on the 60 and 90 °C absorption isotherms by the equation (3.1). The obtained ΔH, or heats of hydride formation, are in a narrow range of –46 to –33 kJ mol^{-1} H_2, which is considered to be on the higher side of the acceptable value for room temperature Ni/MH battery applications [3-5]. The deviation from ΔS between hydrogen in the alloy and free hydrogen molecules in gaseous form (–130 J K^{-1} mol^{-1} H_2) [128] in most of the alloys is due to the incomplete hydriding, which causes extra entropy from a less-ordered hydrogen distribution in the alloy.

5.2.2 Electrochemical measurement

Half-cell capacity measurements were conducted at discharge rates of 50, 12, and 4 mA g^{-1}. The high-rate discharge capacities (capacities measured at 50 mA g^{-1}) and the full discharge capacities (sum of capacities measured at 50, 12, and 4 mA g^{-1} for each cycle, which is the same as if the capacity is measured at 4 mA g^{-1}) of the first 11 cycles of base alloys ZN-Ni and ZN-NiA are plotted in Figure 5.7. The activation of these alloys without any pre-etching process is considered fast when compared to AB_2 alloy before composition modification, especially for being Ti-free (Ti is known to facilitate activation [129]).

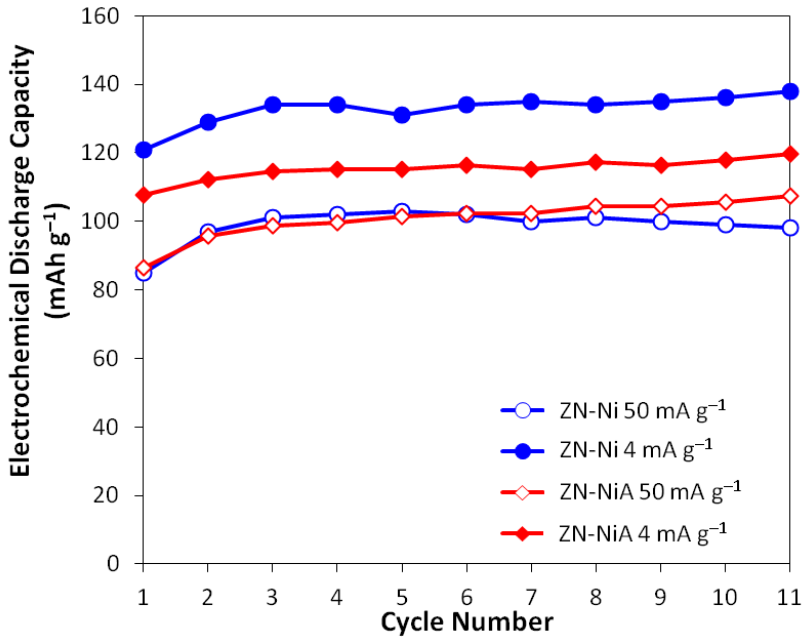

Figure 5.7 Half-cell capacities of alloys ZN-Ni and ZN-NiA measured at two different discharge rates, 50 and 4 mA g^{-1} (high-rate and full discharge capacities, respectively).

The high-rate discharge capacity and the full discharge capacity for each sample are listed in Table 5.2. The full discharge capacities of each sample before and after annealing are plotted in Figure 5.8. After annealing, the full discharge capacity drops from 136 mAh g^{-1} to 118 mAh g^{-1} in the base alloy. Compared to the result given by Ruiz et al. [7, 12], which is 91 mAh g^{-1} measured at 53 mA g^{-1} for Zr_8Ni_{21} annealed at 1000 °C for 30 days, the high-rate discharge capacity of 106 mAh g^{-1} obtained from ZN-NiA at 50 mA g^{-1} is comparatively higher. Similar to the effect of various modifiers' metallic sizes on maximum gaseous phase hydrogen storage capacity, La and Hf are beneficial to the full discharge capacity while V, Mn, Co, and Sn deteriorate it. The highest full discharge capacity, 200 mAh g^{-1}, was obtained from ZN-Hf. Moreover, the trend in full discharge capacity according to the main phase also follows the evolution in B/A ratio: alloys with Zr_7Ni_{10} (o) main phase have the highest capacities while those with Zr_2Ni_7 main phase show the lowest capacities. Unlike the observations made in maximum

gaseous phase hydrogen storage capacity, all alloys except for Sn-substitution that shows alternation in main phase demonstrate degradation in full discharge capacity after annealing. The synergetic effects between the main and secondary phases seem to be crucial to the full discharge capacity as reported previously [15, 20, 53, 54] and appear to be more influential in the electrochemical environment than in the gaseous phase.

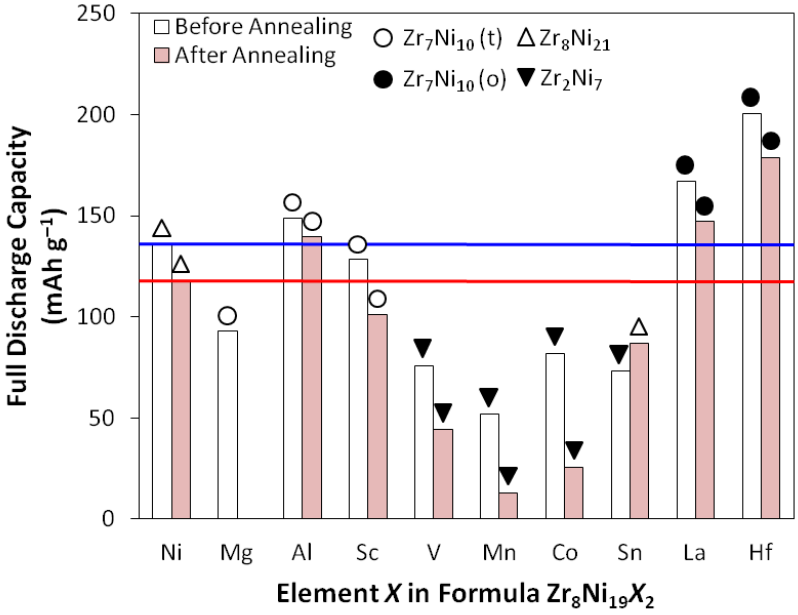

Figure 5.8 Full half-cell discharge capacities measured at a discharge current of 4 mA g^{-1} for all alloys in this study. Horizontal lines mark the capacities from the base alloy ZN-Ni for easy comparison. Symbol on top of the data bar shows the main phase of the specific alloy.

Table 5.2 Summary of room temperature electrochemical half-cell measurements. Number of activation cycles is the cycle number when 95% of the 50 mA g^{-1} capacity is reached.

	High-rate discharge capacity (mAh g^{-1})	**Full discharge capacity (mAh g^{-1})**	**HRD**	**Number of activation cycles**	**OCV (V)**	I_0 **(mA g^{-1})**	D **(× 10^{-10} cm^2 s^{-1})**
ZN-Ni	99	136	0.73	2	–0.87	7.7	2.09
ZN-NiA	106	118	0.90	4	–0.90	19.9	3.18
ZN-Mg	66	93	0.71	8	–0.88	28.3	1.74
ZN-Al	105	149	0.70	5	–0.91	20.9	1.96
ZN-AlA	100	140	0.72	7	–0.86	16.2	2.35
ZN-Sc	87	129	0.68	7	–0.87	31.1	1.62
ZN-ScA	59	101	0.58	10	–0.87	20.2	1.58
ZN-V	64	76	0.84	8	–0.92	21.6	2.24
ZN-VA	40	44	0.89	3	–0.93	9.4	4.22
ZN-Mn	36	52	0.69	7	–0.90	13.7	1.79
ZN-MnA	11	13	0.84	8	–0.90	4.1	2.41
ZN-Co	40	82	0.49	2	–0.85	13.7	1.36
ZN-CoA	19	26	0.74	3	–0.86	4.3	3.17
ZN-Sn	61	73	0.84	5	–0.93	17.9	2.25
ZN-SnA	82	87	0.95	6	–0.93	14.1	3.87

ZN-La	128	167	0.77	3	–0.87	16.1	1.80
ZN-LaA	112	147	0.76	3	–0.90	22.1	2.57
ZN-Hf	159	200	0.79	7	–0.86	13.9	1.71
ZN-HfA	124	179	0.69	7	–0.90	21.2	1.84

The half-cell HRD, defined as the ratio between the high-rate and full discharge capacities, for each sample is listed in Table 5.2 and plotted in Figure 5.9. Supplements such as V, Sn, La, and Hf improve HRD compared to the base alloy ZN-Ni. After annealing, most of the HRD values increase except for alloys with Zr_7Ni_{10} (o) or Zr_7Ni_{10} (t) main phase. The improvement in HRD is related to the larger grain size as a result of the annealing treatment, which facilitates the bulk hydrogen diffusion discussed later in this section. Alloys with Zr_7Ni_{10} (o) or Zr_7Ni_{10} (t) main phase exhibit lower HRD compared to before annealing as a consequence of the increase in abundance of the B-poor main phase. The HRD values before and after annealing were correlated to the oxidation potential (Table 4.1) and R^2 increases from 0.01 to 0.41. As the oxidation potential decreases (easily oxidized), the surface reaction is impeded by the oxide of the supplemental element, and thus the HRD value decreases. The difference in correlation strengths before and after annealing is due to the number of phases that exist in the alloy: after annealing, the secondary phases are reduced and eliminated, therefore the correlation according to the oxidation potential is more significant than in the case of before annealing, where the dispersion of the constituent elements in various phases may mask the influence of the designed overall compositions.

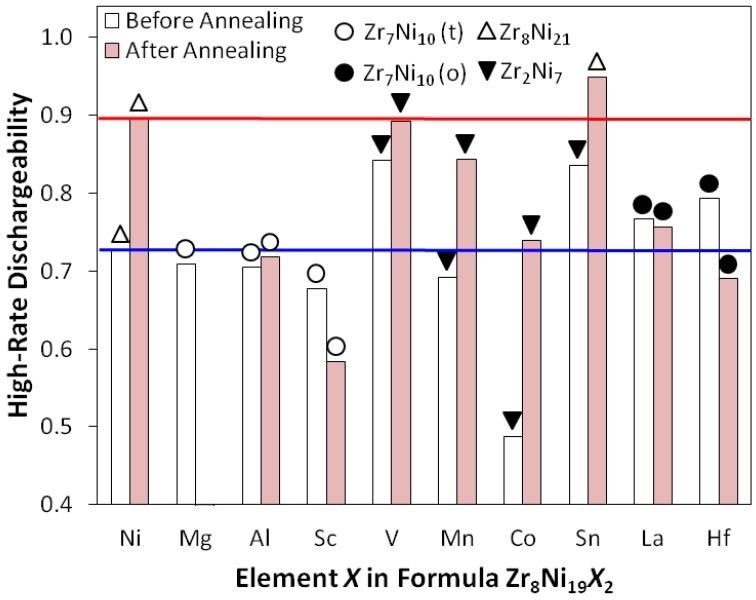

Figure 5.9 High-rate dischargeabilities for all alloys in this study. Horizontal lines mark the capacities from the base alloy ZN-Ni for easy comparison. Symbol on top of the data bar shows the main phase of the specific alloy.

The number of activation cycles, defined as the cycle number when 95% of the high-rate discharge capacity is reached, for each sample is listed in Table 5.2. Before annealing, all supplements besides Co impede the formation performance. Except for V-substitution, all other supplements show decreases in formation performance after annealing, perhaps due to unintentional oxidation during annealing.

The open-circuit voltage (OCV) measured at the 50% state-of-charge for each alloy is listed in Table 5.2. Supplements such as Mg, Al, V, Mn, and Sn lower the OCV value and therefore contribute to higher cell voltage, which indicates better power performance in sealed battery configuration. OCV is correlated to the absorption plateau pressure by the Nernst equation [93, 109, 112]

$$\textbf{OCV vs. Hg/HgO} = -0.934 - 0.0291 \log P_{H2} \qquad (5.2)$$

As the plateau pressure increases, the OCV value decreases. Since the trend in plateau pressure is not clear, as shown in Figure 5.6, an alternative correlation method is applied: the maximum gaseous phase hydrogen storage capacity is closely related to the plateau pressure. A lower maximum gaseous phase hydrogen storage capacity implies a higher plateau pressure (lower metal-hydrogen bond strength). In general, the aforementioned substitutions that show lower OCV values also have lower maximum gaseous phase hydrogen storage capacities compared to the base alloy. The exception of Al-substitution may be caused by the differences between the gaseous phase and the electrochemical environment. After annealing, the OCV values either remain the same or are reduced except for Al-substitution.

The surface reaction exchange current (I_0) and the bulk hydrogen diffusion coefficient (D), two dominating factors in determining HRD [110, 130-132], for each alloy are listed in Table 5.2. All supplements improve I_0 compared to the base alloy ZN-Ni. Mg and Sc supplements show the highest I_0 values before annealing. Only the base alloy and La- and Hf-substitutions have better I_0 values after annealing. The D values decrease with most of the supplements except for V and Sn. After annealing, except for Sc, the D values improve in all other substitutions. Therefore, by enlarging the domain of the main phase grain through the annealing process, the hydrogen diffusion in the bulk improves. These I_0 and D values of the Zr_8Ni_{21} alloy system are considerably lower than those from optimized AB_2 (32.1 mA $g^{-1}$and 9.7 $\times 10^{-10}$ cm^2 s^{-1}), AB_5 (43.2 mA g^{-1} and 25.5 $\times 10^{-10}$ cm^2 s^{-1}), and A_2B_7 (41.0 mA g^{-1} and 30.8 $\times 10^{-10}$ cm^2 s^{-1}) alloys [105]. Further modifying element and phase selections are required in order to utilize the Zr_8Ni_{21} alloy system in commercial applications.

The R^2 values of fitting HRD into linear relationships with I_0 and D are 0.04, and 0.55, respectively. The strong dependence of HRD on D is shown in Figure 5.10. In other words, in the Zr_8Ni_{21} alloy family, the HRD is more related to the bulk transport than the surface reaction.

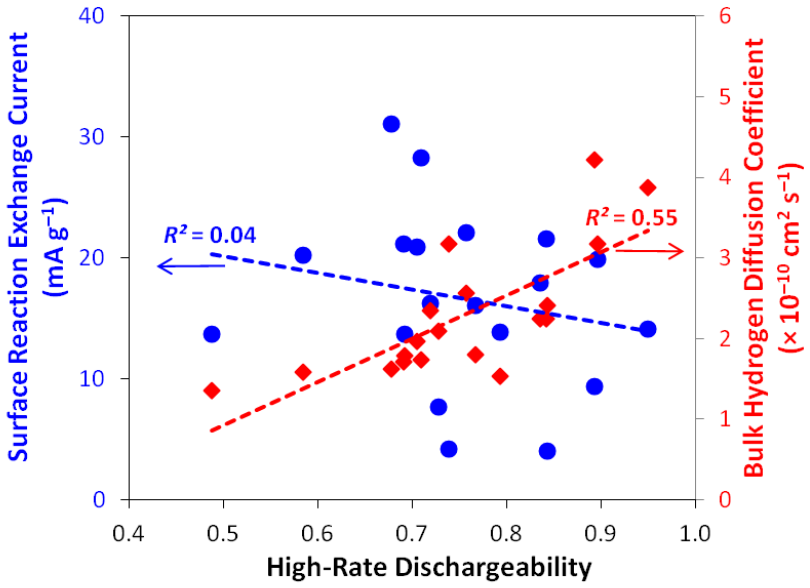

Figure 5.10 Correlations between the half-cell high-rate dischargeability and both the surface reaction exchange current and the bulk hydrogen diffusion coefficient

5.2.3 Correlations between the gaseous phase hydrogen storage and electrochemical characteristics

It is always interesting to compare the gaseous phase hydrogen storage and electrochemical characteristics of MH alloys. In the past, the general rule of thumb is that the electrochemical discharge capacity is between the maximum and reversible gaseous phase hydrogen storage capacities [93, 95]. During electrode formation/activation, two possible reactions can occur and result in higher electrochemical discharge capacity than the reversible gaseous phase hydrogen storage capacity: preferential oxidation and/or etching. As a result of

preferential oxidation, new phases form, such as metallic Ni in the surface oxide, and act as catalysts in assisting the difficult hydrogen desorption of some phases in the gaseous phase discharge electrochemically. Furthermore, preferential etching exposes some minor phases that are originally buried in the bulk and therefore not effective in the gaseous phase. However, since it's difficult to fully discharge in some phases due to their extremely slow discharge kinetics , the electrochemical discharge capacity is always less than or barely equal to the maximum gaseous phase hydrogen storage. In Figure 5.11, both the maximum and reversible gaseous phase hydrogen storage capacities are plotted against the full electrochemical discharge capacity. The former shows a very significant correlation (R^2 = 0.91), and the latter also has also a relatively weaker correlation (R^2 = 0.42).

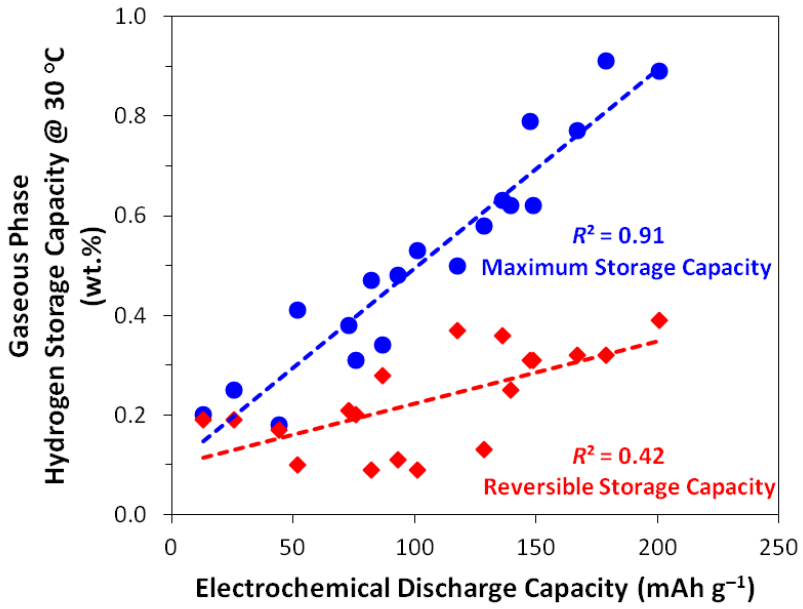

Figure 5.11 Correlations between the gaseous phase hydrogen storage capacities and electrochemical capacity. The maximum gaseous phase hydrogen storage capacity correlates well with the electrochemical capacity (R^2 = 0.91).

The gaseous phase hydrogen storage capacities in wt.% were converted to their equivalent electrochemical capacities using the conversion factor

$$\textbf{1 wt.\% of } H_2 \textbf{ = 268 mAh } g^{-1} \qquad \textbf{(5.3)}$$

As seen in Figure 5.12, in all the cases except for the ones with very low capacities, the electrochemical discharge capacity falls between the maximum and reversible gaseous phase hydrogen storage capacities.

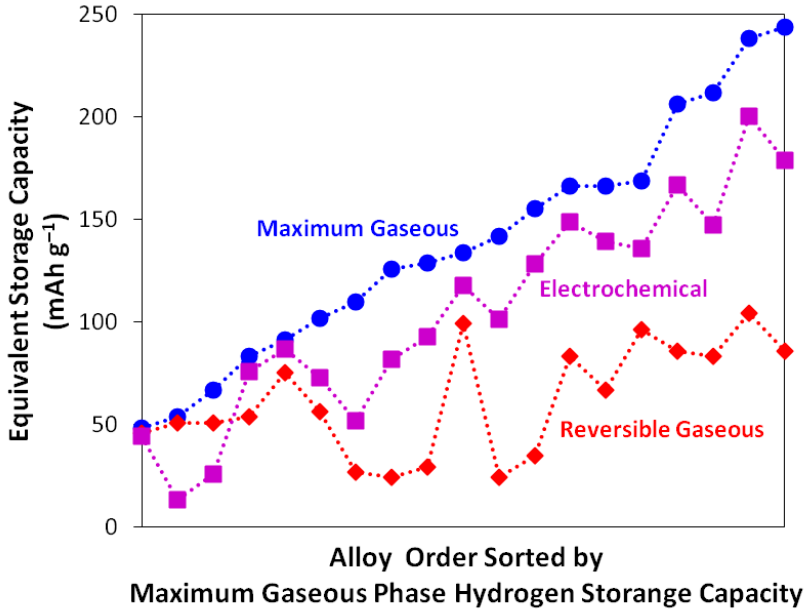

Figure 5.12 Comparison among the maximum gaseous phase hydrogen storage capacity, the reversible gaseous phase hydrogen storage capacity, and the full electrochemical discharge capacity.

5.3 Summary

The general effects of annealing on the Zr_8Ni_{21} alloy system in this study are summarized as follows:

- An increase in the maximum gaseous phase hydrogen storage capacity for alloys with Zr_7Ni_{10} (t) main phase, which have the highest capacity before annealing;
- A decrease in the plateau pressure for alloys with Zr_7Ni_{10} (o) or Zr_7Ni_{10} (t) main phase;
- A decrease in the full electrochemical discharge capacity;
- An increase in HRD for alloys with Zr_8Ni_{21} or Zr_2Ni_7 main phase;
- An increase in surface reaction exchange current for alloys with Zr_8Ni_{21} of Zr_7Ni_{10} (o) main phase; and
- An increase in bulk diffusion coefficient.

The effect of each supplemental element on various storage properties is arranged in the order from the most adverse to the most beneficial (with *Ni* being the base alloy ZN-Ni):

Gaseous phase hydrogen storage:

(As-cast)

Maximum storage capacity– V, Sn, Mn, Co, Mg, Sc, Al, *Ni*, La, Hf

Reversible storage capacity– Co, Mn, Mg, Sc, V, Sn, Al, La, *Ni*, Hf

(After annealing)

Maximum storage capacity– V, Mn, Co, Sn, *Ni*, Sc, Al, La, Hf

Reversible storage capacity– Sc, V, (Mn, Co), Al, Sn, La, Hf, *Ni*

Electrochemical properties:

(As-cast)

Full discharge capacity– Mn, Sn, V, Co, Mg, Sc, *Ni*, Al, La, Hf

HRD– Co, Sc, Mn, Al, Mg, *Ni*, La, Hf, (V, Sn)

Activation– (Mg, V), (Sc, Mn, Hf), (Al, Sn), La, (*Ni*, Co)

Surface reaction exchange current –	*Ni*, (Mn, Co), Hf, La, Sn, Al, V, Mg, Sc
Bulk diffusion coefficient –	Co, Sc, Hf, Mg, Mn, La, Al, *Ni*, V, Sn
(After annealing)	
Full discharge capacity–	Mn, Co, V, Sn, Sc, *Ni*, Al, La, Hf
HRD–	Sc, Hf, Al, Co, La, Mn, V, *Ni*, Sn
Activation–	Sc, Mn, (Al, Hf), Sn, *Ni*, (V, Co, La)
Surface reaction exchange current –	Mn, Co, V, Sn, Al, *Ni*, Sc, Hf, La
Bulk diffusion coefficient –	Sc, Hf, Al, Mn, La, Co, *Ni*, Sn, V

In conclusion, as a result of its larger metallic size and the ability to alter the main phase to Zr_7Ni_{10} (o) due to its number of outer-shell electrons, the as-cast Hf-substitution ($Zr_8Ni_{19}Hf_2$ alloy) demonstrates the best overall gaseous phase hydrogen storage and electrochemical properties among all alloys in this study.

CHAPTER 6

CONCLUSION

6.1 Conclusion

Compared to the mish metal-based AB_5 MH alloy commonly used in Ni/MH batteries, the transition metal-based AB_2 MH alloy not only reduces the rare earth dependency issue, it also has higher specific energy and therefore offers an opportunity to catch up with the rival lithium-ion battery technology. In order to further improve the overall performance of AB_2 MH alloy, it's crucial to obtain more detailed understanding about its multi-phase nature, which includes the main C14/C15 Laves phases and the secondary non-Laves phases.

For the purpose of optimizing the gaseous phase and electrochemical advantages of both the C14 and C15 Laves phases in AB_2 MH alloys, a systematic study was established to predict and understand the factors that affect the C14/C15 phase abundance. *e*/*a* was proven to be one of the most influential parameters in determining the C14/C15 phase abundance: as *e*/*a* increased, C14/C15 became less/more dominant, respectively. However, with different A-site compositions but same overall *e*/*a*, a shift in *e*/*a* was observed in the C14/C15 phase abundance vs. *e*/*a* relationship. The average atomic radius of A atoms was shown to correlate very well with the C14/C15 threshold when the choice of A-site elements is limited to any of Ti + Zr combinations (pure or mixed). The average chemical potential for electronic charge of A atoms had a nearly perfect linear correlation to the C14/C15 threshold even with the addition of Hf in the selection of A-site elements. The combination of *e*/*a* and the average chemical potential for electronic charge can be used to predict the C14/C15 phase abundance and assist future AB_2 MH alloy design process.

A thorough study of four important non-Laves phase alloys, Zr_8Ni_{21}, Zr_7Ni_{10}, Zr_9Ni_{11}, and ZrNi, commonly seen in AB_2 MH alloys were presented. In order to investigate the synergetic effect between the major and secondary phases, annealing treatment was adopted on each alloy to change the abundances of various phases. The structure, gaseous phase hydrogen storage, and electrochemical properties were obtained for each of the four alloy compositions before and after annealing and correlated with each other. Annealing generally suppressed secondary phases except for the case of Zr_9Ni_{11}, where its secondary ZrNi phase increased. As the Zr/Ni ratio in the average composition increased, the maximum gaseous phase hydrogen storage capacity increased but maximized at Zr : Ni = 9 : 11. Comparing the properties before and after annealing, it was clear that the natures of constituent phases influenced the gaseous phase storage. During the electrochemical measurement, it was found that the highest full discharge capacity was obtained at Zr : Ni = 7 : 10, which is a compromise between the hydrogen desorption/discharge rate and the theoretical maximum gaseous phase hydrogen storage. As the Zr/Ni ratio increased, the amount of metallic Ni in the surface oxide obtained by magnetic susceptibility measurement decreased, and consequently HRD decreased, which followed the decreasing trend of the amount of metallic Ni in the surface oxide obtained by magnetic susceptibility measurement. Among all alloys before and after annealing, the unannealed Zr_7Ni_{10} demonstrated the best overall gaseous phase hydrogen storage and electrochemical capacity and can be a candidate to replace AB_5 and AB_2 MH alloys in Ni/MH battery applications. Furthermore, the unannealed Zr_8Ni_{21} showed a good balance between HRD and ease of formation.

From the comparison of non-Laves phase alloys, Zr_8Ni_{21} MH alloy was chosen based on its promising performance to be further modified for the purposes of gaining better

understanding of Zr_8Ni_{21} MH alloy family and developing alternative MH alloys suitable for Ni/MH battery applications. 10 $Zr_8Ni_{19}X_2$ alloys, where X = Ni, Mg, Al, Sc, V, Mn, Co, Sn, La, and Hf, were prepared and studied. The effect of annealing on these alloys except for the Mg-substitution was also investigated. Only the main phase of the annealed Sn-substitution remained Zr_8Ni_{21}-structured while those of other substitutions turned into Zr_7Ni_{10} or Zr_2Ni_7. Similar to the preference of C14/C15 main phase in AB_2 alloys, the number of outer-shell electrons played an important role in determining the main phase of the A_8B_{21} alloys. As the number of outer-shell electrons of the substituting element increased, the main phase evolved from tetragonal Zr_7Ni_{10} (Mg, Al, and Sc), to orthorhombic Zr_7Ni_{10} (La and Hf), cubic Zr_2Ni_7 (V, Mn, Co, and Sn (before annealing)), and finally triclinic Zr_8Ni_{21} (Ni and Sn (after annealing)). After annealing, the abundance of the predominant phase increased, and the number of secondary phases diminished. The only exception was the Sn-substituted alloy, where the major phase transformed from Zr_2Ni_7 to Zr_8Ni_{21} (after annealing). The observed trend in maximum gaseous phase hydrogen storage capacity followed the increasing order of B/A ratio of the main phase as orthogonal Zr_7Ni_{10} > tetragonal Zr_7Ni_{10} > Zr_8Ni_{21} > Zr_2Ni_7. After annealing, due to the increase in abundance of the main phase, the maximum gaseous phase hydrogen storage capacities of alloys with higher capacities before annealing increased while others decreased. The full discharge capacity also improved in the same increasing order of B/A ratio in the main phase. Hf-substitution showed the highest electrochemical discharge capacity at 200 mAh g^{-1}. After annealing, all alloys with the same main phase as the as-cast alloys showed degradation in full electrochemical capacity due to the reduction in both number and abundance of the catalytic secondary phases. All supplements assisted in improving surface exchange current from the base binary Zr_8Ni_{21} alloy. Except for La- and Hf-substitutions, annealing reduced the surface

exchange current density. The bulk hydrogen diffusion coefficient decreased with most of the supplements except for V- and Sn-substitutions. All supplements, except for Sc, showed improvement in the bulk diffusion after annealing. Furthermore, the maximum gaseous phase hydrogen storage capacity showed a strong correlation to the full electrochemical discharge capacity. Among all alloys in this study, the as-cast Hf-substituted Zr_8Ni_{21} alloy demonstrated the best overall gaseous phase hydrogen storage and electrochemical properties.

6.2 Future work

Investigation on the determining factors of non-Laves secondary phase abundances in AB_2 MH alloys will be the next interesting topic to be explored. This study will be done by examining the secondary phase abundances with various elemental substitutions in AB_2 formulation. With information on the formations of C14/C15 Laves phases and non-Laves secondary phases, the phase abundances in a certain AB_2 MH alloy can be more precisely predicted at the alloy design stage.

In order to further improve the ternary Zr_8Ni_{21} MH alloy family to be better suited for Ni/MH battery applications, formula optimization through additional compositional modifications will be required. Moreover, investigation on structural characteristics, gaseous phase hydrogen storage, and electrochemical properties of other Zr-Ni binary alloys such as $ZrNi_3$, Zr_2Ni_7, and $ZrNi_5$ (transition metal-based AB_5 alloy) is fascinating for the purpose of developing more potential MH alloys.

REFERENCES

[1] Fetcenko MA, Ovshinsky SR, Young K, Reichman B, Fierro C, Koch J, et al. High catalytic activity disordered VTiZrNiCrCoMnAlSn hydrogen storage alloys for nickel-metal hydride batteries. J Alloys Compd 2002;330-332:752-9.

[2] Fetcenko MA, Ovshinsky SR, Reichman B, Young K, Fierro C, Koch J, et al. Recent advances in NiMH battery technology. J Power Sources 2007;165:544-51.

[3] Ovshinsky SR, Fetcenko MA, Ross J. A nickel metal hydride battery for electric vehicles. Science 1993;260:176-81.

[4] Nakano H, Wakao S, Shimizu T, Morii K. Development of C14-type Laves phase alloy for high-rate battery application. J Electrochem Soc Jpn 1998;66:734-9.

[5] Hong K. The development of hydrogen storage alloys and the progress of nickel hydride batteries. J Alloys Compd 2001;321:307-13.

[6] Osumi Y. Suiso-kyuzo-goukin no Syurui to Sono. New ed. Agune Technology Center: Tokyo; 1999.

[7] News article available online: http://www.technewsdaily.com/us-congress-pushes-independence-from-chinese-rare-earth-suppliers-0325/, Access on 02-20-2012.

[8] News article available online: http://news.nationalgeographic.com/news/2010/10/101001-energy-rare-earth-metals/, Access on 02-20-2012.

[9] News article available online: http://www.bloomberg.com/news/2011-06-17/rare-earth-prices-double-on-china-industrial-minerals.html, Accessed on 02-20-2012.

[10] Young K, Fetcenko MA, Koch J, Morii K, Shimizu T. Studies of Sn, Co, Al, and Fe additives in C14/C15 Laves alloys for NiMH battery application by orthogonal arrays. J Alloys Compd 2009;486:559-69.

[11] Yu JY, Lei YQ, Chen CP, Wu J, Wang QD. The electrochemical properties of hydrogen storage Zr-based Laves phase alloys. J Alloys Compd 1995;231:578-81.

[12] Joubert JM, Latroche M, Percheron-Guégan A, Bouet J. Improvement of the electrochemical activity of Zr-Ni-Cr Laves phase hydride electrodes by secondary phase precipitation. J Alloys Compd 1996;240:219-28.

[13] Joubert JM, Sun D, Latroche M, Percheron-Guégan A. Electrochemical performances of ZrM_2 (M=V, Cr, Mn, Ni) Laves phases and the relation to microstructures and thermodynamical properties. J Alloys Compd 1997;253-254:564-9.

[14] Zhang QA, Lei YQ, Yang XG, Ren K, Wang QD. Annealing treatment of AB_2-type hydrogen storage alloys: I. crystal structures. J Alloys Compd 1999;292:236-40.

[15] Zhang WK, Ma CA, Yang XG, Lei YQ, Wang QD, Lu GL. Influences of annealing heat treatment on phase structure and electrochemical properties of $Zr(MnVNi)_2$ hydrogen storage alloys. J Alloys Compd 1999;293-295:691-7.

[16] Zhang WK, Ma CA, Huang H, Yang XG, Lei YQ, Wang QD, et al. Crystal structures of the Zr-Ni phases in the Zr-Mn-Ni Laves phase hydrogen storage alloys. Rare Met Mater Eng 1999;28:202-5.

[17] Bououdina M, Soubeyroux JL, Fruchart D. Study of the hydrogenation/dehydrogenation processes of $ZrCr_{0.7}Ni_{1.3}$, a Laves phase-rich multi-component system, by in-situ neutron diffraction under hydrogen gas pressure. J Alloys Compd 2001;327:185-94.

[18] Zhang WK, Ma CA, Huang H, Yang XG, Tu JP, Lei YQ. Occurrence and crystal structure of Zr-Ni phases in the Zr-Mn-V-Ni Laves phase hydrogen storage electrode alloys. Rare Met Mater Eng 2001;30:194-7.

[19] Sun JC, Li S, Ji SJ. Phase composition and electrochemical performances of the $Zr_{1-x}Ti_xCr_{0.4}Mn_{0.2}V_{0.1}Ni_{1.3}$ alloys with $0.1 \leq x \leq 0.3$. J Alloys Compd 2005;404-406:687-90.

[20] Visintin A, Peretti HA, Ruiz F, Corso HL, Triaca WE. Effect of additional catalytic phases imposed by sintering on the hydrogen absorption behavior of AB_2 type Zr-based alloys. J Alloys Compd 2007;428:244-51.

[21] Young K, Fetcenko MA, Li F, Ouchi T, Koch J. Effect of vanadium substitution in C14 Laves phase alloys for NiMH battery application. J Alloys Compd 2009;468:482-92.

[22] Young K, Ouchi T, Fetcenko MA. Roles of Ni, Cr, Mn, Sn, Co, and Al in C14 Laves phase alloys for NiMH battery application. J Alloys Compd 2009;476:774-81.

[23] Young K, Ouchi T, Huang B, Chao B, Fetcenko MA, Bendersky LA, et al. The correlation of C14/C15 phase abundance and electrochemical properties in the AB_2 alloys. J Alloys Compd 2010;506:841-8.

[24] Boettinger WJ, Newbury DE, Wang K, Bendersky LA, Chiu C, Kattner UR, et al. Examination of multiphase $(Zr,Ti)(V,Cr,Mn,Ni)_2$ Ni-MH electrode alloys: Part I. Dendritic solidification structure. Metall Mater Trans A 2010;41:2033-47.

[25] Bendersky L, Wang K, Boettinger W, Newbury D, Young K, Chao B. Examination of multiphase $(Zr,Ti)(V,Cr,Mn,Ni)_2$ Ni-MH electrode alloys: Part II. Solid-state transformation of the interdendritic B2 phase. Metall Mater Trans A 2010;41:1891-906.

[26] Young K, Nei J, Ouchi T, Fetcenko MA. Phase abundances in AB_2 metal hydride alloys and their correlations to various properties. J Alloys Compd 2011;509:2277-84.

[27] Young K, Ouchi T, Koch J, Fetcenko MA. Compositional optimization of vanadium-free hypo-stoichiometric AB_2 metal hydride alloy for Ni/MH battery application. J Alloys Compd 2012;510:97-106.

[28] Young K, Ouchi T, Huang B, Fetcenko MA. Effects of B, Fe, Gd, Mg, and C on the structure, hydrogen storage, and electrochemical properties of vanadium-free AB_2 metal hydride alloy. J Alloys Compd 2012;511:242-50.

[29] Young K, Ouchi T, Huang B, Reichman B, Fetcenko MA. Studies of copper as a modifier in C14-predominant AB_2 metal hydride alloys. J Power Sources 2012;204:205-12.

[30] Laves F. Theory of alloy phases. ASM: Cleveland; 1956.

[31] Massalski TB. Structure and stability of alloys. In: Cahn RW, Hassen P, editors. Physical metallurgy, Amsterdam: Elsevier; 1996. p. 135-204.

[32] Thoma DJ, Perepezko JH. An experimental evaluation of the phase relationships and solubilities in the Nb-Cr system. Mater Sci Eng A 1992;156:97-108.

[33] Hong S, Fu CL. Phase stability and elastic moduli of Cr_2Nb by first-principles calculations. Intermetallics 1999;7:5-9.

[34] Song XY, Zhang XB, Lei YQ, Zhang Z, Wang QD. Effect of microstructure on the properties of Zr-Mn-V-Ni AB_2 type hydride electrode alloys. Int J Hydrogen Energy 1999;24:455-9.

[35] Yang XG, Zhang WK, Lei YQ, Wang QD. Electrochemical properties of Zr-V-Ni system hydrogen storage alloys. J Electrochem Soc 1999;146:1245-50.

[36] Stein F, Palm M, Sauthoff G. Structure and stability of Laves phases. Part I. Critical assessment of factors controlling Laves phase stability. Intermetallics 2004;12:713-20.

[37] Laves F, Witte H. Die Kristallstruktur des $MgNi_2$ und seine Beziehung zu den Typen des $MgCu_2$ und $MgZn_2$. Metallwirtsch Metallwiss Metalltech 1935;14:645-9.

[38] Laves F, Witte H. Der Einfluß der Valenzelektronen auf die Kristallstruktur ternärer Magnesium-Legierungen. Metallwirtsch Metallwiss Metalltech 1936;15:840-2.

[39] Johnston RL, Hoffmann R. Structure-bonding relationships in the Laves phases. Z Anorg Allg Chem 1992;616:105-20.

[40] Zhu JH, Liaw PK, Liu CT. Effect of electron concentration on the phase stability of $NbCr_2$-based Laves phase alloys. Mater Sci Eng A 1997;239-240:260-4.

[41] Zhu JH, Liu CT, Liaw PK. Phase stability and mechanical behavior of $NbCr_2$-based Laves phases. Intermetallics 1999;7:1011-6.

[42] Berry RL, Raynor GV. The crystal chemistry of the Laves phases. Acta Crystallogr 1953;6:178-86.

[43] Dwight AE. Factors controlling the occurrence of Laves phases and AB_5 compounds among transition elements. Trans Am Soc Met 1961;53:479-500.

[44] Nevitt MV. Alloy chemistry of trasition elements. In: Beck PA, editor. Electronic structure and alloy chemistry of the transition elements, New York: Interscience Publishers; 1963. p. 101-78.

[45] Zhu J, Liu C, Pike L, Liaw P. A thermodynamic interpretation of the size-ratio limits for Laves phase formation. Metall Mater Trans A 1999;30:1449-52.

[46] Zhu JH, Liu CT, Pike LM, Liaw PK. Enthalpies of formation of binary Laves phases. Intermetallics 2002;10:579-95.

[47] Thoma DJ, Perepezko JH. A geometric analysis of solubility ranges in Laves phases. J Alloys Compd 1995;224:330-41.

[48] Edwards A. The lattice dimensions of the AB_2 Laves phases. Metall Mater Trans B 1972;3:1365-72.

[49] Huot J, Akiba E, Ishido Y. Crystal structure of multiphase alloys $(Zr,Ti)(Mn,V)_2$. J Alloys Compd 1995;231:85-9.

[50] Yoshida M, Akiba E. Hydrogen absorbing-desorbing properties and crystal structure of the Zr-Ti-Ni-Mn-V AB_2 Laves phase alloys. J Alloys Compd 1995;224:121-6.

[51] Bououdina M, Enoki H, Akiba E. The investigation of the $Zr_{1-y}Ti_y(Cr_{1-x}Ni_x)_2$-$H_2$ system $0.0 \leq y \leq 1.0$ and $0.0 \leq x \leq 1.0$ Phase composition analysis and thermodynamic properties. J Alloys Compd 1998;281:290-300.

[52] Shu K, Zhang S, Lei Y, Lü G, Wang Q. Effect of Ti on the structure and electrochemical performance of Zr-based AB_2 alloys for nickel-metal rechargeable batteries. J Alloys Compd 2003;349:237-41.

[53] Zhang QA, Lei YQ, Yang XG, Ren K, Wang QD. Annealing treatment of AB_2-type hydrogen storage alloys: II. Electrochemical properties. J Alloys Compd 1999;292:241-6.

[54] Bououdina M, Lenain C, Aymard L, Soubeyroux JL, Fruchart D. The effects of heat treatments on the microstructure and electrochemical properties of the $ZrCr_{0.7}Ni_{1.3}$ multiphase alloy. J Alloys Compd 2001;327:178-84.

[55] Ruiz FC, Peretti HA, Visintin A, Real SG, Castro EB, Corso HL, et al. Effect of thermal treatment on the electrochemical hydrogen absorption of ZrCrNi alloy. J New Mater Electrochem Syst 2007;10:249-54.

[56] Ruiz FC, Castro EB, Real SG, Peretti HA, Visintin A, Triaca WE. Electrochemical characterization of AB_2 alloys used for negative electrodes in Ni/MH batteries. Int J Hydrogen Energy 2008;33:3576-80.

[57] Okamoto H. Ni-Zr (nickel-zirconium). J Phase Equilib Diffus 2007;28:409.

[58] Joubert JM, Latroche M, Percheron-Guégan A. Hydrogen absorption properties of several intermetallic compounds of the Zr-Ni system. J Alloys Compd 1995;231:494-7.

[59] Ruiz FC, Castro EB, Peretti HA, Visintin A. Study of the different Zr_xNi_y phases of Zr-based AB_2 materials. Int J Hydrogen Energy 2010;35:9879-87.

[60] Spit F, H.M., Drijver J, W., Turkenburg W, C., Radelaar S. Hydrogen sorption by some early-late transition metal glasses. J Phys Colloq 1980;41:C8-890-3.

[61] Spit FHM, Drijver JW, Radelaar S. Hydrogen sorption by the metallic glass $Ni_{64}Zr_{36}$ and by related crystalline compounds. Scr Metall 1980;14:1071-6.

[62] Wakao S, Sawa H, Nakano H, Chubachi S, Abe M. Capacities and durabilities of Ti-Zr-Ni alloy hydride electrodes and effects of electroless plating on their performances. J Less Common Met 1987;131:311-9.

[63] Sawa H, Ohta M, Nakano H, Wakao S. Effects of oxidation treatment of Ti-Zr-Ni hydride electrodes containing Zr_7Ni_{10} phase on their electrochemical properties. Z Phys Chem 1989;164:1527-32.

[64] Varga LK, Lovas A, Tompa K, Latroche M, Percheron-Guegan A. Electrochemical pressure-composition isotherms for amorphous $Ni_{1-x}Zr_x$ alloys. J Alloys Compd 1995;231:321-4.

[65] Takeshita HT, Kiyobayashi T, Tanaka H, Kuriyama N, Haruta M. Reversible hydrogen absorption and desorption achieved by irreversible phase transition. J Alloys Compd 2000;311:L1-4.

[66] Takeshita HT, Fujiwara N, Oishi T, Noréus D, Takeichi N, Kuriyama N. Another unusual phenomenon for Zr_7Ni_{10}: structural change in hydrogen solid solution and its conditions. J Alloys Compd 2003;360:250-5.

[67] Takeshita HT, Kondo S, Miyamura H, Takeichi N, Kuriyama N, Oishi T. Re-examination of Zr_7Ni_{10} single-phase region. J Alloys Compd 2004;376:268-74.

[68] Takeshita HT, Fujiwara N, Takeichi N, Senoh H, Oishi T. Hydrogenation properties and structural change of $Hf_xZr_{7-x}Ni_{10}$ (x = 0-7). J Alloys Compd 2005;404-406:609-12.

[69] Young K, Ouchi T, Liu Y, Reichman B, Mays W, Fetcenko MA. Structural and electrochemical properties of $Ti_xZr_{7-x}Ni_{10}$. J Alloys Compd 2009;480:521-8.

[70] Watanabe K. Zr-Ni alloys as candidate getter materials for tritium processing. Fusion Eng Des 1991;18:27-32.

[71] Shi Z, Zeng M, Kang H. Property of Zr_9Ni_{11} absorption hydrogen. At Energy Sci Technol 2002;36:439-41, 57.

[72] Libowitz GG, Hayes HF, Gibb TRP. The system zirconium-nickel and hydrogen. J Phys Chem 1958;62:76-9.

[73] Issack SL, Shaaban HI, Hammad FH. Hydriding kinetics of the NiZr intermetallic compounds. In: Veziroglu TN, Taylor JB, editors. Hydrogen energy progress V, Toronto: Pergamon Press; 1984. p. 1443-53.

[74] Kabutomori T, Wakisaka Y, Tsuchiya K, Kawamura H. Improvement of hydriding properties of a Zr_1Ni_1 alloy by adding third transition metals for tritium recovery. J Nucl Mater 1998;258-263:481-7.

[75] Spriano S, Rosalbino F, Baricco M, Morra PV, Angelini E, Antonione C, et al. Surface and electrochemical characterization of Ni-Zr intermetallic compounds. Intermetallics 2000;8:299-304.

[76] Young K, Ouchi T, Fetcenko MA. Pressure-composition-temperature hysteresis in C14 Laves phase alloys: Part 3. Empirical formula. J Alloys Compd 2009;480:440-8.

[77] Allred AL. Electronegativity values from thermochemical data. J Inorg Nucl Chem 1961;17:215-21.

[78] The Japan Institute of Metals. Non-stoichiometric metal compounds. Tokyo: Maruzen; 1975

[79] de Boer FR, Boom R, Mattens WCM, Miedema AR, Niessen AK. Cohesion in metals: transition metal alloys (cohesion and structure). Amsterdam; Elsevier; 1988.

[80] Shi Z, Chumbley S, Laabs FC. Electron diffraction analysis of an AB_2-type Laves phase for hydrogen battery applications. J Alloys Compd 2000;312:41-52.

[81] Jiang W, Huang C, Huang D, Jian X, Guo J. PLS method applied to analysis of binary Laves phase structures. Acta Metall Sin 2005;41:19-22.

[82] Bsenko L. The Hf-Ni and Zr-Ni systems in the region 65-80 at.% Ni. J Less Common Met 1979;63:171-9.

[83] Joubert JM, Cerný R, Yvon K. Refinement of the crystal sturcture of zirconium nickel, Zr_8Ni_{21}. Z Kristallogr New Cryst Struct 1998;213:227-8.

[84] Kirkpatrick ME, Bailey DM, Smith JF. The structures of $NiZr_2$, NiZr and their hafnium analogs. Acta Crystallogr 1962;15:252-5.

[85] Young K, Ouchi T, Fetcenko MA, Mays W, Reichman B. Structural and electrochemical properties of $Ti_{1.5}Zr_{5.5}V_xNi_{10-x}$. Int J Hydrogen Energy 2009;34:8695-706.

[86] Kirkpatrick ME, Smith JF, Larsen WL. Structures of the intermediate phases $Ni_{10}Zr_7$ and $Ni_{10}Hf_7$. Acta Crystallogr 1962;15:894-903.

[87] Joubert JM, Cerný R, Yvon K, Latroche M, Percheron-Guégan A. Zirconium-nickel, Zr_7Ni_{10}: Space group revision for the stoichiometric phase. Acta Crystallogr Sect C Cryst Struct Commun 1997;53:1536-8.

[88] Kirkpatrick ME, Larsen WL. Phase relationships in the nickel-zirconium and nickel-hafnium alloy systems. Trans Am Soc Met 1961;54:580-90.

[89] Glimois JL, Becle C, Develey G, Moreau JM. Crystal structure of the intermetallic compound $Ni_{11}Zr_9$. J Less Common Met 1979;64:87-90.

[90] Young K, Ouchi T, Huang B, Nei J, Fetcenko MA. Studies of $Ti_{1.5}Zr_{5.5}V_{0.5}(M_xNi_{1-x})_{9.5}$ (M = Cr, Mn, Fe, Co, Cu, Al): Part 1. Structural characteristics. J Alloys Compd 2010;501:236-44.

[91] Carvalho EM, Harris IR. X-ray diffraction studies of structural changes in the system $Zr_{50}Co_{50-x}Ni_x$ ($0 \leq x \leq 50$): III. J Less Common Met 1985;106:143-52.

[92] Osumi Y, Suzuki H, Kato A, Oguro K, Kawai S, Kaneko M. Hydrogen absorption-desorption characteristics of Mm-Ni-Al-M and Mm-Ni-Mn-M alloys (Mm = misch metal). J Less Common Met 1983;89:287-92.

[93] Young K, Nei J, Huang B, Ouchi T, Fetcenko MA. Studies of $Ti_{1.5}Zr_{5.5}V_{0.5}(M_xNi_{1-x})_{9.5}$ (M = Cr, Mn, Fe, Co, Cu, Al): Part 2. Hydrogen storage and electrochemical properties. J Alloys Compd 2010;501:245-54.

[94] Ashida K, Watanabe K, Sawada E, Tada S, Ikeno S. Absorption and desorption kinetics of deuterium for ZrNi system. Research Report of the Hydrogen Isotope Research Center, Toyama University. 1993;13:63-74.

[95] Young K, Fetcenko MA, Li F, Ouchi T. Structural, thermodynamic, and electrochemical properties of $Ti_xZr_{1-x}(VNiCrMnCoAl)_2$ C14 Laves phase alloys. J Alloys Compd 2008;464:238-47.

[96] Reichman B, Venkatesan S, Fetcenko MA, Jeffries K, Stahl A, Bennett C, inventors; Energy Conversion Devices, Inc., assignee. Activated rechargeable hydrogen storage electrode and method. United States patent US 4716088. 1987 Dec 29.

[97] Backhaus-Ricoult M, Vignes JL, Lorang G, Knosp B. Microstructural characterisation of surface layers of ZrM_2 powders (Laves phases) obtained by various corrosion treatments. J Alloys Compd 1997;253-254:492-5.

[98] Yan DY, Cheng Q, Cui T. Hot alkaline treatment on hydrogen storage alloys in sealed Ni/MH batteries. J Alloys Compd 1999;293-295:809-13.

[99] Kleperis J, Wójcik G, Czerwinski A, Skowronski J, Kopczyk M, Beltowska-Brzezinska M. Electrochemical behavior of metal hydrides. J Solid State Electrochem 2001;5:229-49.

[100] Pourbaix M. Atlas of electrochemical equilibria in aqueous solution. 2nd English ed. Houston: NACE; 1974.

[101] Zaitsev A, Zaitseva N, Shakhpazov E. Thermodynamic investigation of intermediate phases for the Ni-Zr system. Dokl Phys 2001;46:784-8.

[102] Fetcenko MA, Ovshinsky SR, Chao BS, Reichman B, inventors; Ovonic Battery Company, Inc., assignee. Electrochemical hydrogen storage alloys for nickel metal hydride batteries. United States patent 5536591. 1996 Jul 16.

[103] Stucki F, Schlapbach L. Magnetic properties of $LaNi_5$, FeTi, Mg_2Ni and their hydrides. J Less Common Met 1980;74:143-51.

[104] B. Reichman, W.C. Mays, K. Young, M.A. Fetcenko, S.R. Ovshinsky, Ouchi T. Seleted battery topics. In: Cieslak WR, Abraham KM, Adams WA, Braithwaite JW, Gopikanth ML, Halpert G, et al., editors. Symposia on Aqueous Batteries; Battery Applications; Batteries for the 21st Century; Corrsionin Batteries and Fuel Cells; The Exploratory Research and Development of Batteries and Supercapacitors for Electric and Hybrid Vehicles. Boston: The Electrochemical Society, Inc.; 1998. p. 111-9.

[105] Young K, Huang B, Regmi RK, Lawes G, Liu Y. Comparisons of metallic clusters imbedded in the surface oxide of AB_2, AB_5, and A_2B_7 alloys. J Alloys Compd 2010;506:831-40.

[106] Massalski TB. Binary alloy phase diagrams. 2nd ed. Ohio: ASM International; 1990.

[107] Bsenko L. The crystal structure of Hf_8Ni_{21}. Acta Crystallogr Sect B Struct Crystallogr Cryst Chem 1978;34:3204-7.

[108] Pan H, Ma J, Wang C, Chen S, Wang X, Chen C, et al. Studies on the electrochemical properties of $MINi_{4.3-x}Co_xAl_{0.7}$ hydride alloy electrodes. J Alloys Compd 1999;293-295:648-52.

[109] Liao B, Lei YQ, Chen LX, Lu GL, Pan HG, Wang QD. A study on the structure and electrochemical properties of $La_2Mg(Ni_{0.95}M_{0.05})_9$ (M = Co, Mn, Fe, Al, Cu, Sn) hydrogen storage electrode alloys. J Alloys Compd 2004;376:186-95.

[110] Li R, Pan H, Gao M, Miao H, Lei Y. Investigation of microstructure and electrochemical properties of $Ti_{0.8}Zr_{0.2}V_{2.7}Mn_{0.5+x}Cr_{0.8}Ni_{1.5-x}$ hydrogen storage alloys. J Alloys Compd 2007;432:183-8.

[111] Liu Y, Pan H, Gao M, Miao H, Lei Y, Wang Q. Function of Al on the cycling behavior of the La-Mg-Ni-Co-type alloy electrodes. Int J Hydrogen Energy 2008;33:124-33.

[112] Miao H, Gao M, Liu Y, Zhu D, Pan H. An improvement on cycling stability of Ti-V-Fe-based hydrogen storage alloys with Co substitution for Ni. J Power Sources 2008;184:627-32.

[113] Young K, Ouchi T, Koch J, Fetcenko MA. The role of Mn in C14 Laves phase multi-component alloys for NiMH battery application. J Alloys Compd 2009;477:749-58.

[114] Young K, Ouchi T, Reichman B, Mays W, Regmi R, Lawes G, et al. Optimization of Co-content in C14 Laves phase multi-component alloys for NiMH battery application. J Alloys Compd 2010;489:202-10.

[115] Young K, Regmi R, Lawes G, Ouchi T, Reichman B, Fetcenko MA, et al. Effects of aluminum substitution in C14-rich multi-component alloys for NiMH battery application. J Alloys Compd 2010;490:282-92.

[116] Zhao Y, Gao M, Liu Y, Huang L, Pan H. The correlative effects of Al and Co on the structure and electrochemical properties of a La-Mg-Ni-based hydrogen storage electrode alloy. J Alloys Compd 2010;496:454-61.

[117] Liu Y, Cao Y, Huang L, Gao M, Pan H. Rare earth-Mg-Ni-based hydrogen storage alloys as negative electrode materials for Ni/MH batteries. J Alloys Compd 2011;509:675-86.

[118] Young K, Fetcenko MA, Ouchi T, Li F, Koch J. Effect of Sn-substitution in C14 Laves phase alloys for NiMH battery application. J Alloys Compd 2009;469:406-16.

[119] Zhu Y, Pan H, Liu Y, Li R, Jin Q, Wang Q. New type TiV-based hydrogen storage electrode alloy. Chin J of Nonferrous Met 2003;13:680-4.

[120] Powder Diffraction File database. Newtown Square: International Center for Diffraction Data; 2010.

[121] Kittle C. Introduction to solid state physics. 7th ed. New York: John Wiley & Sons; 1990.

[122] Lide DR. CRC handbook of chemistry and physics. 74th ed. Ann Arbor: CRC Press; 1994.

[123] Shaltiel D, Jacob I, Davidov D. Hydrogen absorption and desorption properties of AB_2 Laves-phase pseudobinary compounds. J Less Common Met 1977;53:117-31.

[124] Chao B, Young RC, Ovshinsky SR, Pawlik DA, Huang B, Im JS, et al. In: Doughty D, Nazar L, Arakawa M, Brack H-P, Naoi K, editors. New Materials for Batteries and Fuel Cells, Materials Research Society Symposium; 1999; San Francisco, U.S.A. Warrendale: Materials Research Society; 1999. p. 193.

[125] Amerioun S, Yokosawa T, Lidin S, Häussermann U. Phase stability in the systems $AeAl_{2-x}Mg_x$ (Ae = Ca, Sr, Ba): Electron concentration and size controlled variations on the Laves phase structural theme. Inorg Chem 2004;43:4751-60.

[126] Young K, Ouchi T, Fetcenko MA. Pressure-composition-temperature hysteresis in C14 Laves phase alloys: Part 1. Simple ternary alloys. J Alloys Compd 2009;480:428-33.

[127] Young K, Ouchi T, Mays W, Reichman B, Fetcenko MA. Pressure-composition-temperature hysteresis in C14 Laves phase alloys: Part 2. Applications in NiMH batteries. J Alloys Compd 2009;480:434-9.

[128] Schlapbach L, Zuttel A. Hydrogen-storage materials for mobile applications. Nature 2001;414:353-8.

[129] Liao B, Lei YQ, Chen LX, Lu GL, Pan HG, Wang QD. The effect of Al substitution for Ni on the structure and electrochemical properties of AB_3-type $La_2Mg(Ni_{1-x}Al_x)_9$ (x = 0-0.05) alloys. J Alloys Compd 2005;404-406:665-8.

[130] Pan H, Li R, Gao M, Liu Y, Wang Q. Effects of Cr on the structural and electrochemical properties of TiV-based two-phase hydrogen storage alloys. J Alloys Compd 2005;404-406:669-74.

[131] Pan H, Liu Y, Gao M, Lei Y, Wang Q. Electrochemical properties of the LaMgNiMnCoAl (x = 0-0.5) hydrogen storage alloy electrodes. J Electrochem Soc 2005;152:A326-32.

[132] Pan H, Li R, Gao M, Liu Y, Lei Y, Wang Q. Effects of Ni on the structural and electrochemical properties of Ti-V-based hydrogen storage alloys. Int J Hydrogen Energy 2006;31:1188-95.

ABSTRACT

MULTI-COMPONENT AB_2 METAL HYDRIDE ALLOYS FOR NICKEL METAL HYDRIDE BATTERY APPLICATIONS

by

JEAN NEI

MAY 2012

Advisors: Dr. Simon Ng and Dr. Steve Salley

Major: Chemical Engineering

Degree: Doctor of Philosophy

Compared to the mish metal-based AB_5 metal hydride (MH) alloy commonly used in Ni/MH batteries, the transition metal-based AB_2 MH alloy not only reduces the rare earth dependency, it also has higher specific energy. In order to further improve the performance of AB_2 MH alloy, it's crucial to fully understand its multi-phase nature, which includes the main C14/C15 Laves phases and the secondary non-Laves phases.

In order to optimize the gaseous phase and electrochemical advantages of both the C14 and C15 Laves phases, a study was established to identify the factors that affect the C14/C15 phase abundance. Average electron density (*e*/*a*) was proven to be an influential parameter in determining the C14/C15 phase abundance: as *e*/*a* increased, C14/C15 became less/more dominant, respectively. However, with different A-site composition, a shift in *e*/*a* was observed in the C14/C15 phase abundance vs. *e*/*a* relationship. The average chemical potential for electronic charge of A atoms (ϕ^*_A) was found to show a nearly perfect linear correlation to the C14/C15 threshold with various selections of A-site elements. The combination of *e*/*a* and ϕ^*_A

can be used to predict the C14/C15 phase abundance and assist future AB_2 MH alloy design process.

Four non-Laves phase alloys, Zr_8Ni_{21}, Zr_7Ni_{10}, Zr_9Ni_{11}, and ZrNi, commonly seen in AB_2 MH alloys were studied. Annealing treatment was adopted on each alloy to change the abundances of various phases. Annealing suppressed secondary phases except for the case of Zr_9Ni_{11}, where its secondary ZrNi phase increased. As the Zr/Ni ratio increased, the maximum gaseous phase hydrogen storage capacity increased but maximized at Zr : Ni = 9 : 11. Comparing the properties before and after annealing, it was clear that the natures of constituent phases influenced the gaseous phase storage. The highest full discharge capacity was obtained at Zr : Ni = 7 : 10, which is a compromise between the hydrogen desorption rate and the theoretical maximum gaseous phase hydrogen storage. As the Zr/Ni ratio increased, the amount of metallic Ni in the surface oxide decreased, therefore the high-rate dischargeability decreased. Among all alloys, the unannealed Zr_7Ni_{10} demonstrated the best gaseous phase hydrogen storage and electrochemical capacities, and the unannealed Zr_8Ni_{21} showed excellent HRD and activation.

Zr_8Ni_{21} alloy was then chosen based on its promising performance to be further modified for the purpose of developing alternative MH alloys for Ni/MH batteries. $Zr_8Ni_{19}X_2$ alloys (X = Ni, Mg, Al, Sc, V, Mn, Co, Sn, La, and Hf) were prepared and studied. The effect of annealing on these alloys was also investigated. Only the main phase of the annealed Sn-substitution remained Zr_8Ni_{21}-structured while those of other substitutions turned into Zr_7Ni_{10} or Zr_2Ni_7. Annealing generally suppressed secondary phases except for the case of $Zr_8Ni_{19}Sn_2$, where the major phase transformed from Zr_2Ni_7 to Zr_8Ni_{21}. Both the maximum gaseous phase hydrogen storage and electrochemical full discharge capacities followed the increasing order of B/A ratio of the main phase. After annealing, all alloys except for the Sn-substitution showed degradation

in full discharge capacity due to the reduction in number and abundance of the catalytic secondary phases. Among all alloys, the as-cast Hf-substituted Zr_8Ni_{21} alloy demonstrated the best overall gaseous phase hydrogen storage and electrochemical properties.

AUTOBIOGRAPHICAL STATEMENT

EDUCATION

B.S., Chemical Engineering, Wayne State University, May 2004

PUBLICATIONS

1. **Nei J**, Young K, Salley SO, Ng KYS. Effects of annealing on $Zr_8Ni_{19}X_2$ (X = Ni, Mg, Al, Sc, V, Mn, Co, Sn, La, and Hf): Hydrogen storage and electrochemical properties. International Journal of Hydrogen Energy. 2012. doi: 10.1016/j.ijhydene.2012.02.066.

2. **Nei J**, Young K, Salley SO, Ng KYS. Effects of annealing on $Zr_8Ni_{19}X_2$ (X = Ni, Mg, Al, Sc, V, Mn, Co, Sn, La, and Hf): Structural characteristics. Journal of Alloys and Compounds. 2012;516:144-52.

3. **Nei J**, Young K, Salley SO, Ng KYS. Determination of C14/C15 phase abundance in Laves phase alloys. Submitted to Materials Chemistry and Physics, 2012

4. **Nei J**, Young K, Lawes G, Salley SO, Ng KYS. Gaseous phase hydrogen storage and electrochemical properties of Zr_8Ni_{21}, Zr_7Ni_{10}, Zr_9Ni_{11}, and ZrNi metal hydride alloys. In preparation, to be submitted to International Journal of Hydrogen Energy, 2012.

5. Young K, **Nei J**, Huang B, Fetcenko MA. Studies of off-stoichiometric AB_2 metal hydride alloy: Part 2. Hydrogen storage and electrochemical properties. International Journal of Hydrogen Energy. 2011;36:11146-54.

6. Young K, **Nei J**, Ouchi T, Fetcenko MA. Phase abundances in AB_2 metal hydride alloys and their correlations to various properties. Journal of Alloys and Compounds. 2011;509:2277-84.

7. Young K, Ouchi T, Huang B, **Nei J**, Fetcenko MA. Studies of $Ti_{1.5}Zr_{5.5}V_{0.5}(M_xNi_{1-x})_{9.5}$ (M = Cr, Mn, Fe, Co, Cu, Al): Part 1. Structural characteristics. Journal of Alloys and Compounds. 2010;501:236-44.

8. Young K, **Nei J**, Huang B, Ouchi T, Fetcenko MA. Studies of $Ti_{1.5}Zr_{5.5}V_{0.5}(M_xNi_{1-x})_{9.5}$ (M = Cr, Mn, Fe, Co, Cu, Al): Part 2. Hydrogen storage and electrochemical properties. Journal of Alloys and Compounds. 2010;501:245-54.